Mechanical response of ssDNA filaments and ss/dsDNA patches: experiments and simulations

Candidate: Alessandro Bosco

Supervisors: Prof. Cristian Micheletti and Prof. Antonio DeSimone

Sector of Statistical and Biological Physics, SISSA

A thesis submitted for the degree of

PhD in Physics and Chemistry of Biological Systems

Academic year 2010/2011

To my extended family...

Contents

ABBREVIATIONS

List of Abbreviations

AD	Antidigoxigenin
AFM	Atomic Force Microscope
DNA	Deoxyribonucleic Acid
dsDNA	double-stranded DNA
EDTA	Ethylenediaminetetraacetic acid
FJC	Freely Jointed Chain
MUF	Mean Unzipping Force
OT	Optical Tweezers
SA	Streptavidin
ssDNA	single-stranded DNA
TC	Thick Chain
TOEG3	Top Oligo Ethylene-Glycol (3) alkylthiol
WLC	Worm Like Chain

0

Introduction

In this thesis we shall present experimental and computational results about the mechanical properties of DNA systems.

DNA is one of the main subject of biophysical studies. This biomolecule is the prototypical example of how the function and the structure of a biological molecule can be tightly interconnected. The discovery of the structure of DNA [1, 2], which clarified the molecular basis of storage of genetic information, has become a landmark in twentieth century biology. The pairing mechanism between the complementary bases discovered by Watson and Crick is in fact the key feature for storing and replicating the hereditary information [3, 4].

Aside from its fundamental biological role, DNA has been also fruitfully exploited as a material for self assembly for nano-bio-sensing. The strong technological push towards miniaturization opened the way to the use of these molecules as building blocks for different application. This bottom-up approach allowed for the production of devices with dimensions on the nanoscale but a direct control on the position of the molecules has been possible thanks to the development in the last decades of new instruments and techniques for the manipulation of single or few molecules [5]. With techniques such as atomic force microscope (AFM) and optical tweezers (OT) it is possible to apply forces to single molecules and to control their position at the nanoscale.

Besides, with these techniques, it is possible to study at the level of individual molecule the physical and structural properties of biomolecules in a wide variety of conditions. These experiments allows for singling out the behavior of individual molecules instead of considering the average ensemble one standard bulk experiments

[6]. Such measurements can be used to study the elastic properties of different individual biomolecules (DNA, proteins and polysaccharides [7]) giving an insight on the interactions that stabilize their biomolecular structure. Moreover these techniques can be effectively used to explore the interactions of DNA with a different variety of molecules such as small ligands or complex proteins [8].

In this thesis, we address two problems where the elastic properties of DNA molecules play an important role in defining the behavior of the system subject to an applied force: the stretching of single stranded DNA and the compression of DNA patches.

Before we get into the heart of these two arguments, several framework topics are introduced in the Chapter 1: the structural and chemical basis of DNA, the instruments for single molecule manipulation (in particular the AFM and the OT), some basics of polymer physics and biosensors.

The first argument of this thesis, the study of the mechanical response of the single stranded DNA (ssDNA) is described in Chapter 2. Despite the huge amount of papers produced on elastic properties of nucleic acids, the literature on ssDNA is less wider than the one focused on dsDNA. ssDNA is a molecule of great biological relevance but the experimental study of this molecule is quite challenging because of the interplay of electrostatic interaction, stacking and basepairing interaction. All these properties play a role in the elastic response of ssDNA and in the formation of secondary structures.

In the thesis, we report about the use of a very promising technique to obtain force extension curves of long molecules of ssDNA with an OT set up in order to produce a systematic study of the elastic properties and the formation of secondary structure at different salt conditions. The experiments are carried out both in monovalent and in divalent salt condition and the force extension curves have been compared with the data reported in literature.

Theoretical models are used to characterize the force extension curves obtained by the experiment. Moreover by the analysis with these models the fraction of paired bases and hence the formation of secondary structure has been pointed out.

The other topic discussed in the second part of the thesis is the compression of DNA patches. These patches consist of DNA oligonuclotides grafted on a surface in a confined manner and are produced using nanografting, an innovative technique for the AFM tip-aided deposition of DNA on surface.

From the technological point of view DNA patches are very promising nanostructure for biological applications. In particular, it is possible to use them in sensors for detecting biochemical reactions. Patches of ssDNA, are in fact used as mechanical transducers of the hybridization with complementary sequences: the occurred hybridization can be in fact sensed by AFM topographic image at different applied load [9]. However in such systems, the surface density and the hybridization efficiency are a piece of information difficult to achieve but fundamental from the perspective of the production and characterization of this kind of nanodevice.

In this thesis we introduce and discuss a coarse grained computational approach that can be used for the quantitative description/prediction of DNA patch sensed and compressed by an AFM tip. Specifically the main purpose of our model is to obtain computationally the height of the DNA patch of both ssDNA and dsDNA at a given surface density and applied force. Once this relation is known, it can be fruitfully exploited in reverse on a real system for the estimation of the surface density starting from AFM topographic images of DNA patches at different applied load.

Chapter 3 introduces the basic elements of the model and the parametrization chosen. In particular here we discuss the DNA model that contains the excluded volume effect and the bending rigidity, the modelization of the surface and the kind of simulations chosen . Furthermore, the computational results are examined and incorporated in a model for the description of the compression of the patch with an AFM tip.

Our model is successively, first validated and than used on height *vs* applied load measurements obtained form experimental data. Chapter 4 is focused on the experimental part and the relative comparison with the model. The fabrication technique used for DNA patches and the experiments of compression are described here. In this chapter we present also the major outcomes obtained from the comparison with the model. Adding to that, by using simple considerations it will be possible to give an estimation of the efficiency of hybridization in ssDNA patches.

The major part of the work presented in this thesis has been carried out at SISSA. The experiment of stretching of ssDNA have been carried out at the Small Biosystem Laboratory in Barcelona within the collaboration of the group of Prof Felix Ritort of the University of Barcelona.

For what concerns the work on DNA patches, the experiments used for the validation and comparison with the model have been produced by the Senil Nano-Innovation Laboratories headed by Dr. Loredana Casalis.

These findings have been object of two publications:

- A. Bosco, F. Bano, P. Parisse, L. Casalis, A. DeSimone and C. Micheletti, "*Hybridization in Nanostructured DNA Monolayers probed by AFM: Theory Versus Experiment*", submitted for publication

- A. Bosco, J. Camuñas and F. Ritort, "*Stretching ssDNA*", in preparation

on which the material presented in this thesis is based.

1

Background Material

1.1 Introduction

DNA plays a prominent role in all living organism [10]. Since the discovery that the genetic information is coded in DNA [1, 2], this molecule and, more in general, nucleic acids, have attracted the interest of a numerous community of scientists across chemistry, physics and biology. DNA in fact is the classical example of how biological function follows from biomolecular structure [3]. According to Victor McElheny, the breakthrough of James D. Watson and Francis Crick (supported by the discoveries of Rosalind Franklin [11, 12] and Maurice Wilkins [13]) can be put it in the same class of Newton's law of motion. In fact, this discovery prepared the bases of the major advancements in biology in this century, such as biochemistry of DNA replication, the understanding of genetic code, genetic engineering, and the sequencing of the human genome [14].

1.2 DNA structure

DNA is a linear polymer whose monomeric units are nucleotides. A nucleotide consists of a nitrogenous base (or nucleobase), a five-carbon sugar and one phosphate group (See the top left of Figure 1.1). A DNA strand consists of a backbone of alternating phosphate and sugar residues to which the nitrogenous bases are attached.

The sugars are D-2-deoxyribose arranged in a ring structure and are joined together by the phosphates through phosphodiester bonds between the carbon atoms in the third and the fifth position. This asymmetric linkage of the sugars gives a directionality to

the strand that has two different ends. The one called 5' that has a phosphate group and the other called 3' bearing a hydroxyl functionality. In dsDNA the two strands run in opposite direction.

At the carbon in position two is attached the nitrogenous base that can be a purine or a pyrimidine. In DNA this can be an Adenine, a Guanine, a Cytosine or a Thymine (top right of Figure 1.1). Each base is essentially planar and its conformations are limited. Typically, the base lies perpendicular to the direction of the backbone.

The molecular structure of nucleobases gives the possibility to form hydrogen bonds with each other, forming base-pairs. Base-pairing is possible between a purine and a pyrimidine, in particular, Adenine can pair via hydrogen bonding with Thymine and Guanine with Cytosine [15]. The possibility of base pairing allows DNA to be found as a single stranded (ssDNA) or as a double stranded molecule (dsDNA).

In the '50, Chargaff gave the chemical evidence of this pairing but only with the work of Watson and Crick its structural role and the biological function became clear. There are alternative pattern of hydrogen bond with which bases can pair [3] but Watson-Crick basepairing, shown in top right of Figure 1.1 is the most frequent.

Nitrogenous bases are formed by planar rings that can interact with adjacent bases through aromatic interaction [4] and can arrange parallel to each other. This non covalent interaction is called *stacking* and can add stability of the molecular structure. The general three-dimensional form of local segments of DNA strands depends on base pairing and hence stacking.

For a generic molecule of DNA, the sequence of nucleotides is called in the literature primary structure, while the spatial organization of the nucleotides is referred to as secondary structure. dsDNA assumes the widely known double helix form that is held together tightly by means of the hydrogen bonding of the nitrogenous bases. In nature there are at least 3 DNA conformations: A-DNA, B-DNA, and Z-DNA. In cells, the B form is believed to be the predominant one [3] and the double helix contains about 10.5 base pairs per turn in solution and corresponds to a rise between adjacent bases of 0.34 nm.

ssDNA is generally less structured, however it can form stem-loop structure (or commonly known as hairpin) or pseudoknots (see Figure 1.1)

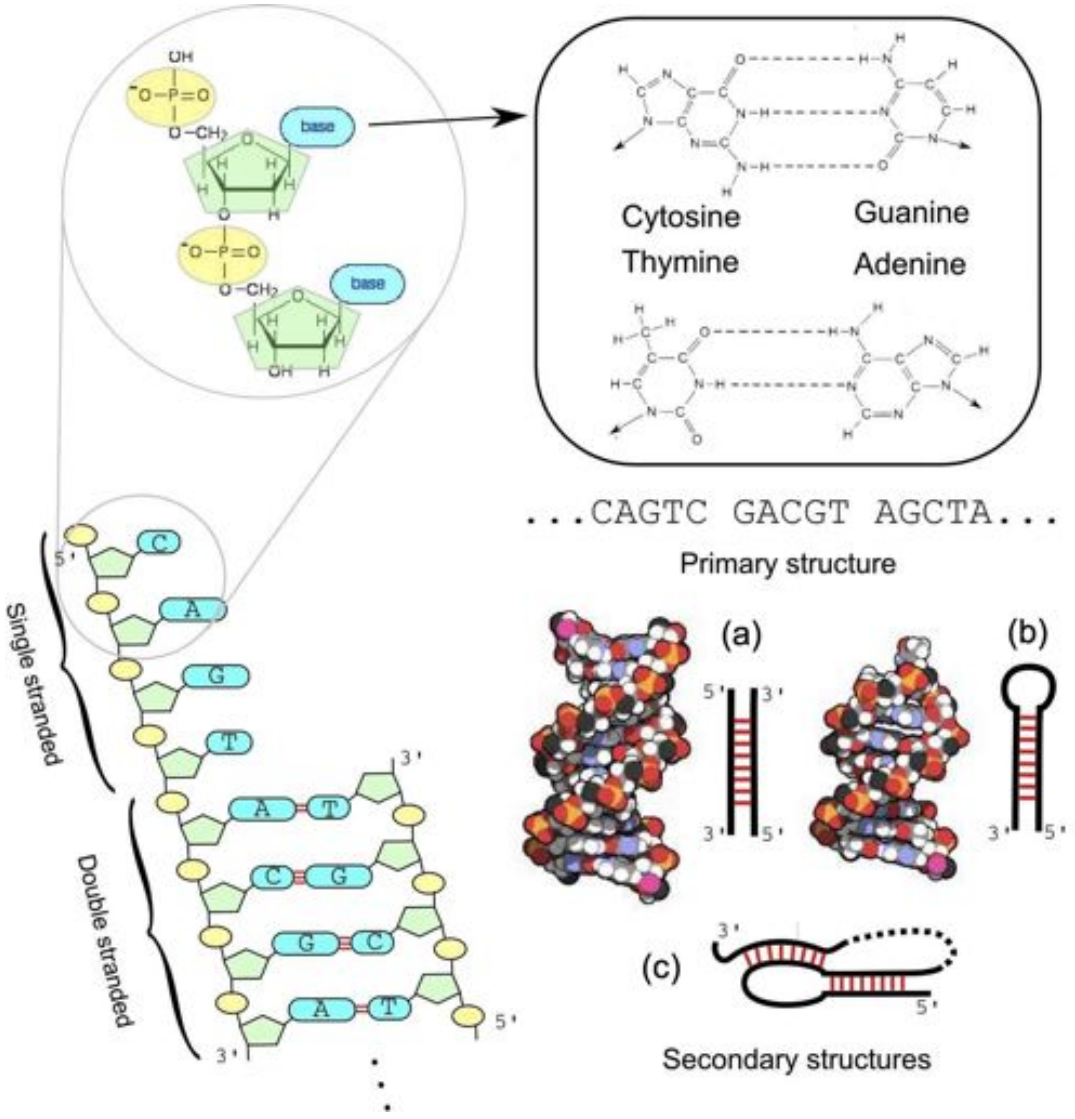

Figure 1.1: Chemical structures and organization of DNA. Top Left: two nucleotides showing the structural formula Top Right: Structural formula of the nucleobases and the Watson-Crick pairing. Bottom Left: Schematic organization of a DNA molecule (single and double stranded) Bottom Right: Primary and Secondary Structures for DNA: (a) dsDNA, (b) an hairpin (scheme and structure with atomic detail) and (c) a pseudoknot (scheme only).

1.3 Single molecule experiments

In modern biophysics, the study of single molecules has become a major field of research. This has been supported by the development in the last decades of instruments capable

to manipulate one or few molecules [5].

In the last decades, the study of the DNA by means of single molecule experiments has been profitably exploited for understanding the mechanical behavior of DNA and the interactions between DNA and proteins [8]. These investigations have laid the groundwork for real-time, single-molecule assays of enzyme mechanism [16]

The most commonly used instruments that have been developed are Atomic Force Microscope (AFM) and Optical Tweezers (OT). We will focus on these two instruments also because they have been used for the experiments described in the following of the thesis.

With AFM it is possible to take images of molecules adsorbed on surfaces and to produce nano dimensional objects by moving molecules one at the time. With OT one can move microscopic objects and apply mechanical forces in the picoNewton range.

1.4 The Atomic Force Microscope

The atomic force microscope is part of the family of scanning probe microscopes in which a physical probe is moved in proximity of surface of the specimen obtaining an image of the sample. An AFM consist in a soft cantilever with a tip that is moved near the surface sensing the topographic profile of the sample [17]. Figure 1.2 shows a schematic representation of the set up.

In a generic AFM setup the tip is brought near the surface and the cantilever bends (according Hooke's law) by an amount which is proportional to the proximity of the tip to surface. The deflection is caused by the interactions of the tip with the surface (Van der Waals forces, electrostatic forces, etc.).

The bending of the cantilever can be detected in several ways, and the most common setup uses a laser. The laser beam is focused on the cantilever that reflects the light to a detector (an array of photodiodes). When the cantilever bends, the position of the laser focus moves on the detector and the signal of the photodiodes changes. Typically the cantilever is moved in the direction perpendicular to the sample plane by a piezoelectric actuator and a feedback mechanism allows for keeping the force between the tip and the surface constant. A piezoelectric stage controls the sample position.

AFM can work in several modes: *contact mode*, *non-contact mode* and *tapping mode*. In *contact mode*, the AFM tip touches directly the sample so the overall forces

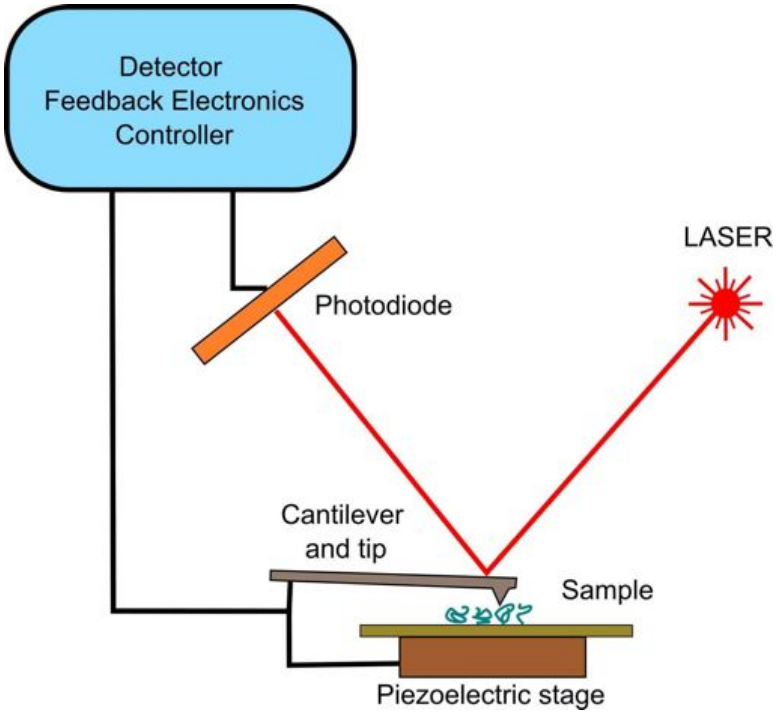

Figure 1.2: Scheme of an Atomic Force Microscope

that bend the cantilever are repulsive: the deflection is due to mechanical contact forces.

In non *contact mode*, the tip is put in proximity of the surface in a region where it feels the attractive interaction with the surface. The resulting force sensed by the tip is kept constant during the measurement.

In *tapping mode*, the cantilever oscillates at a constant amplitude over the sample. When the tip encounters a bump on the surface, the amplitude is damped and a feedback system increases the distance of the cantilever in order to keep the oscillation amplitude constant.

The AFM can be used to manipulate and exert mechanical forces on individual biomolecules [18]. It is possible to apply forces to molecules both in compression and in pulling mode. In order to pull molecules there is the need to chemically or physically attach the molecules to the tip or to the surface. It is also possible to work in a liquid environment by immersing the sample and the cantilever in a solution. The AFM can exert forces in the range between 20 pN to 10 nN, depending on the elastic properties of the cantilever. The typical stiffness of the cantilever goes between 10 to 1000 pN

nm^{-1}. The resolution of an AFM depends on thermal fluctuation of the cantilever. At room temperature, one typically sees force fluctuation of the order of 20 pN and spatial fluctuation of about 0.2 nm, if the cantilever stiffness is 100 pN nm^{-1}, a typical value.

1.5 The Optical Tweezers

The basic principle of optical tweezers is the trapping of particles caused by gradient forces generated by a laser beam [5, 19, 20]. When a beam of light is focused on a microscopic object with an index of refraction higher than the surrounding medium (e.g. a bead of polymeric material immersed in water), it creates a trapping potential in the region of maximum light intensity. Once the object is trapped, it is possible to manipulate molecules by chemically attaching them on the bead.

In the basic set up, optical tweezers consist of a near-infrared laser collimated by a high numerical aperture lens immersed in water. The trapped object is a micrometer sized polystyrene or silica bead that is trapped in the focus of the lens where the forces exerted on the micro sphere are in the range of 0.1 to 100 pN .

The trapping potential is well approximated by a harmonic potential and hence the force acting on the bead depends linearly on the distance. The coefficient of proportionality is called stiffness of the trap and it depends on the size of the bead and the power of the laser. Typical values are three orders of magnitude smaller than the stiffness of an AFM cantilever so that the fluctuation of the force (and therefore the resolution of OT) is in the order of 0.1 pN.

In the last decades, the technique has been improved by the development of optical tweezers with two counter propagating laser beams that pass through identical objectives facing one another [21, 22]. This setup increases the stiffness of the optical trap and allows for the direct measurement of the force from the total amount of light deflected by the bead which is collected by a position sensitive detector. Figure 1.3 (top) shows a schematic representation of the setup.

The manipulation of micro particles, and hence of the attached molecules, is carried out in a microfluidic chamber (see the bottom left of Figure 1.3) where the fluids (water or chemicals) can be easily replaced. Two micrometer sized glass tubes connect two lateral chambers to the main one in order to selectively flow the particles in the main chamber. A micropipette is positioned at the center of the main chamber and it can be

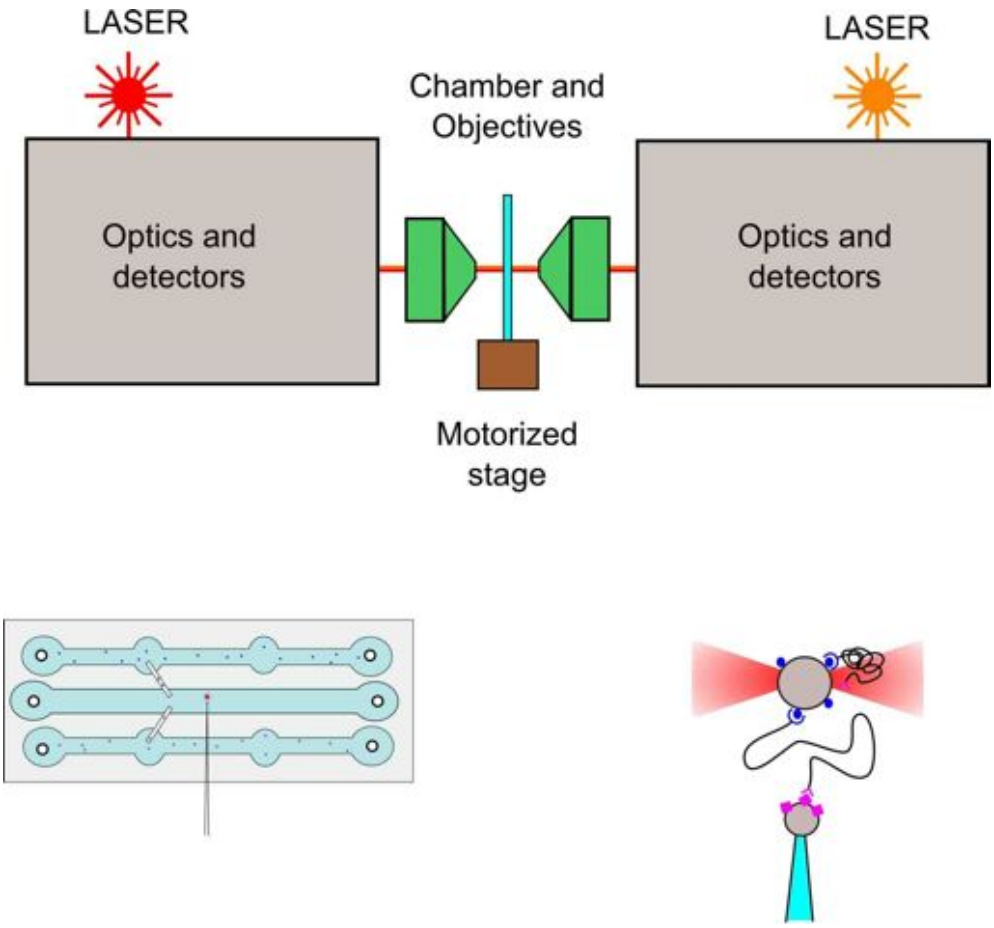

Figure 1.3: Top: Scheme of Optical Tweezers. Bottom-left: Schematic representation of the chamber. Blue and magenta dots represent the functionalized polystyrene beads flowing in the channels. Bottom-right: Representation of the connections between the bead in the optical trap (top), the molecule of interest (black line) and the bead in the micropipette (bottom). Blue circles and magenta squares represent the the protein for the specific binding on the beads.

used to block a bead by suction. The molecules and the beads are functionalized with chemical substances that can selectively bind. This "lock and key" selective interaction attaches the molecule to the beads and gives the possibility to nano-manipulate the molecules moving the beads. For example in a pulling experiment, the molecules are labeled at the ends with two different proteins or molecules (see the bottom right of Figure 1.3). These molecules have the possibility to specifically bind other proteins, in a lock-key fashion, forming a stable complex. Such complexes can be biotin/streptavidin

or antigen/antibody such as digoxigenin/antidigoxigenin.

The functionalized molecules are dissolved in a solution with microscopic beads coated with proteins selective for one label. In this way, the attachment of one end to the beads is achieved. The other bead, selective to the other end of the molecule, is fixed to the micropipette. The bead with the molecules are put in the chamber and one is picked by the optical tweezer. By putting the two beads in contact it is possible to attach the other end to the bead in the micropipette

Once the molecule is connected to both beads, it is possible to study the elastic response, by slowly moving away the bead in the optical trap and than recording the position and the force exerted on the trap by the pulling.

1.6 Models of biopolymer

In order to describe the elastic properties of DNA in single molecule experiments, a coarse grained description of this biopolymer is used. Theoretical concepts and methods borrowed from polymer physics are frequently used in biophysics to characterize DNA and biopolymers.

Ideal chains are a common starting point for describing the macroscopic behavior of biomolecules. In such systems the chain monomers do not interact with each other. In this way the complex behavior of a "real" polymer can be approximated by a model with few parameters [23].

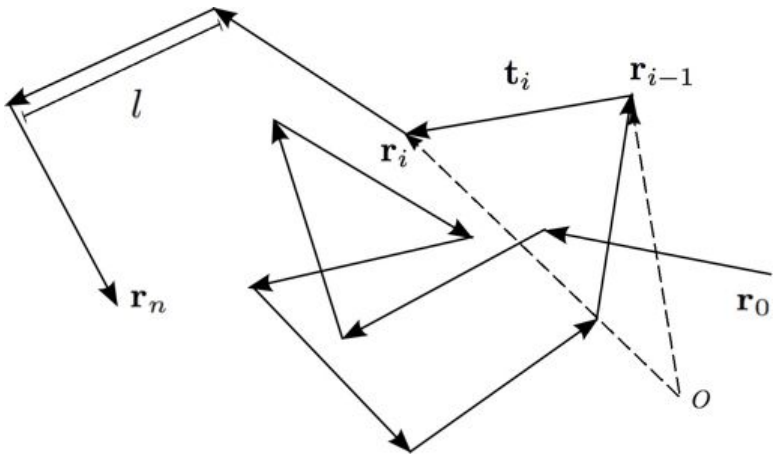

Figure 1.4: A representation of a polymer conformation

In following we will describe some simple models. A polymer conformation (see figure 1.4) is described by the positions of the $n+1$ monomers, denoted as $\{\mathbf{r}_i\}$ where i goes between 0 and n. The "bond vectors" $\mathbf{t}_i$ can be defined as

$$\mathbf{t}_i = \mathbf{r}_i - \mathbf{r}_{i-1} \quad i = 1, 2, ..., n. \tag{1.1}$$

The *contour length* L_c is the sum of all lengths of all bond vectors, that is

$$L_c = \sum_{i=1}^{n} \|\mathbf{t}_i\| \tag{1.2}$$

The simplest polymer model is the Freely Jointed Chain (FJC). In this model, the bond vector length is constant and there is no interaction between the monomer, that means that the direction of every bond vector is independent from all the other bond vectors. This also implies that the energy of the polymer does not depend on its conformation, so at the thermodynamic equilibrium the configurations are equally likely to occur.

A useful measure of the "size" of the polymer in equilibrium is the *mean-square end-to-end distance*, defined as

$$< R^2 >=< \sum_{i=1}^{n} \sum_{j=1}^{n} < \mathbf{t}_i \cdot \mathbf{t}_j > \tag{1.3}$$

where $< ... >$ is the average over all allowed conformation of the chain.

If all the bonds have the same length, so $\|\mathbf{t}_i\| = l$ for any i, Eq 1.3 can be written in terms of the angle θ_{ij} between the vectors $\mathbf{t}_i$ and $\mathbf{t}_j$, so that

$$< R^2 >= l^2 \sum_{i=1}^{n} \sum_{j=1}^{n} < \cos\theta_{ij} > \tag{1.4}$$

In the case of FJC $< \cos\theta_{ij} >= 0$ for $i \neq j$ and the mean-square end to end distance becomes $< R^2 >= nl^2$.

Another useful model is the Kratky-Porod Chain, that can be viewed as a FJC to which bending rigidity is added. The Hamiltonian of the system can be written as

$$H^{KPC} = -\varepsilon \sum_{i=1}^{n-1} \left(1 - \frac{\mathbf{t}_i \cdot \mathbf{t}_{i+1}}{l^2}\right) \tag{1.5}$$

where ε is the bending rigidity coefficient. The tangent-tangent correlation function has the following form

$$< \cos\theta_{ij} >= \exp\left(-\frac{|j-i|}{l_p}l\right) \tag{1.6}$$

where l_p is the persistence length and is related to ε by $\varepsilon = k_B T \frac{l_p}{l}$, where k_B is the Boltzmann constant.

In the continuum limit, this model is commonly known as Worm Like Chain (WLC). WLC describes a chain with continuous curvature. The polymer can be described as a path in the three-dimensional space $\mathbf{r}(s)$ with s the distance from one end (arc length). The position of the other end will be $\mathbf{r}(Lc)$. The bending energy can be written as

$$H^{WLC} = \frac{k_B T l_p}{2}\int_0^{L_c}\left(\frac{\partial^2 \mathbf{r}(s)}{\partial s^2}\right)^2 ds \tag{1.7}$$

so the more the chain is bent, the higher its energy.

As described in previous sections, with single molecule experiments it is possible to apply a force to macromolecules. With the models of FJC and WLC one can describe the stretching response of polymer-like molecules, such as DNA and proteins.

Consider a FJC that is anchored at one end to a fixed point (the origin of the Cartesian coordinate system) and that is pulled at the other end by a force f directed along the z axis. The energy of the chain will be proportional to the projection of the end-to-end vector on the direction of the applied force, so that

$$U^{FJC} = -fR_z \tag{1.8}$$

where R_z is the length of the vector projected along the z axis. From Eq. 1.9 it is possible to evaluate the partition function Z as:

$$Z = \sum_{states}\exp\left(\frac{-fR_z}{k_B T}\right). \tag{1.9}$$

The force dependence of the mean end-to-end distance (commonly referred to as the elongation or extension of the polymer) is computed as:

$$< R >= -\frac{\partial\left(-k_B T \ln\left(Z\right)\right)}{\partial f} = L_c\left[\left(\frac{fl}{k_B T}\right) - \frac{k_B T}{fl}\right]. \tag{1.10}$$

For the case of a WLC, an analytical exact solution for the $< R > vs\ f$ relationship is not presently available but several approximate forms have been proposed. The one that is most commonly used is [24] :

$$f = \frac{k_B T}{l_p} \left[\frac{1}{4} \left(1 - \frac{< R >}{L_c} \right)^{-2} + \frac{< R >}{L_c} - \frac{1}{4} \right]. \tag{1.11}$$

Such models have been primarily used to describe the force extension curves of different biopolymers, such as protein, polysaccharides and nucleic acids [7]. In addition, these models have been also proficiently used to extract informations about the interaction of the biopolymer with itself or with other molecules [5, 8, 18].

In the following chapter of this thesis, these models are used in two ways: for describing the force extension curve of ssDNA and for studying the formation of secondary structures.

1.7 Biosensors

Life is based on biorecognition events. From bacteria to humankind, the interactions between biological molecules generate stimuli that can lead to an effective response of the cell or of the organism. Understanding these processes from the level of the structural information to the biochemical activity gave the possibility to build biosensors. A biosensor is a device that contains a bioreceptor, i.e. a system capable to recognize a molecule of biological relevance (the analyte), and a transducer or detector element which converts the information into a detectable signal [25, 26].

Biosensors can be classified by either their bioreceptor or by their transducer. In this thesis we focus on biosensors whose bioreceptor is based on DNA. The transducer can be classified by the signal produced from the recognition event which can be optical, electrochemical or mechanical.

The development of miniaturization technology and nanomanipulation instruments coupled with a more detailed knowledge of biology at molecular level offered the possibility to build smaller and smaller biosensors. In particular, with these instruments, the detection can be carried out directly by sensing the change in conformation or the variation of the properties at the molecular level caused by the biorecognition event.

Bottom up technology is currently being exploited for the assembly of functional devices using programmed molecular building blocks [27]. By chemical (or biochemical)

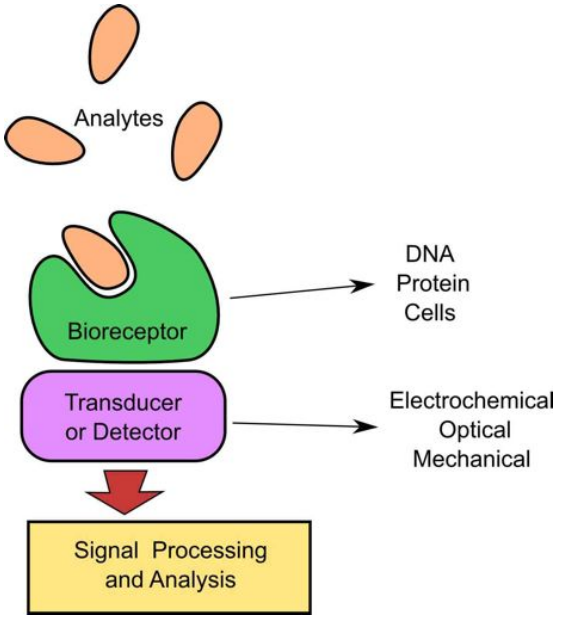

Figure 1.5: Scheme of a biosensor

synthesis it is possible to combine and to form construct that can be assembled in a spatially organized nanostructure. In fact, DNA is a particularly promising candidate to serve as a construction material in nanoscience [28, 29, 30]. DNA can be either the active site of the biorecognition event or it can be exploited as a building block of a nanostructured system. Therefore the highly specific formation of Watson-Crick basepairs can be exploited in these two ways.

1.7.1 DNA-based Biosensors

Biosensors for DNA sequence detection are part of this first class. In these system, the biorecognition event is the hybridization of ssDNA molecules with the complementary sequences, so in this case DNA acts as active site. Among these there are microarrays [31] in which the molecular recognition events are transduced and amplified into a detectable signal. A microarray consists of ssDNA molecules, from 10 up to 5000 nucleotide long, attached to a support surface.

The hybridization is detected by means of a fluorescence signal. The DNA sequences that must be detected are labeled with a fluorophore in order to detect hybridization. Figure 1.6 shows a schematic representation of the hybridization event in a microarray.

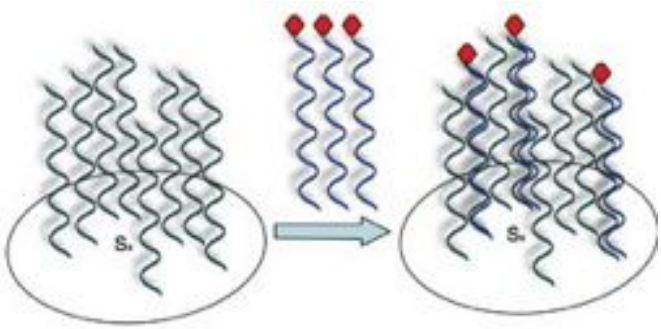

Figure 1.6: Pictorial representation of the working principle of a microarray. Reproduced from [32]

More sophisticated detection techniques give the possibility to avoid the labeling of the complementary sequences and the direct recognition of the hybridization. These devices are based on the measuring of the change in physical properties that occurs at the sample-detector surface interface [33, 34, 35]. One very promising technique is the direct detection of the hybridization by means of AFM mechanical sensing of a DNA patch attached to a surface [9]. These systems are described with full detail in the second part of the thesis. Moreover AFM based direct detection of biomolecular events has been exploited in the study of DNA-enzyme interaction [36].

Additionally, DNA can be used as a building block of bioanalytical devices. The development of DNA-protein conjugates has contributed to the development of surface devices for biorecognition. DNA can be exploited as a spacer between the protein and the surface. DNA direct immobilization provides a chemically mild process for the highly parallel binding of multiple delicate protein to a solid support by using DNA patches as immobilization matrices [37]. In this way the protein retain the biological activity thanks to the DNA spacer that avoids the direct attachment of the protein to the surface that could limit the conformational freedom of the protein and could lead to denaturation of the tertiary structure. An example of this kind of device has been developed and built by Bano and coworkers [38].

However in all these DNA-based devices, it is crucial to control the probe density in order to achieve the highest reproducibility and to optimize the sensitivity of the device. In fact, a low DNA density (corresponding to few hundreds of molecules per 0.1 micron square) may not be detectable while a too high density can sterically hinder the

complementary strand or the DNA-protein conjugates from entering the nano-structure and hybridize with the complementary probes. Moreover for nanoscaled biosensors, the control of the surface density and the hybridization efficiency of the grafted DNA can not be achieved with well-established techniques, such as surface-plasmon resonance or electrochemical techniques [39, 40] because these are best suited for DNA samples of much larger size.

The need of a new strategy to control the surface density and the hybridization efficiency motivated the work presented in the second part of the thesis.

2

Stretching ssDNA

2.1 Introduction

In the last decades the interest in single stranded DNA (ssDNA) has gained great relevance because of its major role in many biological processes, such as replication, recombination, repair, transcription and transposition of DNA [41]. Chemical and physical characterization of ssDNA is fundamental for understanding its structure and then inferring its function. As discussed in chapter one, with single molecules experiments [5] it is possible to collect force extension curves of different biomolecules (protein, sugars and nucleic acids) that can be used to characterize and obtain structural information on these systems.

Literature on ssDNA is less wide then the one focused on double stranded DNA (dsDNA) [42]. ssDNA is a biological molecule difficult to study because of the interplay between several intrinsic properties [43] such as the electrostatic interaction and base paring interaction.

As dsDNA and all nucleic acids, ssDNA has a high linear density of electrostatic charge. In fact, the backbone of nucleic acids is highly charged (it bears one negative charge per nucleotide) due to the presence of phosphate groups. Moreover ssDNA, can interact with itself forming secondary structure by Watson-Crick hydrogen bonding and a-specific hydrogen bonding [15]. Also base stacking between the bases plays a role in the formations of secondary structures [3].

Added to these intrinsic difficulties, ssDNA also shows interactions with a variety of substrates [44, 45, 46, 47]. Due to this fact, the realization of single molecule experiment

using ssDNA is very difficult.

Characterizing the formation of secondary structure is an important task in understanding the behavior of ssDNA. The interplay between base-pairing, stacking and electrostatics, define the behavior of ssDNA in the formation of secondary structure.

Most experimental methods for secondary structure analysis rely on the differential reactivity of single and double stranded regions of nucleic acids with chemical and enzymatic agents [48, 49]. However deducing structural information form these data is complicated by the fact that such reactivity is usually sequence dependent and is averaged over an ensemble of possible structures adopted by the molecule. Using single molecule experiment to study secondary structure formation, can overcome this problem.

In this chapter, we present a very promising technique that allows to study the force extension curves of ssDNA. This technique has been devised by Prof Felix Ritort and coworkers and has been further developed within the framework of a collaboration with his group in Barcelona. All the experiments reported in this chapter have been developed and carried out at the Small Biosystems Lab of the Department of Fundamental Physics in Barcelona.

The idea is to start from a long hairpin (6.8 kbp), that is mechanically unzipped by means of an optical tweezer set-up. Once ssDNA has been obtained by unzipping, a solution that contains a small concentration of an 30 bases oligonucleotide designed to adhere to the loop region, is flushed into the chamber. When an oligonucleotide is bound to the hairpin, it prevents the re-zipping because the loop region cannot bend back on itself and the reformation of the hairpin is inhibited. In this way, by approaching the two beads it is possible to collect the force extension curve of the ssDNA with the optical tweezers .

Primarily in order to check the reproducibility, force extension curves at seven different monovalent salt conditions have been carried out. Moreover we performed experiments at different divalent salt conditions. At present there are only few papers in which the properties of ssDNA in presence of divalent ions have been studied [50, 51, 52]. To our knowledge, this is the first work in which a systematic study of force extension curves has been presented for ssDNA at different divalent salt concentration.

Here, after a brief review of the literature, the technique and the experiments are presented. Then the compatibility with results reported in literature has been checked.

We report here also the analysis with theoretical models for the description of force extension curves in order to describe the elastic response and to point out the formation of secondary structure.

2.2 Literature background

A general review on the experiments that have been carried out on DNA has been published recently [42]. Here we report the main contributions to the field in order to make a survey of the analogous techniques to obtain ssDNA and some models useful for describing the force extension curves that have been used for the description of single stranded nucleic acids.

In order to obtain ssDNA the simplest strategy is to unbind the two strands of a dsDNA. Different methods have been used but mostly thermal [53] or chemical denaturation[50, 52].

Chemical treatment of the ssDNA has been also used in order to screen baseparining interactions in order to study the electrostatics of ssDNA [52, 54, 55, 56]. In this kind of experiments, it is used glyoxal, a chemical compound that inhibits the formation of hydrogen bonds. This chemical it is commonly used in fact for the study of ssDNA as it were a "pure" polyelectrolyte [52].

First studies of the force extension curve of ssDNA have been carried out in the group of Bustamante [50]. The force-extension curves of a ssDNA melted from the λ-phage DNA at 150 mM NaCl solution have been published. The strategy that have been used to obtain ssDNA, is the following: a dsDNA molecule is attached between beads and the melting is induced using distilled water or formaldehyde. It has been also showed that the behavior of the force extension curve depends deeply at different salt condition, in particular at low salt (2mM NaCl) and in presence of divalent salt (5mM $MgCl_2$) [52]. It has been argued that the behavior at high salt concentration, can be explained by the formation secondary structure.

Montanari and Mezard have done a theoretical analysis of the behavior of a generic polymer chain capable to bend on itself forming hairpins [57]. The force extension curve obtained by this model were compatible with the behavior of the ssDNA at high divalent salt concentration. In Figure 2.1 is reported the comparison between the model proposed by Montanari and the data of [52].

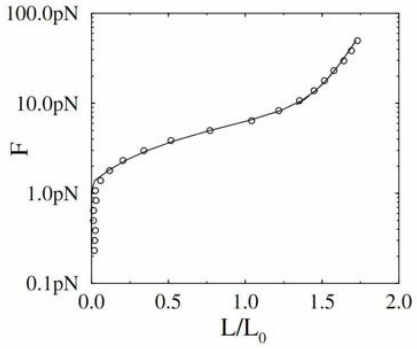

Figure 2.1: Comparison between the force extension curve of charomid ssDNA of [52] and the model proposed by Montanari. Reproduced from [57].

Toan, Marenduzzo and Micheletti proposed a model, the Thick Chain (TC) model [58, 59] that can be used to infer the effective thickness of polyelectrolytes from stretching measurements. In this model the excluded volume effects are included for a polymer described as a tube of uniform cross-section in order to describe the mechanical response of a polymer under a stretching force. Given the thickness, the persistence length of the chain and the contour length, the model provides a relation between the force applied and the extension of the polymer. This model has been proficiently used to describe the force extension curve of an homopolymeric nucleic acid Poly(U) [59]. In Figure 2.1 are reported the comparison between the TC model and the data of the of poly(U) from [52]

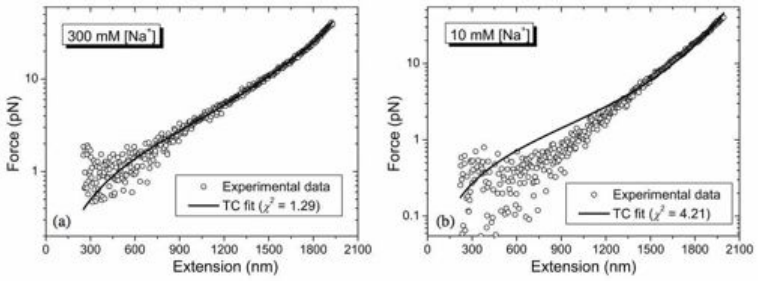

Figure 2.2: Application of the TC model to poly(U) data for (a) 300 mM [Na^+] and (b) 10 mM [Na^+]. Experimental data reproduced from [60] are shown as open circles while the fit with the TC model is denoted with a solid line.

2.3 Methods

The protocol for obtaining force extension curves for ssDNA consists of several phases that are described hereafter.

2.3.1 Materials

All the experiments were performed using a dual beam force measuring optical trap as described in Chapter 1. (A more detailed description of the setup can be find in the Appendix.)

The molecules that are used in the experiment are long hairpins (6838 bps). The hairpins are synthesized from a segment of λ-DNA to which the loop and the DNA handles have been attached by biochemical reactions (see Appendix for the details). This construct has been used previously for single-molecule derivation of salt dependent base-pair free energies in DNA [61].

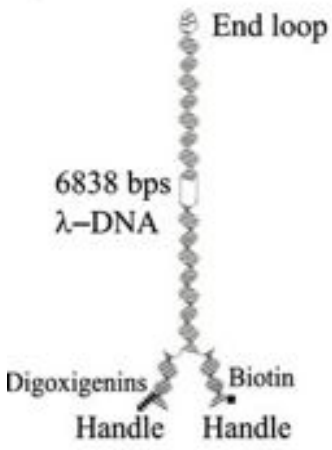

Figure 2.3: Scheme molecule used in the experiments. Reproduced from [61].

In figure 2.3 there is a schematic representation of the molecule. The two ends have been also functionalized with two different molecules: to one end with biotin, to the other several digoxigenins. These chemical compounds are able to selectively bound to specific proteins, respectively streptavidin and antidigoxigenin.

This specific interaction is exploited in order to attach the molecule to the beads and hence to manipulate the molecules via the optical tweezers.

The beads used are polystyrene microbeads of 3 μm coated either with streptavidin or antidigoxigenin (see Appendix for the details).

The buffer solutions used for the experiments are TE buffer at different concentration of NaCl (10, 25, 50, 100, 250, 500 and 1000 mM). The buffer with divalent salt contained 10mM Tris $\cdot$ HCl and different concentration of $MgCl_2$ (0.5, 1, 2, 4, 10 mM).

2.3.2 Attachment of the hairpins to the beads

The first step requires that the molecules are bounded to the polystyrene microspheres. Streptavidin beads (SA beads) are incubated for 20-30 minutes with the synthesized hairpins in TE buffer solution at room temperature. During this time the biotin labeled handle of the molecules bounds to the beads. The second attachment is obtained inside the microfluidic chamber. An anti-digoxigenin antibody-coated bead (AD bead) is positioned at the tip of the micropipette by air suction. By putting in contact a previously incubated SA bead with an AD bead, one could attach one or more molecule. It is quite easy to find a good connection between the beads and the molecule. A stable attachment (up to a force of 40 pN) of the molecule to the beads is obtained in just one or two attempts.Figure 2.4 reports a schematic representation of the connections between the beads and the molecular construct.

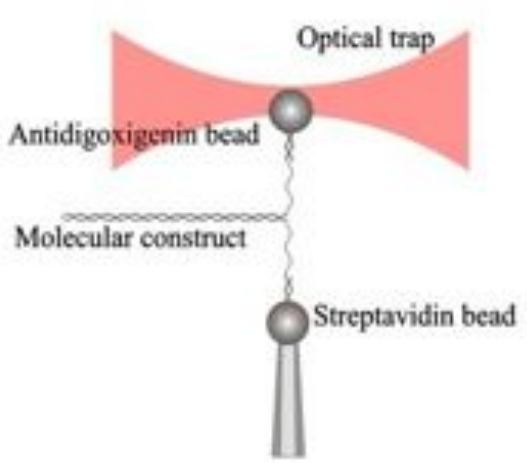

Figure 2.4: Scheme illustrating the connections between hairpin and polystyrene beads. Reproduced from [61].

2.3.3 Unzipping of the hairpin

The optically trapped SA bead is moved away from AD bead at a constant pulling rate of 50 nm/s. The tethered hairpin starts unzipping (see Figure 2.6, step 1) showing a characteristic pattern with climbs and rips. This sawtooth pattern is closely related to the sequence of the hairpin [61]. The climbs are related to the tension needed to detach the two strands. When the strands detach, the tension is released and hence the force lowers (see Figure 2.5).

For the sequence used in our experiments, the mean unzipping force is between 10 and 20 pN varying with salt concentration. When the hairpin is completely unzipped, the force increases monotonically with the distance of the beads. Typically when the force reaches values higher than 20 pN the hairpin is unzipped.

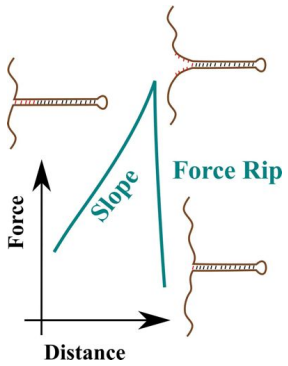

Figure 2.5: Simple scheme representing the events causing unzipping pattern. Reproduced from [61].

2.3.4 Flushing the oligonucleotide solution and releasing

At this point (see Figure 2.6, step 2) a solution of the same buffer added with a small concentration (250 nM) of an oligonucleotide with a designed sequence is flushed in the chamber. The sequence of the oligonucleotide is 30 nt long and it is complementary to the loop region of the hairpin. Once the force of 40 pN is reached, the beads are approached with constant pulling rate. If an oligo is attached to the loop region, the reformation of the hairpin is inhibited. In this case the releasing of the molecule shows a behavior compatible with a molecule of ssDNA with a number of bases doubled respect to the number of base pairs of the hairpin (see Figure 2.6, step 3). It is possible to reach forces up to 0.5-1 pN without observing the reformation of the hairpin. If the hairpin is reformed a sudden jump up to the mean unzipping force of the hairpin is observed (see Figure 2.7). Increasing again the force, the sawtooth pattern is recovered. Releasing force-extension curves have been collected for at least 3 molecule for every concentration.

The buffer solutions used contained 10mM Tris $\cdot$ HCl (pH 7.5), 1 mM EDTA and different concentration of NaCl (10, 25, 50, 100, 250, 500 and 1000 mM). The buffer

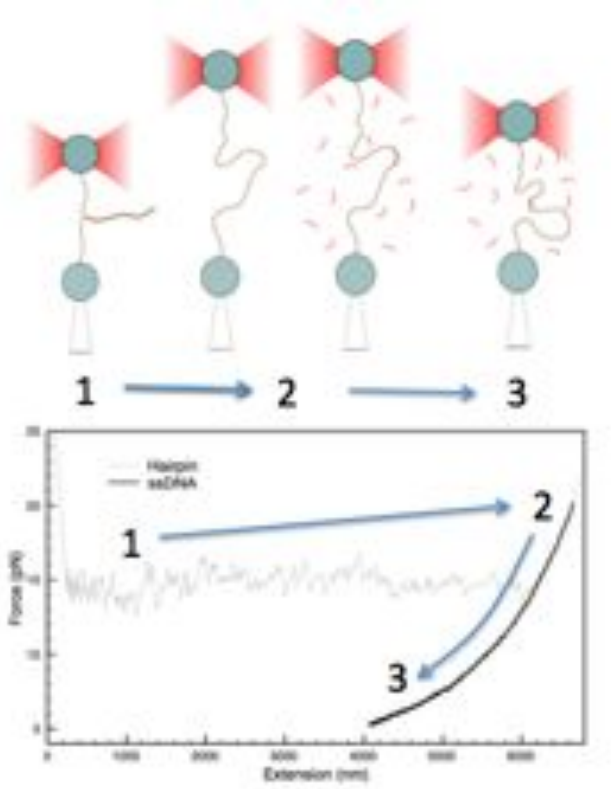

Figure 2.6: Scheme of the procedure used in our experiments to obtain force-extension curves of ssDNA.

with divalent salt contained 10mM Tris $\cdot$ HCl and different concentration of $MgCl_2$ (0.5, 1, 2, 4, 10 mM).

2.3.5 From force distance curves to force extension curves

The force distance curves of the ssDNA are converted to a force extension curve subtracting the contribution of the optical trap. The potential energy of the bead in the trap can be approximated as harmonic, so the extension or end-to-end distance of the ssDNA molecule x can be written as

$$x = x_d - \frac{f}{k} \tag{2.1}$$

where x_d is the measured distance, f is the force and k is the stiffness of the optical trap. The value of the stiffness of the optical trap is about 0.07 pN/nm. Then the

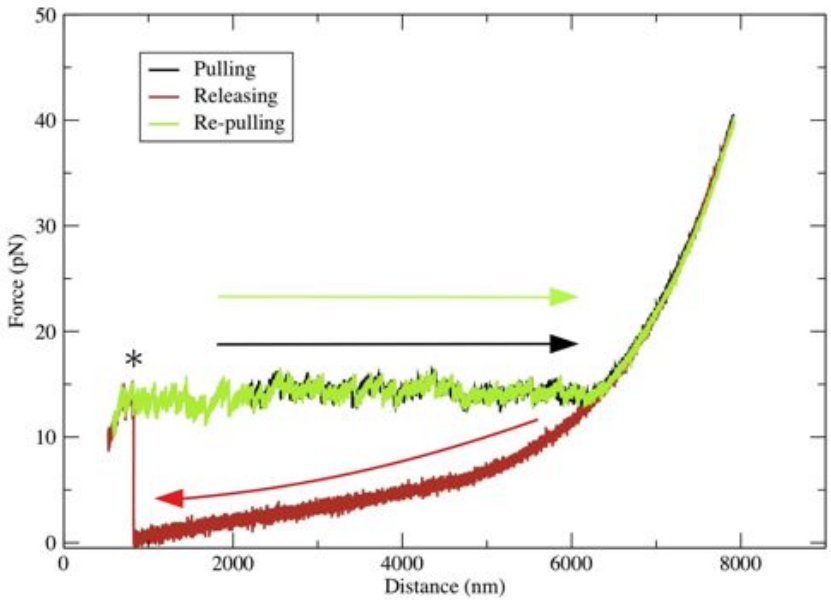

Figure 2.7: Cycle of pulling and releasing for an hairpin in TE with 100 mM of NaCl. The reformation of the hairpin is highlighted with an asterisk.

curves are aligned using the unzipping pattern of the hairpin collected up to 40pN [61]. The force extension curves of the hairpins can be easily aligned because of the sequence dependence of the pattern. The force extension curve of ssDNA is than aligned on top of the ssDNA part of the extension curve of the hairpin.

2.4 Experimental Results

2.4.1 Unzipping of hairpins

Here we report the unzipping pattern obtained from the experiments both in monovalent and in divalent salt conditions. Figure 2.8 shows the unzipping pattern for one molecule in the case of NaCl and $MgCl_2$. The sawtooth patterns of this hairpin has been characterized previously [61]. For the case of monovalent salt, the mean unzipping force (MUF) is measured and compared with the data of literature in order to have a control on the synthesis of the molecules. The MUF is obtained by averaging the sawtooth pattern in the range between 1000 and 6000 nm. As shown in the inset of Figure 2.8, the agreement of the data in NaCl solutions is remarkable. For the data in $MgCl_2$ there are no data from literature to which compare the results. However the pattern of unzipping is almost identical to the one found in the case of NaCl and the MUF increases, increasing the divalent salt concentration.

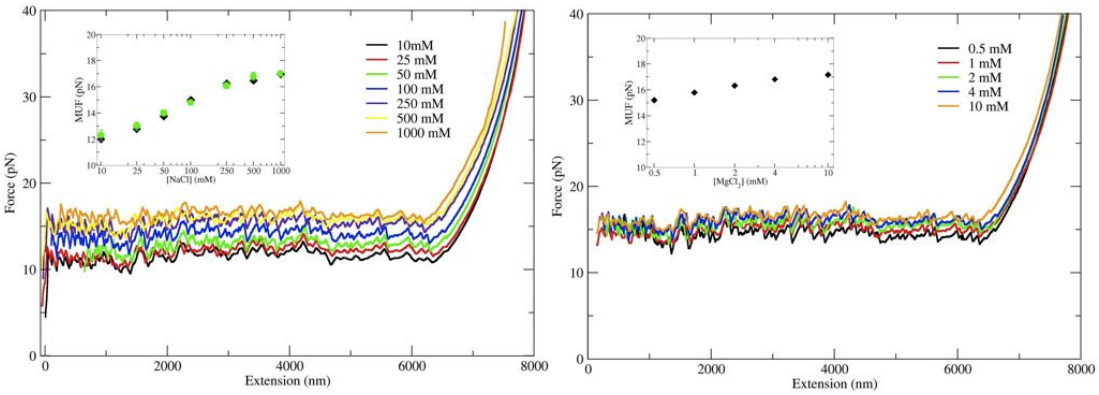

(a) NaCl **(b)** MgCl

Figure 2.8: Unzipping of the molecular construct varying concentration in TE buffer solution. In the inset the mean unzipping force of the hairpins is reported (black diamonds). In the case of NaCl, the comparison with data of [61] (green circles) is also reported

2.4.2 Results with monovalent salt (NaCl)

In Figure 2.9 the force extension curves at different monovalent salt concentration have been reported. For each concentration two force-extension curves are shown. For all the curves, increasing the extension, also the force measured increases. At low forces (up to

10 pN), a behavior compatible with the formation of secondary structure [52, 57] can be observed for the experiments carried out at monovalent concentration higher than 100 mM. At low force (i.e. around 5 pN) the higher the salt concentration, the shorter the molecular extension. This can be reasonably explained by considering that the formation of secondary structure reduces the effective length of the ssDNA. In fact, if a secondary structure is formed along the filament, the effective contour length decreases (see figure 2.10)

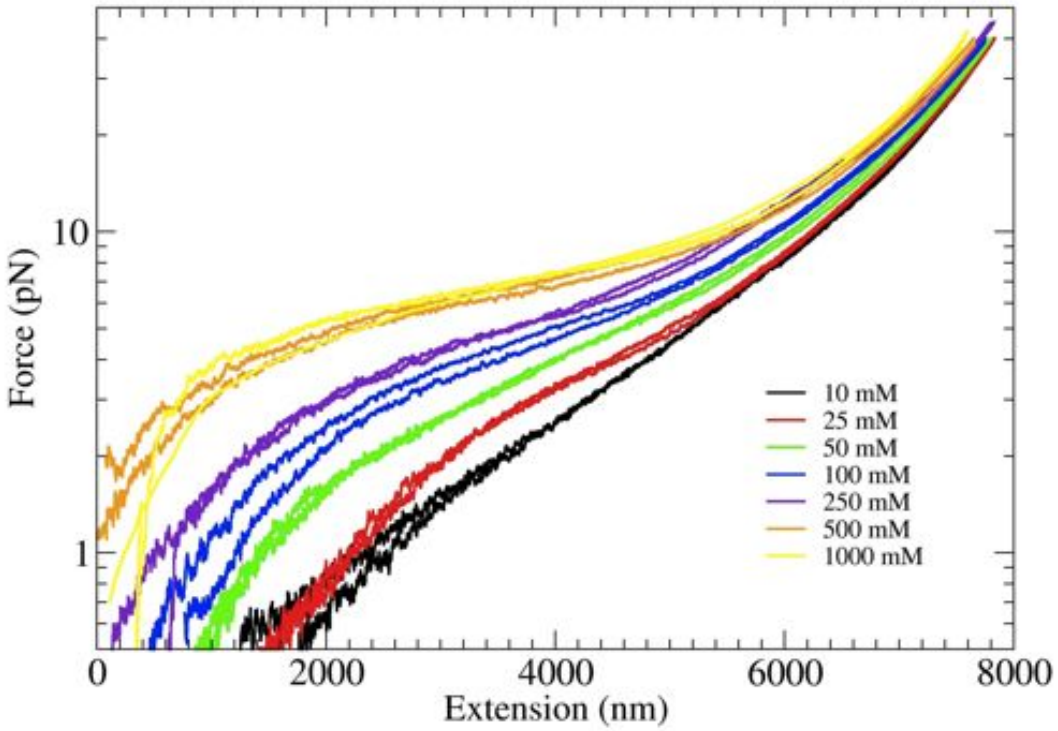

Figure 2.9: Experiments varying NaCl concentration in TE buffer solution.

One should expect that due to the large number of secondary structure, the individual closing (or alternatively the opening when the molecule is pulled) of these structural elements should produce clear signatures in the force extension curves. However this is not observed in the experiment of stretching of ssDNA.

This can be explained considering mainly three effects [62]: the floppiness of the ssDNA, the superimposition of alternative secondary structures and the compensation effect [63].

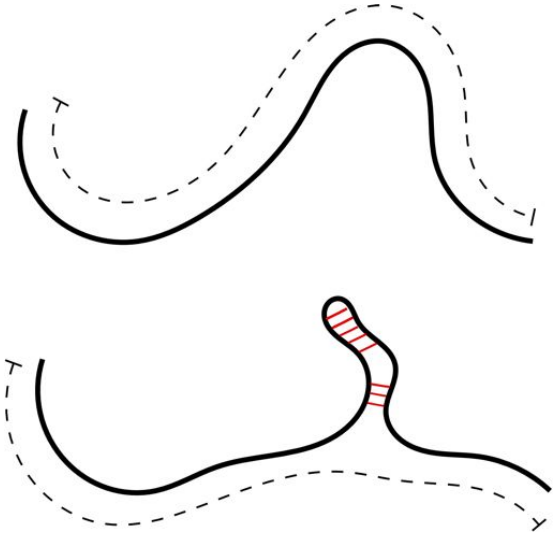

Figure 2.10: Pictorial representation of the effect of secondary structure formation to contour length (drawn with the dashed line).

The sub-optimal configurations have similar free energy, so the system can thermally explore all these configurations (if the energy barriers can be overcome). Moreover the change in extension of individual structural subunits can compensate each other since the profile is measured along the total extension. When several structural elements are pulled in parallel, thermal fluctuation can open a given number of bases of one secondary structure and meanwhile it may reclose stretches of base-pairs in other parts of the chain.

2.5 Results with divalent salt ($MgCl_2$)

In Figure 2.11 the force extension curves at different divalent salt concentration have been reported. For every concentration 2 force-extension curves are reported. As shown in the case of monovalent salt, the plateau that is evidence of secondary structure formation becomes more prominent while the salt concentration increases. The increase in the case of divalent salt is even bigger compared to the case of monovalent salt. At 10 mM of $MgCl_2$ the plateau is comparable with the one observed in the case of 1 M NaCl concentration. A possible explanation of the increasing of the secondary structure formation and hence the formation of the plateau, can be give by considering that base pairing is stabilized at higher salt concentration [64]. Adding to that, at high salt

condition, Debye screening length is small (0.304 nm at 1 M NaCl), so the electrostatic repulsion between the phosphates is screened and the bases can pair with hydrogen bonding.

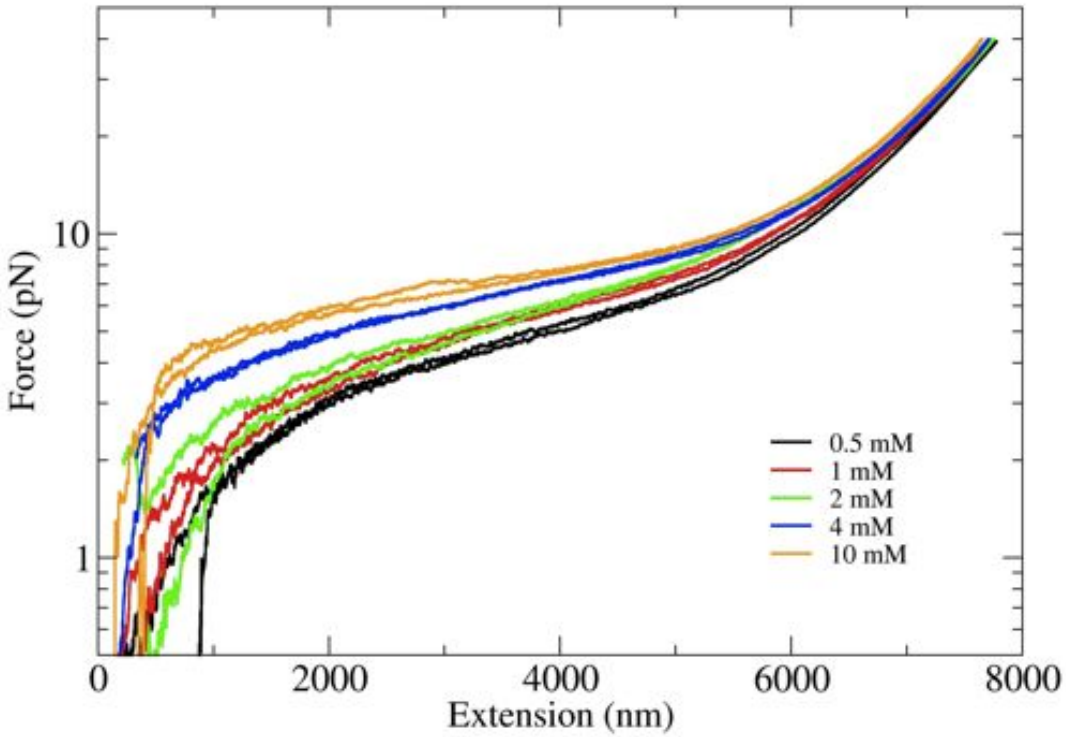

Figure 2.11: Experiments varying $MgCl_2$ concentration in TE buffer solution

2.6 Analysis of the force-extension curves of ssDNA

2.6.1 Analysis with Worm Like Chain

In order to quantify with a model the elastic behavior of the force extension curves of ssDNA, we performed fit of the data with a well known model in literature: the Worm Like Chain model [24].

It has been shown theoretically that the behavior of the extension of ssDNA in the range between 4 to 50 pN is compatible with the Worm Like Chain model [65]. Here, the approximated formula of Marko and Siggia (Eq. 1.11) is used.

The force extension curves have been fitted only between 10 to 40 pN in order to avoid the presence of secondary structure. In fact the secondary structures should disappear at forces larger than 10-15 pN, enough to unzip DNA [66]. In tables 2.1 and 2.2 are reported the persistence length, l_p and contour length, L_c obtained by the fits. For every concentration the value of the persistence length is averaged on curves from 3 different molecules.

Table 2.1: Persistence length obtained by the fit between 10-40 pN of the force extension curves in the case of monovalent salt

[NaCl] (mM)	Persistence Length (nm)	St.Dev. (nm)	Contour Length (μm)	St.Dev. μm
10	1.19	0.06	9.21	0.07
25	1.04	0.06	9.36	0.07
50	0.99	0.05	9.34	0.06
100	0.87	0.04	9.48	0.09
250	0.73	0.04	9.59	0.09
500	0.78	0.04	9.46	0.07
1000	0.76	0.05	9.53	0.07

In Figures 2.12 and 2.13, it is reported a comparison between the fit of the data carried out in the range 10-40 pN with the data in the whole range for the case of NaCl and $MgCl_2$. The comparison shows that the fit of the persistence length describes well the curves in the range of the fit, but it cannot be extended to describe the force extension curve at force lower that 10 pN. In particular at these forces, positive deviations to the WLC model can be observed at concentration higher than 100 mM

Table 2.2: Persistence length obtained by the fit between 10-40 pN of the force extension curves in the case of divalent salt

$[MgCl_2]$ (mM)	Persistence Length (nm)	St.Dev. (nm)	Contour Length (μm)	St.Dev. μm
0.5	0.93	0.06	9.37	0.09
1	0.86	0.04	9.42	0.05
2	0.78	0.04	9.55	0.06
4	0.79	0.05	9.50	0.05
10	0.75	0.04	9.49	0.05

for monovalent salt and in the whole range studied for the divalent salt. Also at monovalent concentration lower than 50 mM, some deviations at forces below 10 pN, can be observed. This discrepancy at low salt concentration can be attributed to excluded volume effects [52]. In fact at low concentrations, the Debye length can be bigger than the persistence length of the ssDNA, resulting in an interplay between the possibility of the molecule to bend and the electrostatics.

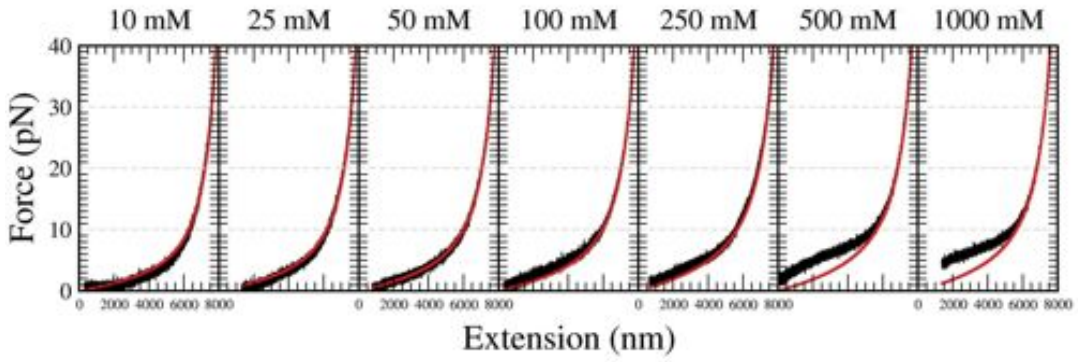

Figure 2.12: Comparison between fit with WLC model of the data in the range 10-40 pN (in red) with the data on the whole range measured (in black) in the case of TE buffer at different NaCl concentration

2.6.2 Comparison with force extension curves of ssDNA

Here we present the comparison with the force extension curves of ssDNA reported in [61]. The data presented in that publication were obtained with a different molecular

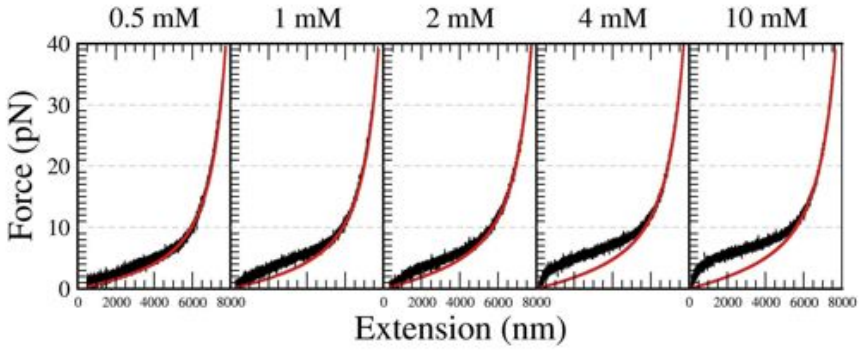

Figure 2.13: Comparison between fit with WLC mode of the data in the range 10-40 pN (in red) with the data on the whole range measured (in black) in the case of TE buffer at different $MgCl_2$ concentration

construct and protocol. The instrumental setup is the same used here, but the molecule is a dsDNA 3000 bps long. One of the two strands is functionalized with biotin at 5' end and with digoxigenin at 3'. The protocol for the attachment of the construct to the beads is similar but a chemical denaturation with NaOH is also performed. In this way a strand of ssDNA is obtained for the measurement of force extension curve.

It must be stressed that this technique present several difficulties because the second connection in the chamber is hard to obtain. Indeed ssDNA tends to attach a-specifically to the beads and hence picking up a molecule requires a large number of attempts.

In order to perform the comparison between ssDNA obtained from the hairpin with the oligo and the molecule of 3000 bps, the extension has been divided by the contour length obtained by the fit with WLC at forces higher than 10 pN. Figure 2.14 shows this comparison. The qualitative agreement between the curves is quite remarkable at small concentrations (10-100 mM). At 1 M NaCl concentration there is also agreement at forces higher than 15 pN. Below that threshold, the behavior is quite different. A possible explanation to this discrepancy could be that the elastic response in presence of basepairing interaction depends on the size of the polymer.

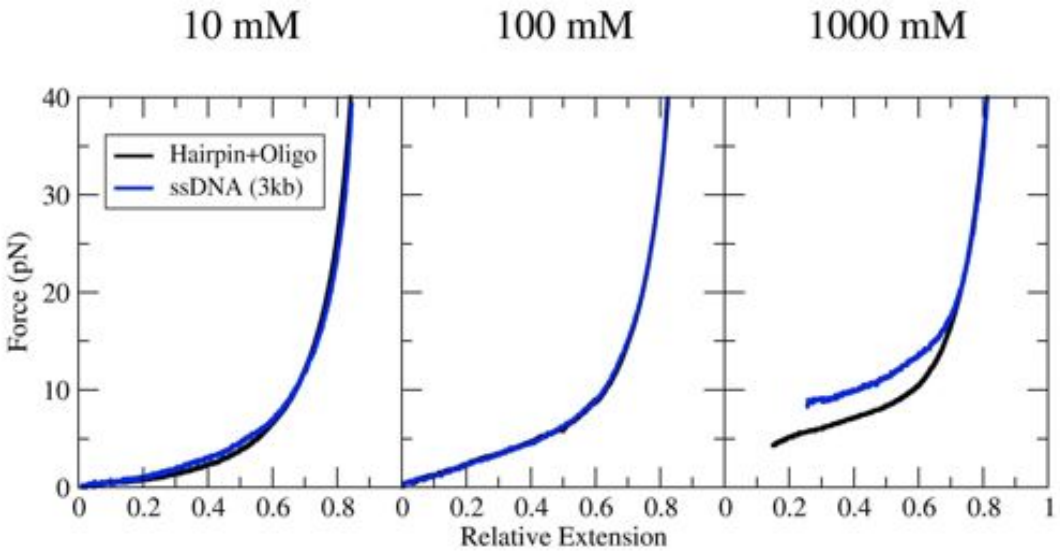

Figure 2.14: Comparison between relative extension of the data obtained with the method described here (in black) and the data reported in [61] for a ssDNA of 3 kbs (in blue)

2.6.3 Analysis of the behavior of persistence length at different ionic conditions

A graphical representation of the data is reported in Figure 2.15. In literature [59, 65, 67], it has been showed that the persistence length, Lp, for charged semi-flexible polymer can be written as

$$l_p = l_p^0 + l_p^{el} \tag{2.2}$$

where l_p^0 is the intrinsic persistence length and l_p^{el} is an electrostatic contribution that depends linearly on Debye screening length and consequently on the inverse of the square root concentration of ions in solution, so $l_p^{el} \propto \frac{1}{\sqrt{[Ion]}}$.

The data obtained for l_p have been plotted as function of the inverse of the squared root concentration, in order to show the dependence on the concentration. In figure 2.15 the data from [61] are also reported.

The comparison shows that the values obtained for the persistence length in presence of NaCl with both methods are comparable. The linear fit of the data have been shown also in the graph for both monovalent and divalent salt. For both salts, a value of l_p^0 equal to 0.7 nm is obtained. This value is in extremely good agreement with the values

reported for single stranded nucleic acids, in particular for poly-U (0.67 nm) [59, 60, 65] and for chemical denatured ssDNA (0.6 nm) [54, 55]

From the comparison between monovalent and divalent salt, it emerges that the linear behavior can collapse into a single linear trend by multiplying the concentration of $MgCl_2$ by a factor 100. These results suggest the hypothesis that magnesium is roughly 100 times more efficient than sodium in affecting the elastic properties of ssDNA. This cannot be explained by Debye-Hueckel picture of diffuse cloud of screening counterions [56] but using strongly correlated liquid models of counterion/macroions interaction [68]. With this model a ratio between 50 to 200 is expected [56]. Moreover results that are consistent with our findings can be observed in the case of the folding of the ribozyme [69] and in pulling experiments of RNA [70]

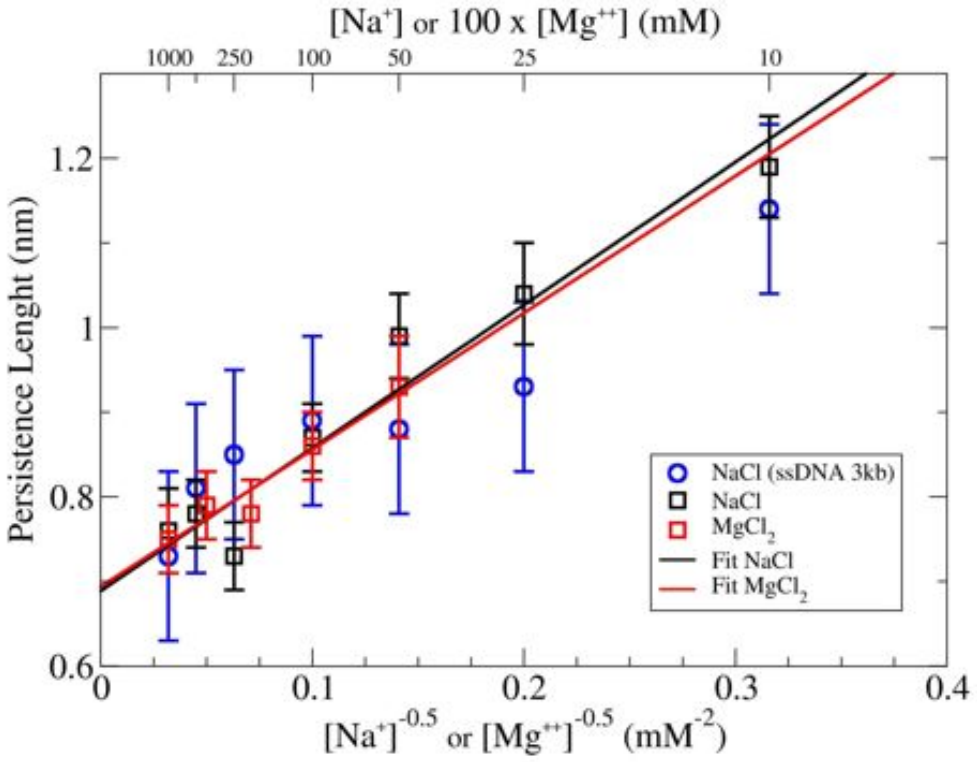

Figure 2.15: Persistence length values for the ssDNA at different salt conditions: in black and red data in presence of NaCl and $MgCl_2$respectively. In blue, the data from [61]. Magnesium concentrations have been multiplied by 100.

2.6.4 Comparison with Thick Chain Model: indications on effective thickness

In order to analyze the effect of the excluded volume, the curves of the force extension curves at low monovalent salt concentration (10-50 mM of NaCl) have been fitted with the Thick Chain (TC) Model in the whole range of force studied. With this model, it is possible to extract values for the thickness of the biopolymer [58, 59] and the persistence length. The fits are reported in Figure 2.16 and the values obtained from the fit are reported in Table 2.3 .

The values obtained are comparable with the one found obtained from the fitting of homopolymers (for Poly-U, Δ is about 0.9-0.8 nm [59] in the same concentration range used in our experiments). From the fitting, it emerges also that the effective thickness decreases increasing the salt concentration. This could be interpreted in terms of screening of the ions: the effective thickness appears smaller if the phosphate backbone is more screened.

Table 2.3: Geometric parameters obtained by the fit with TC model of the force extension curves at low monovalent salt concentration

[NaCl] (mM)	Δ (nm)	St.Dev. (nm)	l_p (nm)	St.Dev (nm)	Contour Length (μm)	St.Dev. μm
10	0.83	0.03	1.13	0.08	8.48	0.09
25	0.74	0.04	1.12	0.08	8.57	0.09
50	0.71	0.02	0.85	0.07	8.46	0.09

2.7 Estimate of the fraction of unpaired bases of ssDNA

In order to have a quantitative measure of the fraction of ssDNA that forms secondary structure, we used the WLC model to estimate the effective contour length L_c^{Eff}. This is carried out in the following way. For a force extension curve, we extracted the effective contour length fixing the value of the persistence length to the one obtained in the range 10-40 pN. If the model of the WLC described the whole range of measured forces, the effective contour length would be equal to the one measured in the range 10-40 pN. In other words, the length should not depend on the force also at small forces.

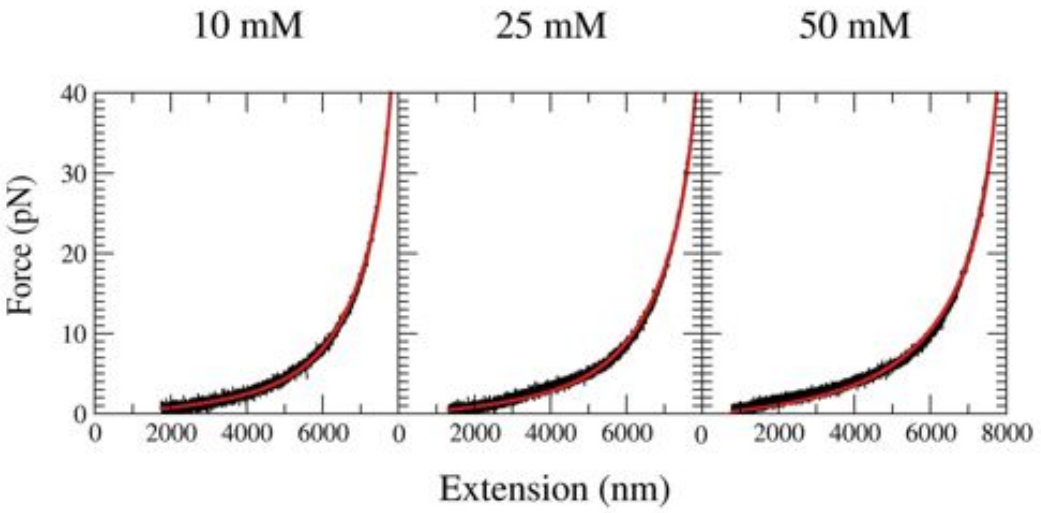

Figure 2.16: Comparison between fit with TC model (in red) with the experimental data (in black) on the whole range measured at low NaCl concentrations.

In Figure 2.17 the values of the effective contour length are plotted against the force applied to the hairpin.

For the case of NaCl at concentration below 50 mM, L_c^{Eff} increases while the force decreases. This effect could be related to excluded volume effect that become prominent at low salt concentration.

At monovalent salt concentration higher than 100 mM, and in all explored concentration of divalent salt, L_c^{Eff} decreases when the force decreases. This can be explained simply considering that, at small force, there is more possibility to form secondary structure because the molecule is not stretched. The fraction of unpaired ssDNA bases is simply given by the ratio $\phi(f) = \frac{L_c^{Eff}}{L_c^{10-40}}$. At low force (below 5pN), the higher the salt concentration the shorter the effective contour length. This means that at high monovalent salt concentration (or in presence of divalent salt) the fraction of base paired DNA increases. At the lowest forces (1-2 pN), the fraction of unpaired bases can reach values of about 20-40%of the one at the highest salt concentration (namely 1 M of NaCl and 10 mM of $MgCl_2$)

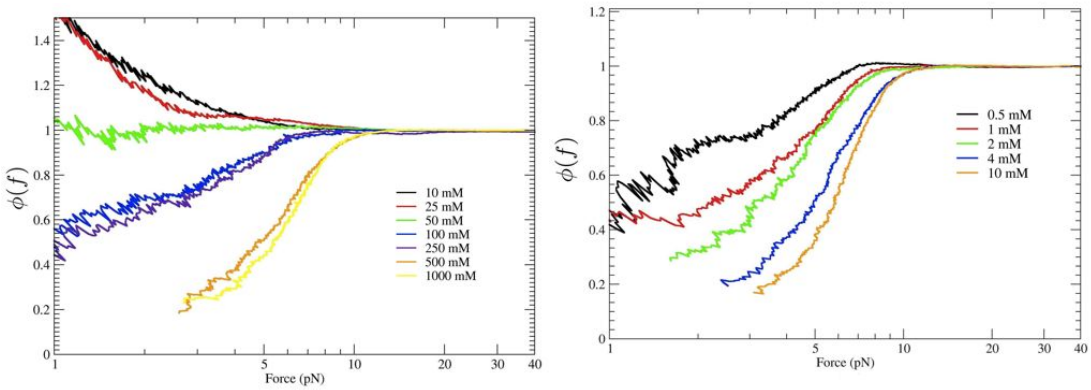

(a) NaCl **(b)** $MgCl_2$

Figure 2.17: Estimation of the fraction of unpaired ssDNA bases from effective contour length for different salt concentration varying the pulling force applied to the molecular construct.

2.8 Summary and conclusions

In this chapter it has been presented a promising technique that can be fruitfully used to study the formation of secondary structure in ssDNA. A wide range of different concentrations of monovalent and divalent salt has been explored. In both cases we observed the formation of a plateau in the force-extension curve of the ssDNA, evidence of secondary structure formation. This feature increases while increasing the salt concentration and it has been explained considering that base pairing is stabilized by higher salt concentration.

It has been shown that the persistence length varies linearly with the inverse of the square root concentration of monovalent salt consistently with what shown in [59, 67]. The same behavior can be obtained with divalent salt but with a concentration that is 100 times smaller.

As a further step, it would be very interesting to extend our study to other kind of cations, both monovalent and divalent, such as potassium and calcium. Moreover, a characterization of the effect of the oligo concentration should be taken account in further experiment. This new technique also opens the way to the study of its interaction with chemicals and proteins. In fact the force extension curve of ssDNA in presence of other molecules of biological relevance could be exploited to characterize the behavior of nucleic acids with these.

3

Modeling DNA patches

3.1 Motivation and introduction

Gene expression profiling experiments are useful tools for studying the function of a cell. The genome codes for all the necessary information of the development and activity of an organism [4]. However the specific function of a cell depends on the activity (the regulation and the expression) of the genes. By profiling the gene expression of a cell, one can, for example, distinguish between cells that are in a different cellular phase, or study how cells react to a particular treatment (i.e. pressure or temperature variations, changing in chemical environment, and so forth) [71, 72].

In experiments of gene expression profiling the relative amount of messenger-RNA (mRNA) expressed in two or more experimental conditions is measured. If a change in the abundance of a particular mRNA is detected, it is possible to infer that the gene is involved in the particular variation of the conditions. For example, if a particular cancer cell expresses high levels of mRNA associated to a particular kinases or to a specific receptor, it might be that these proteins play a role in the pathological state [73].

In this framework, gene expression microarrays are powerful tools for early-stage disease identification [74, 75, 76]. Microarrays are a collection of microscopic spots of ssDNA with known sequence attached to a surface. These specific sequences have a typical length of 10-100 nucleotides. The operation principle is based on the detection of the molecules complementary to the sequences in the spots [72, 73].

The genetic material is extracted from the cells under study and it is cut into small

sequences. These are functionalized with a fluorophore and put in contact with the microarray spots. If a sequence obtained from the genetic material is complementary to the strands in one spot of the microarray, than it hybridizes there. The higher the number of sequences hybridized in the spot, the higher the signal of fluorescence. In this way it is possible to know the sequences that are the most expressed by the cell.

Recently the quest for increasing miniaturization has spurred the development of nano-arrays of DNA oligonucleotides immobilized on a surface. Nano-arrays of DNA consist of patches of nanografted assembled monolayers (NAMs) of DNA. NAMs are produced with an Atomic Force Microscope (AFM) by scanning a given monolayer of molecules attached to a surface with the tip operated at high load in a liquid environment that contains oligonucleotides. In such DNA array, the hybridization with the complementary sequence is detected by means of mechanical probing of the patches with an AFM tip. By applying different loads at the tip during the imaging of the DNA patch, it is possible to detect whether the patch has undergone hybridization or not. In fact, by considering the difference in structure and elastic properties of ssDNA and dsDNA, we expect a different response of the patch to compression. Within this scheme the ssDNA patches that have been surface-immobilized by AFM grafting are used as mechanical transducers for the presence of complementary DNA strands in solution and for the hybridization efficiency, that is the percentage of hybridized strands in the patch [9, 77].

The partner group of Dr. Loredana Casalis gave an experimental proof of principle of this idea [9]. They showed that DNA patches of different densities have a different height when compressed by means of an AFM tip. By applying increasing loads at the tip during the imaging, it is possible to compress the patch and measure a height variation. The height variation in response to an applied load depends on the intrinsic mechanical properties of the chain (ssDNA and dsDNA) and on the surface densities. The qualitative relation that has been experimentally observed between applied load and height variation could be effectively exploited by turning it into a quantitative relation.

Here we explore the possibility to make progress in this direction by using coarse grained DNA models to study the response to mechanical compression of ssDNA and dsDNA.

A coarse grained model for the DNA patches is presented in this chapter. The principal objective of this model is to give an estimate of the height of the patch under a given compressive load. The model is used to describe the mechanical response upon compression of the DNA patches at different surface densities. From this we obtain a phenomenological formula that captures the relation between the force applied to patch and the height measured during the simulation. Successively, this relation can be used to make a comparison of the mechanical response of the model with the experimental one.

However a direct comparison between the results of the simulation and the experiments is not possible. In fact, one should consider how the AFM tip compresses the DNA patches because the load applied by the tip is spread on the surface that is in contact with the patch. For this reason, the tip geometry must be introduced in modeling the behavior of the DNA patch under compression. In this chapter we describe how this effect is taken into account.

Height measurement of NAMs at different applied load have been performed within the framework of a collaboration between SISSA and the Senil Lab. In the next chapter, first a validation of the model described here can be obtained from their measures. In turn, using this relationship, we obtain an estimate of two quantities that are typically difficult to measure directly in experiments, namely the patch surface density and the sample hybridization efficiency.

3.2 DNA patches: description of the system and Hamiltonian of the model

The DNA NAMs model considered here is tailored to capture the main features of the experimental set up and condition used by the Senil lab. A DNA NAM consists of a patch of DNA molecules attached to a surface.

The molecules can be either ss or ds DNA. The linkage between the DNA molecules and the gold surface is obtained by a covalent bond. DNA molecules are functionalized with an alkyl spacer (of few carbonyl groups) that bears a thiol functional group. This moiety can be selectively bounded on the gold of the surface. Figure 3.1 offers a schematic picture of dsDNA functionalized with an alkyl spacer.

Figure 3.1: Schematic representation of a ds-DNA with 15 basepairs functionalized with an alkyl spacer bearing thiol moiety (in orange).

The oligonucleotide that can be attached on the surface consist of few tens of nucleotides. In the experiments considered here the length of the oligos is equal to 24 nucleotides. Patches are produced by nano-grafting ssDNA and dsDNA on a golden surface. The typical dimension of these patches is about 1 μm^2 so every patch contains several thousands of molecules. Figure 3.2 provides a cartoon of such DNA patch. The ssDNA NAMs can be put in contact with the complementary sequence of the deposited oligo (hybridization *in situ*). The mechanical probing of the patches before and after hybridization is carried out at high salt conditions, namely 1 M NaCl.

A minimal model for the DNA patch can be built by describng the N ssDNA and dsDNA filaments in the patch as chains of beads subject to the following potential energy:

$$\sum_{I,J=1}^{N} H_I^{BR} + H_I^{SA} + H_I^{attract} + H_I^{wall} + H_{I,J}^{beads} \tag{3.1}$$

where H^{SA} contains the self-avoidance along the chain (Eq. 3.3) and H^{BR} is the bending rigidity contribution (Eq. 3.4), ; $H^{attract}$ models the attraction with the surface

(Eq. 3.5); H^{beads} and H^{wall} account for the steric hindrance of the chains with themselves and with the surface, respectively (Eq. 3.6 and 3.7). In following sections every term of the the potential energy in formula 3.1 will be discussed.

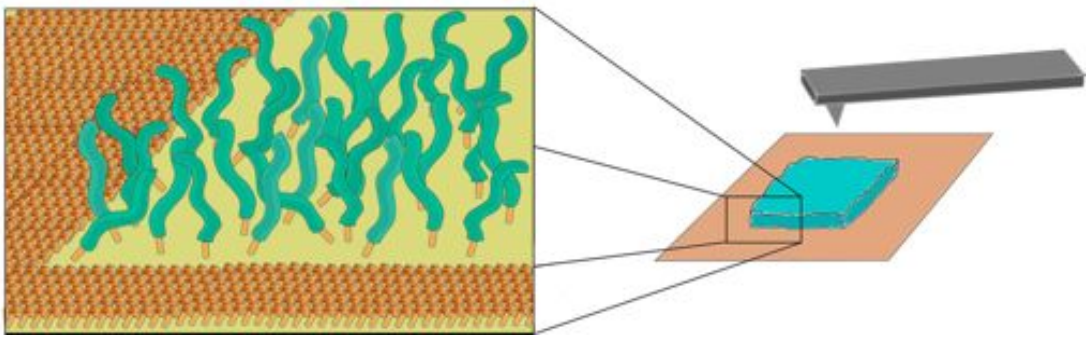

Figure 3.2: Cartoon representing a patch of DNA deposited on a gold surface. On the right a macroscopic picture of the patch and the AFM tip. On the left, in the detail, picture of the chains within the patch. DNA molecules are represented in light blue and the alkyl spacer is represented in orange

3.3 Excluded volume of DNA

ssDNA and dsDNA molecules are modeled as discrete thick chains with appropriate bending rigidity. In the literature such models have been widely used to describe several systems, for example in estimating the probability of a segment of DNA of forming knot in solution at different salt condition [78], or modeling the stretching response of nucleic acids homopolymers [58, 59].

Every chain is represented through its backbone and consists of 24 segments of equal length, each segment corresponding to a nucleotide (for ssDNA) or a base-pair (for dsDNA). In both cases, the segment length, l, is set to 0.34 nm, which corresponds to the canonical base-pair separation in B-form dsDNA [3], as well as the axial rise of ssDNA between two consecutive stacked nucleotides [15].

Excluded volume effects are taken into account by considering the backbone as being the centerline of a discrete thick chain having cross-sectional radius Δ (see Figure 3.3). Following the scheme of Gonzalez and Maddocks [79], a finite chain thickness, Δ, limits the possible configurations of the chain. Given $\{\mathbf{r_i}\}$, the position of the points on the centerline, it is possible to check whether this arrangement of segments is compatible

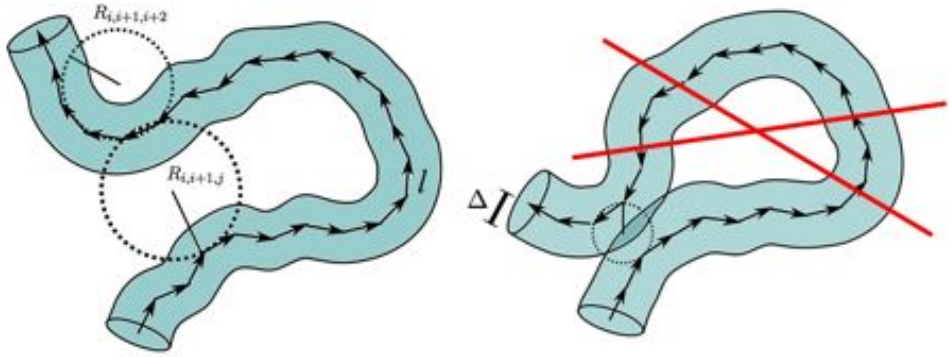

Figure 3.3: A schematic representation of a discretized chain. Excluded volume effects are taken into account using the model of a thick chain. Image shows how the thickness impacts on the radius of curvature. On the left: $R_{i,i+1,i+2}$ gives a local contribution (it is the radius of circumcircle that pass trough three subsequent vertexes of the chain) while $R_{i,i+1,j}$ is a non local contribution to the thickness (it is the radius of the circle passing trough non consecutive vertexes) On the right: prohibited configuration of a chain. If the radius of circumcircle is smaller than δ, the excluded volume region shows a clash.

with a chain of preassigned thickness. $R_{i,j,k}$ is the radius of circumcircle for every triplet of distinct points i, j and k. For every arrangement of the segment of the chain, it is possible to define ρ, the global radius of curvature as the smallest radius amongst all radii of circumcircles, $R_{i,j,k}$. The global radius of curvature, ρ, is defined as

$$\rho = \min_{i,j,k}\{R_{i,j,k}\} \tag{3.2}$$

The self-avoiding potential energy for a chain I is:

$$H_I^{SA} = V_{SA}(\rho_I) \quad \text{with} \quad V_{SA}(\rho_i) = \begin{cases} \infty & \text{if } \rho_I < \Delta_I \\ 0 & \text{if } \rho_I > \Delta_I \end{cases} \tag{3.3}$$

where ρ_I is the global radius of curvature for chain I. This term, present also in the total potential energy of Eq. 3.1, assigns an infinite energy penalty to configurations where the global radius of curvature is smaller than Δ.

With reference to previous formula, Eq. 3.3, the finite thickness introduces both local and non-local constraints on the chain configurations. Consider the radius of curvature of three consecutive bonds, $R_{i,i+1,i+2}$, the local radius of curvature at point i. The constraint imposed by Eq. 3.3 limits the local radius of curvature of the chain to be greater than Δ. This sets a bound on the angle formed by two consecutive

bond. The non-local effect arises by the fact that the two parts of the chain that are distant along the centerline cannot interpenetrate. The non-local radius of curvature of non-consecutive points, $R_{i,i+1,j}$ constrains the distance of minimum approach of any two backbone segments, which cannot be smaller than 2Δ. In Figure 3.3 a cartoon illustrates the effect of this constraint on a discrete chain and the effective excluded volume that results by applying the constraint. For modeling DNA patches, the value of Δ was set equal to 0.45 nm for ssDNA and to 1.25 nm for dsDNA .

Notice that the finite thickness induces a non trivial characteristic length for the tangent-tangent correlation at short arclenght separation [58, 80]. Figure 3.4 shows the graphs of the tangent-tangent correlation function along a chain of 500 segments . This has been evaluated on 10000 independent configurations obtained with a stochastic sampling scheme. (A detailed description of this technique is presented in the following section). In this simulation, we used the same parametrization chosen for modeling DNA patches, that is Δ =0.45 nm for ssDNA, Δ =1.25 nm for dsDNA and l =0.34 in both cases. The tangent-tangent correlation functions can be fitted with a single exponential in order to extract the decay length. Notice that, for a semi-flexible chain without excluded volume, the decay length of the tangent-tangent correlation is equal to the persistence length [23]. The restrictions imposed by steric hindrance on the local radius of curvature are sufficient to endow the ssDNA with a persistence length of about 2 nm (Figure 3.4a) that is sufficient and reasonable for such system. Conversely, chain thickness alone accounts for a persistence length of about 20 nm for dsDNA (see solid lines in Figure 3.4b). This value is about half of the the full persistence length of dsDNA [80] and therefore a bending rigidity term, appropriate to reproduce the persistence length of 50 nm in a discrete piece-wise linear chain, has been introduced for this second type of molecule [81].

3.4 Bending Rigidity

The contribution of the bending rigidity that acts on every I-th chain can be written as:

$$H_I^{BR} = -\varepsilon \sum_{i=2}^{n} \frac{\mathbf{t}_i \cdot \mathbf{t}_{i+1}}{l^2} \quad \text{with} : \begin{cases} \mathbf{t}_i = \mathbf{r}_i - \mathbf{r}_{i-1} \\ |\mathbf{t}_i| = l \end{cases} \tag{3.4}$$

where $\mathbf{r_i}$ is the position of the i-th vertex in the chain of segments and the ε is the bending rigidity. For a chain with no steric hindrance the amplitude of the ε is simply

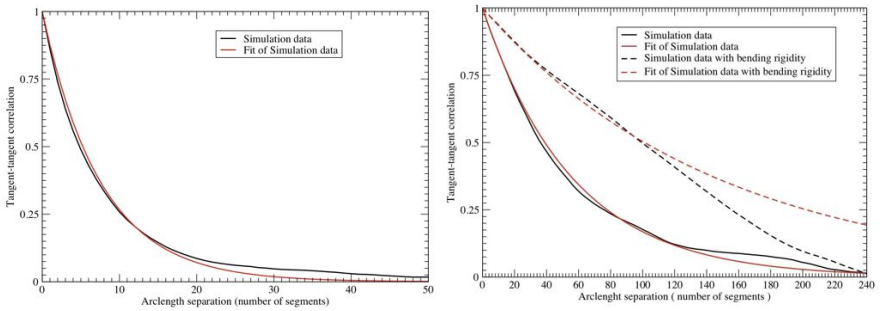

(a) ssDNA **(b)** dsDNA

Figure 3.4: Tangent-tangent correlation between segments along the chain for dsDNA and ssDNA. Black curves show results from 10000 independent configuration obtained by simulating a chain of 500 segments. Red curves shows a fit with a single exponential .

related to the persistence length l_p by the expression $\varepsilon = k_B T \frac{l_p}{l}$, where k_B is the Boltzmann constant and the temperature T is set to 300K. Using a value of ε_{dsDNA} $=147 k_B T$, the decay length of the tangent-tangent correlation function can be fitted with a value equal to 50 nm. (see dashed lines in figure 3.4b)

3.5 The alkyl spacer

In the experimental set-up, the ssDNA and dsDNA molecules are attached to the surface by means of a 1.2 nm-long flexible alkanethiol spacers. Consistently with this fact, the backbones of the model DNA chains are prolonged at one of the ends by a second piece-wise linear chain consisting of 3 segments of length 0.4 nm, and thickness equal to 0.45 nm. Regarding the flexibility of the alkanethiol spacer, the value of the bending rigidity is chosen equal to $\varepsilon_{spacer} = 16 k_B T$, obtaining a persistence length equal to 6.5 nm as reported in the literature for such systems [82, 83]. Notice that each modeled chain consists of two tethered chains (the ss or dsDNA and the linker) with different thickness diameters. The heterogeneity of the thickness between the spacer and the DNA has been taken into account when controlling the constraints on the local and non-local radii of curvature.

A behavior like a rigid rod (see Figure 3.5a) is expected for dsDNA constructs. In fact, considering the length and the number of the segments used in the model, the contour length is equal to 24x0.34nm=8.16 nm that is almost one sixth of the

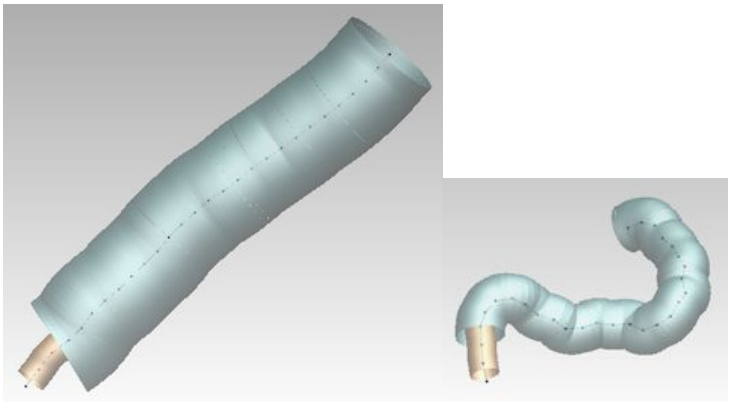

(a) dsDNA **(b)** ssDNA

Figure 3.5: Representation of the DNA+linker constructs in the case of the dsDNA (a) and the ssDNA (b). The effective excluded volume is also represented: in light blue for DNA part and in orange for the spacer

persistence length for dsDNA. By contrast for ssDNA a behavior more similar to a flexible polymer is expected (see Figure 3.5b), because the persistence length is 4 times smaller than the total length.

3.6 Modeling the surface

The surface is modeled as an impenetrable wall: the hard-core repulsion between the DNA molecules and the surface is taken into account by forbidding each chain vertex to lie below a plane corresponding to the gold surface. The plane is the locus of points with coordinates $z = 0$ and the DNA chains lie in the semi-space $z > 0$.

It is known that DNA molecules can adhere on the gold surface [84, 85]. The mechanism with which these molecules interact with the gold surface comes out from a complex interplay of several factors. Key players in this interaction are certainly hydrophobic interactions [46, 47] and electrostatic forces [86].

Therefore, to take into account these effects, a non-specific attractive interaction is introduced between the surface and each vertex of the chain segments at a distance smaller than a threshold distance from the surface.

Gouy-Chapman theory has been used to give an order of magnitude estimate of this interaction [86]. With this theory, it is possible to evaluate the potential energy and ionic distribution of the charges present in solution at increasing distance form the

surface. Free ions in solution form screening layers around charged objects but also away from the surface. In presence of ions, a gold surface can be moderately-polarized. With this model it is possible to give an order of magnitude estimation of the effect of the polarized surface on the charges present in solution. For every negative charge the effective electrostatic potential is a fraction of k_BT and has a range of 1-2 nm [86, 87].

The effect of the surface is captured by the following potential energy term:

$$H_I^{attract} = \sum_{i=2}^{n} V_{attract}\left(r_{z,i}\right) \quad \text{with} \quad V_{attract}\left(r_{z,i}\right) = \begin{cases} \infty & \text{if } r_{z,i} < 0 \\ -\gamma & \text{if } 0 < r_{z,i} < \delta \\ 0 & \text{if } r_{z,i} > \delta \end{cases} \tag{3.5}$$

where δ and γ are, respectively the range and the strength of the interaction potential. Values of δ=2nm and γ=$0.2k_BT$ are chosen in the case of the ssDNA and the alkyl spacer and a value of γ=$0.2k_BT$ is set in the case of dsDNA. In addition, the finite thickness of the chain restricts the maximum angle up to which the first bond (attached to the surface) can bend. This is implemented adding the following contribution to the hamiltonian:

$$H_I^{wall} = \sum_{i=2}^{n} V_{wall}\left(r_{z,i}\right) \quad \text{with} \quad V_{wall}\left(r_{z,i}\right) = \begin{cases} \infty & \text{if } r_{z,i} < \max\left\{\frac{l}{2}, \Delta\sin\left(\theta\right)\right\} \\ 0 & \text{elsewhere} \end{cases} \tag{3.6}$$

where θ is the angle between the vector $\mathbf{t}_i$ and a vector normal to the surface.

3.7 Interaction between the chains of the patch

Excluded volume interactions must be enforced also between distinct chains in the patch. This excluded volume interaction is accounted for by assigning an infinite energy penalty to configurations where two chain vertices of different chains are at a distance smaller that the sum of their thickness radii. An illustration of this constraint is given in Figure 3.6. The contribution to the total hamiltonian that involves the I-th and the J-th chain can be written as:

$$H_{I,J}^{beads} = \sum_{i,j=2}^{n} V_{beads}\left(r_{IJij}\right) \quad \text{with :} \quad V_{beads}\left(r_{IJij}\right) \begin{cases} \infty & \text{if } r_{IJij} < \Delta_{IJij} \\ 0 & \text{elsewhere} \end{cases} \tag{3.7}$$

with r_{IJij} is the distance between the bead i of the chain I and the bead j of the J-chain and Δ_{IJij} is the sum of the radii of the two beads.

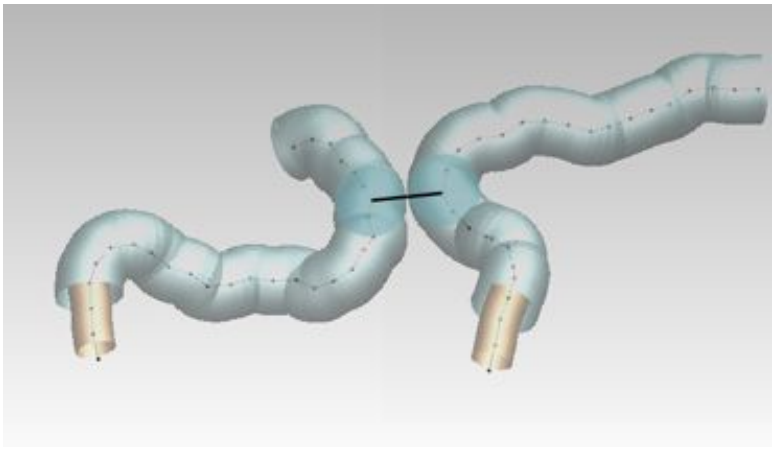

Figure 3.6: Representation of the mutual avoidance between chains. In this case two ssDNA constructs are represented with regions of excluded volume

3.8 Applying a force to the patch: compressive term

Some of the ingredients that are used to model the DNA patches have been described in the previous section. Another term that takes into account the effect of compression of the tip during the imaging must be added to the total potential energy:

$$H^{ext} = \sum_{I=N} f_{ext} \max_i(\{r_{z,i}\}_I) \tag{3.8}$$

where f_{ext} is the external force, acting on the bead at largest height in each chain of the patch. In summary, the total potential energy for a DNA patch is given by:

$$E_{tot} = \sum_{I,J=1}^{N} H_I^{BR} + H_I^{SA} + H_I^{attract} + H_I^{wall} + H_{I,J}^{beads} + H_I^{ext} \tag{3.9}$$

3.9 Monte Carlo Sampling

The equilibrium properties of the model are computed by Monte Carlo sampling of system configurations in canonical equilibrium [88]. Ensemble averages are hence obtained by straightforward arithmetic averages over the observables calculated on the sampled configurations. To sample the configurational space of the system, a series of elementary Monte Carlo steps are adopted. The Monte Carlo evolution involves a series of elementary deformations of the system configuration as described in detail hereafter.

The standard Metropolis criterion [89], is used to accept the new configuration or to reject and retain the previous one. Specifically the Metropolis acceptance criteria is given by:

$$p_{acc} = \min\left(1, \exp\left(-\frac{E - E'}{k_B T}\right)\right) \tag{3.10}$$

where p_{acc} is the probability of acceptance for the move, E' and E are respectively the energy of the old and the new configurations of the system.

For the model of DNA patch, a move is implemented in this way: at every step, a chain of the patch is randomly chosen. A "Crankshaft" or a "Pivot" move is next applied to the chosen chain. The probability is the same for the two moves.

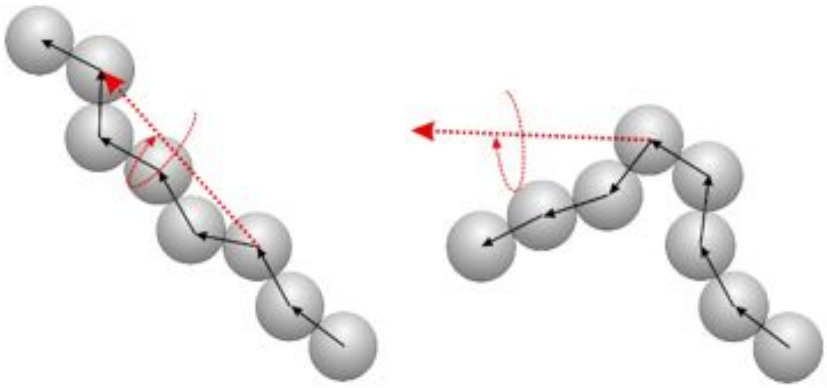

(a) Crankshaft **(b)** Pivot

Figure 3.7: Pictorial representation of the two moves that are usually implemented in the simulations of polymer [88]: (a) "Crankshaft" move and (b) "Pivot move". The red dotted vector represents the axis of rotation around which the configuration is changed.

Figure 3.7 shows a representation of the two moves. During a "Crankshaft" move, two points of the chain with position $\mathbf{r}_i$ and $\mathbf{r}_j$ are chosen randomly. All the points of the chain between i and j are rotated by a random angle around the vector $\mathbf{r}_i - \mathbf{r}_j$. In a "Pivot" move, a point along the chain is chosen randomly and the segment of the chain not attached to the surface is rotated by a random angle around a randomly chosen axis. It has been shown that these moves, if implemented on lattice polymer, satisfy ergodicity criteria. In this case equilibrium is certainly reached [90]. With the moves used in the simulation, it is reasonable to think that also in our case ergodicity

is assured. Notice that inter- o intra-chain steric clashes can result after a move. This would lead to configurations with infinite energy, that causes the rejection of the new conformation.

Several observable can be monitored for every configuration during the Monte Carlo evolution of the system: the energy, the maximum height among all the chain, the mean of the position of the last vertex of the chains and the mean patch height. The latter variable describes the average height of all the chains in the patch. The mean patch height h can be written as

$$h = \frac{\sum_{I=1}^{N} \max\{r_{z,i}\}_I}{N} \tag{3.11}$$

where $r_{z,i}$ is he value of the distance from the surface of the i-th point along the chain. The autocorrelation time (expressed in number of Monte Carlo Steps) of all these variables is evaluated on the sequence of configurations obtained by the Monte Carlo evolution. On a sequence of t Monte Carlo steps it is defined as

$$C(\Delta\tau) = \frac{\langle (X_\tau - \langle X_\tau \rangle)(X_{\tau+\Delta\tau} - \langle X_\tau \rangle) \rangle}{C(0)} \tag{3.12}$$

where X_τ is the generic observable measured on the configuration at timestep τ, $\langle ... \rangle$ is the mean on $t - \Delta\tau$ elements of the trajectory. Among the observables, the autocorrelation time of h was smaller than the others monitored variables and it has been used as minimal time lag to sample the configurations along the timeseries of the Monte Carlo evolution. In the next session all of the details of the simulations performed with the model are presented.

3.10 Simulations details

In order to keep the computational expenditure to a manageable size periodic boundary conditions are introduced to mimic the behavior of an extended sample. For this purpose only a unit cell of the lattice comprising N chains (where N=mxm with m between 4 and 6) is considered in the simulation. The periodic boundary conditions are ensured by adding copies of unit cell around the simulation tile. Figure 3.8 shows a cartoon representing a patch of DNA+linker constructs arranged in 3x3 patch on a hexagonal lattice. The effect of the periodic boundary condition is also included by representing the replicas that surround the simulation tile.

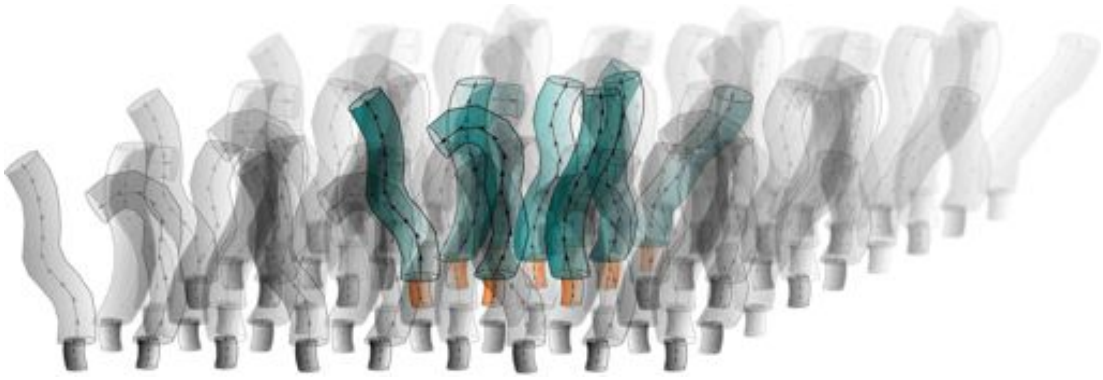

Figure 3.8: Cartoon representing a 3x3 patch of DNA+linker constructs. The effect of the thickness is included. In orange the excluded volume due the spacer and in light blue the DNA steric hindrance. In grey are rendered the replica of the patch that ensure periodic boundary condition. Notice that only 10 bonds for every DNA chain are depicted in the picture for sake of simplicity

Two parameters are set for every simulation: the surface density and the applied force per chain The range of considered surface densities has been selected by looking at which are the order-of-magnitude estimates expected for DNA NAM. A guess is provided by the maximum surface density reported for dsDNA and ssDNA SAMs [39], which are of about 3×10^{12} and 12×10^{12} molecules per cm^2, respectively. This density corresponds to hexagonal lattice spacing, a, equal to 6.2 nm for dsDNA and 3.1 nm for ssDNA, respectively. In order to cover a fairly wide range of observation around the above measured values, the simulations are performed for values of a ranging from 3.4 nm to 20 nm for the dsDNA and from 1.7 nm to 20 nm for the ssDNA. For every simulation the applied force per chain has been chosen in a range between 0 and 60 pN. This maximum value has been chosen considering the fact that such force per chain can lead to conformational changes of the DNA [16].

For each considered value of the hexagonal lattice spacing and applied compressive force, the Monte Carlo simulations were started from the configurations with all the DNA strands in the upright position. At least 50,000 configurations for each simulation are picked at time intervals greater than the autocorrelation time of the mean sample height. For the ssDNA patch 58 simulations have been run, varying surface density and applied force. In the case of dsDNA, 48 simulation have been performed.

3.11 Results

First the results for the patch without applied force are presented. Figure 3.9 depicts the results in the case of a patch of dsDNA at zero force at different surface densities. The black crosses correspond to the results of a system not including the surface attraction potential. The mean patch height is about 7.3 nm at the lowest concentration and slowly increases at higher surface density. This effect can be intuitively explained considering that in a denser patches, the steric hindrance of neighboring chains provides a support to stand up and the mean patch height increases.

Results from ssDNA simulations are discussed below. In this case too, the mean patch height increases with the surface density. Figure 3.10 shows with black crosses the behavior of the mean patch height at different surface densities. At the lowest surface densities, the mean patch height is about 4.3 nm and grows approximately linearly with the surface densities.

The maximum close packing for dsDNA chains is also shown in the graph with an orange dashed line. This maximum possible packing is reached when the interaxial distance is equal to the effective thickness of the chains. At that surface density, the dsDNA constructs can only stay in straight conformation perpendicular to the surface, so the maximum height for the patch is reached (9.32 nm).

Here we present the effect of the attractive surface. In this case the values of the mean patch height of the dsDNA patch are reported in Figure 3.9 with the red crosses. Adding the interaction with the surface lowers the values of the mean patch height. The effect is prominent at low surface densities (below $5\text{x}10^{12}$ molecules cm^{-2}) but at higher surface densities the effect of the attractive surface is negligible. The dsDNA chains are forced to stand in a configuration almost perpendicular to the surface as shown in the snapshot of dsDNA patches taken at the equilibrium (Figure 3.11) .

The effect of the attractive surface (red crosses in the graph of Figure 3.10) is lower at hight densities than at low densities. At surface densities larger than $3.5\text{x}10^{13}$ molecule cm^{-2} the behavior is identical for both the data with and without the effect of the attractive surface. The mean patch height increases less steeply than in the case of the dsDNA. By looking at snapshots of the equilibrium conformations (Figure 3.12) it appears plausible that ssDNA has more space and can assume more configurations thanks to smaller thickness and high flexibility with respect to dsDNA.

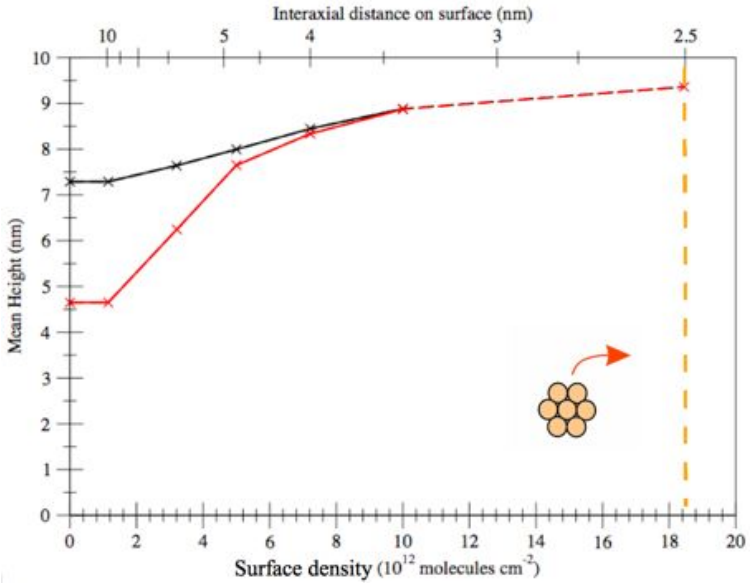

Figure 3.9: Surface densities *vs* mean patch height : simulation for dsDNA patch. Cross mark the results of the simulations at zero force with (red cross) and without (black cross) the $H^{attract}$ describing the attraction to the surface. Lines are drawn to guide the eye. Orange dashed line marks the maximum surface density that the system can reach (close packing).

Figures 3.13 and 3.14 represent the results of simulations at different values of the external force per chain, and for different surface densities. By increasing the force per chain, a systematic decrease at all surface densities, both for ssDNA and dsDNA, is observed. In both cases the behavior presents an almost linear regime at low force per chain. Increasing the force, a zone is reached where the mean patch height tends to a constant value.

From the snapshots at equilibrium, the different behavior for dsDNA and ssDNA can be described. Up to the region in which the steric hindrance of the other chains doesn't play a major role, the dsDNA constructs can be easily bent at the alkyl spacer (see Figure 3.15a). Otherwise, when the surface density is incremented, the mean patch height increases more rapidly at high forces than at low forces. Conversely, ssDNA can bend and can be easily compressed by applying a force. Compared to the dsDNA, at low forces the linear decrease is moderate. At high force ($>$ 30 pN per chain), the asymptotic mean patch height raises when surface density is increased. An interesting point arises from the comparison between the results obtained for ssDNA

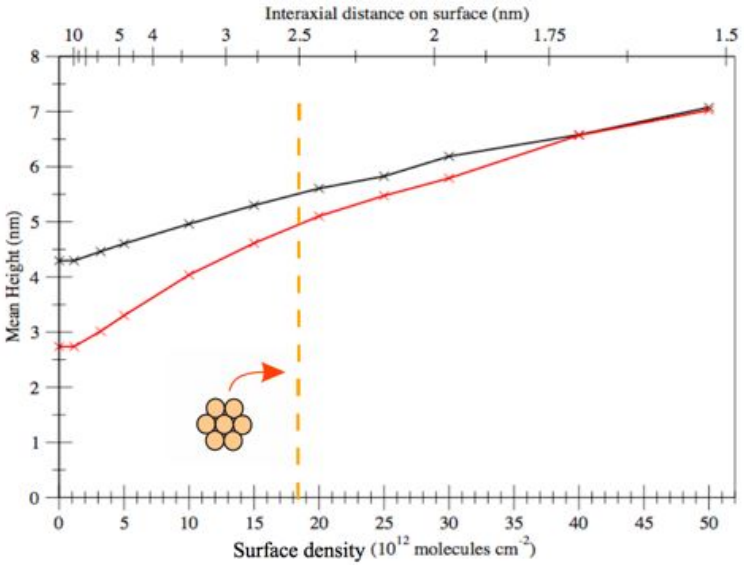

Figure 3.10: Surface densities *vs* mean patch height : simulation for ssDNA patch. Cross mark the results of the simulations at zero force with (red cross) and without (black cross) the $H^{attract}$ describing the attraction to the surface. Lines are drawn to guide the eye. Orange dashed line marks the maximum surface density that the system can reach (close packing) in the case of a dsDNA patch.

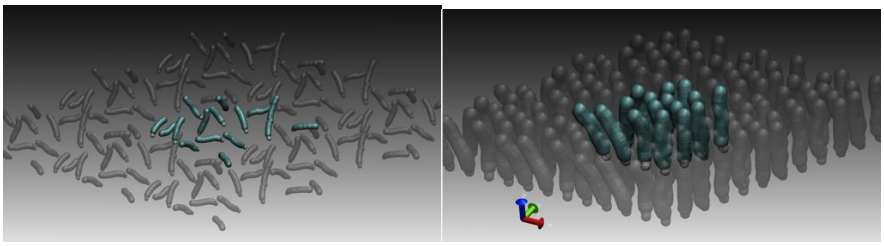

(a) $a = 10nm$ **(b)** $a = 3.4nm$

Figure 3.11: Snapshots rendering equilibrium configuration of dsDNA patch in absence of applied force at different hexagonal spacing distance a (and surface density σ) (a) a=10 nm ($\sigma = 10^{12}$ molecules cm^{-2})(b) a=3.4 nm ($\sigma = 10^{13}$ molecules cm^{-2})

and dsDNA. As pointed out before, at low surface densities the linear behavior of the dsDNA patch seems to decrease more rapidly than in the ssDNA patch. The dsDNA constructs at low force, can stand, but increasing the force applied per chain, they take on a configuration with a bend at the alkyl spacer (see Figure 3.15a). In this way the molecule can be lowered and reach the surface. By contrast ssDNA shows a behavior

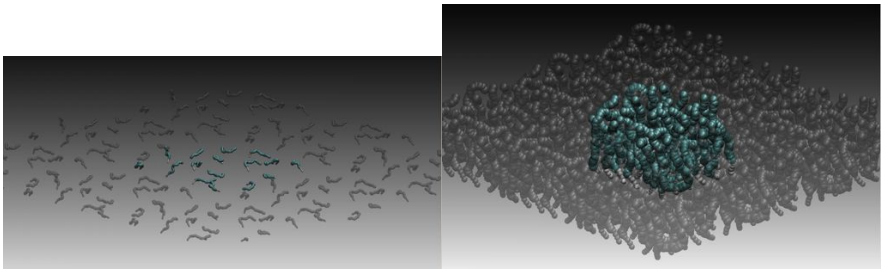

(a) a=10 nm **(b)** a=1.7 nm

Figure 3.12: Snapshots rendering equilibrium configuration of ssDNA patch in absence of applied force at different hexagonal spacing distance a (and surface density σ) (a) a=10 nm ($\sigma = 10^{12}$ molecules cm^{-2})(b) a=1.7 nm (σ=3.9x10^{13} molecules cm^{-2})

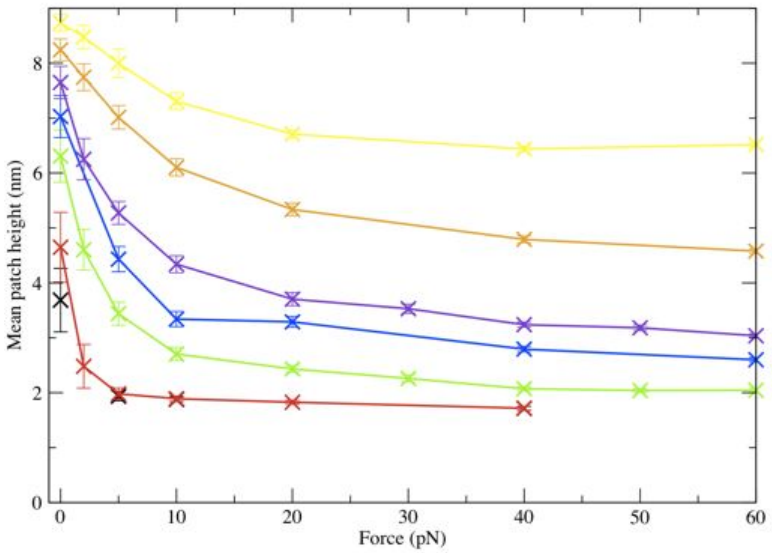

Figure 3.13: Mean patch height *vs* applied force per chain for dsDNA patch. Black crosses illustrate results of the simulations at hexagonal spacing distance a (surface density σ) a=20 nm (σ=0.3x10^{12} molecules cm^{-2}), red cross a=10 nm (σ=1.16x10^{12} molecules cm^{-2}), green cross a=6 nm (σ=3.2x10^{12} molecules cm^{-2}), blue cross a=5.37 nm (σ=4x10^{12} molecules cm^{-2}), violet crosses a= nm (σ=5x10^{12} molecules cm^{-2}), orange crosses a=4 nm (σ=7.22x10^{12} molecules cm^{-2}), yellow crosses a=3.4 nm (σ=10^{13} molecules cm^{-2}). The lines are drawn to guide the eye.

that depends on the high flexibility of the chain: the chains bend at several points and can be easily lowered to the surface. This mechanism doesn't seem to be much affected by the increase in surface densities.

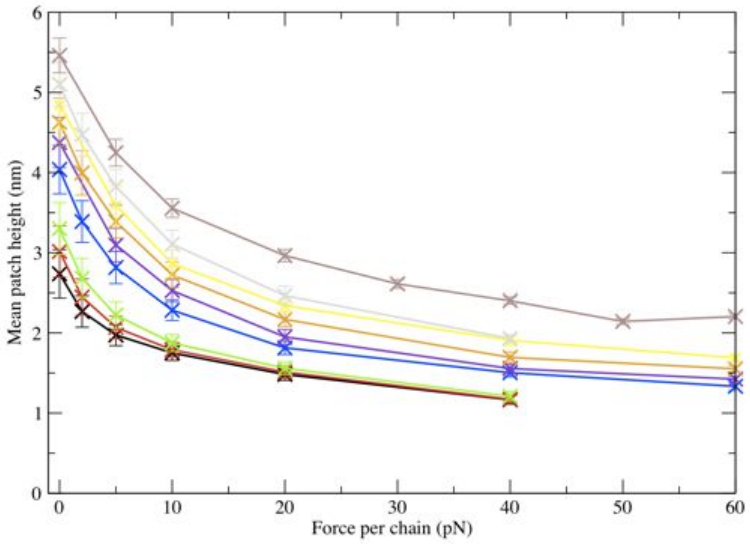

Figure 3.14: Mean patch height *vs* applied force per chain for ssDNA patch. Black crosses illustrate results of the simulations at hexagonal spacing distance a (surface density σ) a=10 nm (σ=1.16x10^{12} molecules cm^{-2}), red cross a=6 nm (σ=3.2x10^{12} molecules cm^{-2}), green cross a=4.8 nm (σ=5x10^{12} molecules cm^{-2}), blue cross a=3.4 nm (σ=10^{13} molecules cm^{-2}), violet crosses a=3.04 nm (σ=1.25x10^{13} molecules cm^{-2}), orange crosses a=2.77 nm (σ=1.5x10^{13} molecules cm^{-2}), yellow crosses a=2.57 nm (σ=1.75x10^{13} molecules cm^{-2}), gray crosses a=2.4 nm (σ=2x10^{13} molecules cm^{-2}) and brown crosses a=2.15 nm (σ=2.5x10^{13} molecules cm^{-2}). The lines are drawn to guide the eye.

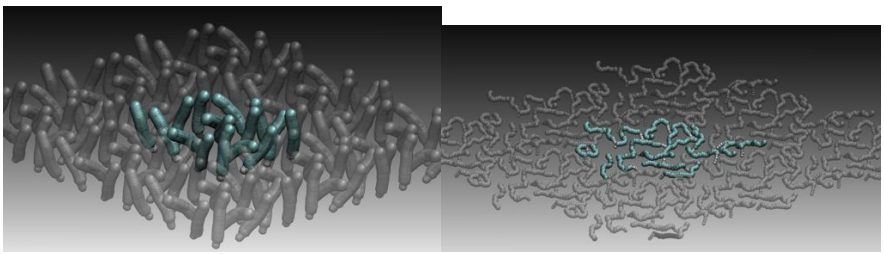

(a) dsDNA a=5.37nm f_{ext} = 20 pN **(b)** ssDNA a=6nm f_{ext} = 30 pN

Figure 3.15: Snapshots rendering equilibrium configuration of ssDNA patch in presence of applied force f_{ext} at different hexagonal spacing distance a (and surface density σ) (a) a=5.37 nm (4x10^{12} molecules cm^{-2}) and force applied equal to f_{ext} = 20 pN (b) a=6 nm (3.2x10^{12} molecules cm^{-2}) and f_{ext} = 30 pN

3.12 Modeling the AFM tip compression

In order to use the result of the DNA patch model presented in the previous sections we fitted the data obtained from the simulation with a continuous function. From the extensively-sampled configurations of model DNA patches the mean patch height h (i.e. the mean height of all the highest point of each chain in the patch) has been fitted as a function of the applied force and the surface density, σ. In this way, all the data of the simulations can be summarized by the surfaces represented in Figure 3.16. Throughout the explored range of force and density values, the value of h for both ssDNA and dsDNA are well interpolated by the following empirical formula:

$$h = a_0 + \frac{a_1}{(a_2 + f_{ext})^2} \tag{3.13}$$

where f_{ext} is the applied force per chain. The parameters, a_0, a_1 and a_2, depend on surface density σ through the following (again empirical) relationships :

$$a_0 = a_{00} + a_{01}\sigma; \tag{3.14}$$

$$a_1 = a_{10} + a_{11}\sigma^2; \tag{3.15}$$

$$a_2 = a_{20} + a_{21}\sigma^2; \tag{3.16}$$

The numerical coefficients a_{00}, a_{01}, a_{10}, a_{11}, a_{20} and a_{21} are provided in Table 3.1. Figure 3.16 illustrates the fitted manifolds of mean patch height h for ssDNA and dsDNA NAMs versus σ and f_{ext}.

Table 3.1: Values of the coefficients

	a_{00}	a_{01}	a_{10}	a_{11}	a_{20}	a_{21}
ssDNA	0.940	0.045	263	0.997	11.0	0.005
dsDNA	0.658	0.544	75.9	6.87	4.36	0.111

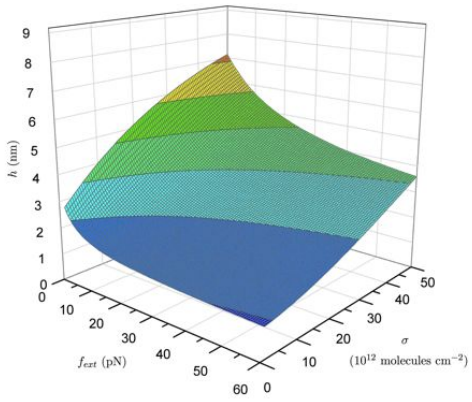

(a) ssDNA

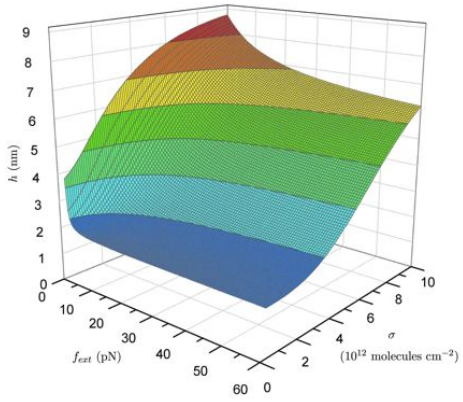

(b) dsDNA

Figure 3.16: Representation of the manifolds of mean patch height *vs* surface density and force per chain obtained by the fitting of simulation results for ss (a) and ds DNA (b)

3.13 Paraboloid model of the AFM tip

For the purpose of comparing the numerical results of Figure 3.16 to experimental measurements, it should be considered how the AFM tip compress DNA patches. The total load experienced by the AFM tip spreads over an area that depends on the tip geometry. The knowledge of the shape of the tip used in the experiments is clearly fundamental for modeling the response of the patch upon compression.

A choice commonly adopted in literature [91, 92, 93, 94] is to model the AFM tip surface as a paraboloid. With this choice, the most important parameter that characterizes the paraboloid, is the apical radius of curvature, α.

In cylindrical coordinates, the surface of the tip modeled as a paraboloid can be expressed as

$$z = h_{tip} + \frac{R^2}{2\alpha} \tag{3.17}$$

where z is the height from gold surface, h_{tip} the height of the tip apex and R is the distance from the axis of the paraboloid. α is the radius of curvature of the paraboloid.

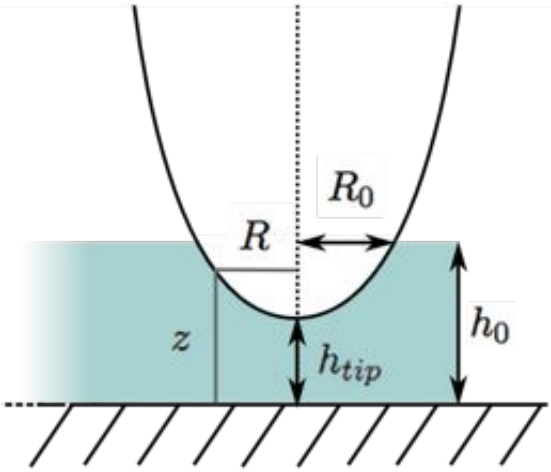

Figure 3.17: Schematic representation of the paraboloid that mimic the AFM tip penetrating in the DNA patch.

With respect to Figure 3.17, we indicate with h_0 the mean patch height at zero force,

$$h_0 = a_0 + \frac{a1}{{a_2}^2}. \tag{3.18}$$

The penetration depth of the tip is therefore given by $(h_0 - h_{tip})$.

The total load applied to the penetrated tip can be evaluated with a continuum approximation. Using cylindrical symmetry, we integrate the force contributions of the infinitesimal annuli corresponding to sections of the paraboloid tip at varying height, z, from the gold surface. For every element of the tip surface, the contribution to the applied load arises both from forces normal (compression of the patch) and parallel to the surface. For the sake of simplicity, only the contributions normal to surface are considered.

The load of one annulus is equal to the product of the annulus surface area, $2\pi RdR$, times the force per unit area of a patch compressed down to height z, that is $\sigma f_{ext}(z)$. The total applied load that the tip experiences can therefore be written as

$$F_{tip} = \int_0^{R_0} 2\pi\sigma R f_{ext}(z)\, dR \tag{3.19}$$

where R_0 is the radius of the paraboloid annulus at $z = h_0$.

Using relations Eq. 3.13 and Eq. 3.17 the integral can be evaluated exactly to obtain:

$$F_{tip} = \pi\alpha\sigma \left(\frac{2a_1 \left(a_0 - h_{tip} + \sqrt{(h_{tip} - a_0)(h_0 - a_0)}\right)}{\sqrt{a_1(h_{tip} - a_0)}} + a_2 \left(h_{tip} - h_0\right) \right) \tag{3.20}$$

Notice that Eq. 3.20 requires that $h_{tip} > a_0$. The physical interpretation of this constraint is straightforward because a_0 correspond to the average height of a patch that is uniformly compressed by an "infinite" force (see Eq. 3.13); consequently the threshold value of the force, F_{max}, beyond which the compressed patch height is a_0 is given by:

$$F_{max} = \pi\alpha\sigma \left(2\left(\sqrt{a_1(h_0 - a_0)}\right) + a_2 \left(a_0 - h_0\right) \right) \tag{3.21}$$

as can be easily checked form Eq. 3.20.

3.14 Summary and conclusions

In this chapter we introduced a model for the DNA patches. The main elements of the system are introduced one by one, starting from the model of the thick chain used to describe the ssDNA and dsDNA to the description of the surface. Next, the simulation scheme has been outlined and the details of the simulation have been provided.

From the results of the simulations, the value of the mean patch height under an applied force has been obtained. The behavior of the mean patch height for different surface densities and values of applied force per chain are described for both ssDNA and dsDNA. The shape of the tip has been also taken into account in modeling the mechanical response when a DNA patch is compressed by an AFM tip. We obtained an analytical formula (Eq. 3.20) that, given the surface density and the tip radius of curvature, puts in relation the height measured by the tip and load applied.

4

DNA patches: Experiments and comparison with the model

4.1 Introduction

Here we compare the analytical formula (Eq. 3.20) obtained in the previous chapter with the experimental measurements carried out by the partner group of Senil Lab (lead by Dott. Loredana Casalis) at Elettra Synchrotron Facility in Trieste.

First of all we shall describe nanografting, the innovative technique that allows the production of DNA patches. With this technique the experimental group of Senil Lab has produced different DNA patches (both of ssDNA and dsDNA) at different surface densities. On these samples, the compression experiments [9] are carried out. In a compression experiment, the DNA patches are imaged with an Atomic Force Microscope (AFM) at different applied loads.

The principal objective of this comparison is to characterize the surface density by comparing AFM height measurements with the computational model. In fact this quantity is very difficult to measure due to the small size of the patch and the small amount of DNA grafted on the surface. As a validation, the model is tested on a DNA monolayer for which the surface density is known.

4.2 Nanografting DNA patches

The technique used to produce DNA patches in Senil Lab is nanografting, which was reported for the first time by Liu and coworkers [95, 96, 97]. It is an AFM based tech-

nique which exploits the surface chemistry of covalent adsorption in order to selectively attach specific molecules in nanodimensional spots. The absorption of thiols on gold surface is one of the most used techniques to covalently attach molecular layers on surfaces. When thiolated molecules are put in contact with a gold surface, the chemical affinity leads to the production of self assembled monolayers SAM [96]. The selective binding of the thiol functional group to gold surfaces have been successfully exploited to graft and orient molecules on surfaces [95].

Nanografting is an improvement of this unconstrained attachment of molecules to surfaces. It gives the possibility, thanks to an AFM tip, to produce also spots or lines whose geometrical parameters (width and separation) are controlled by the size of the tip.

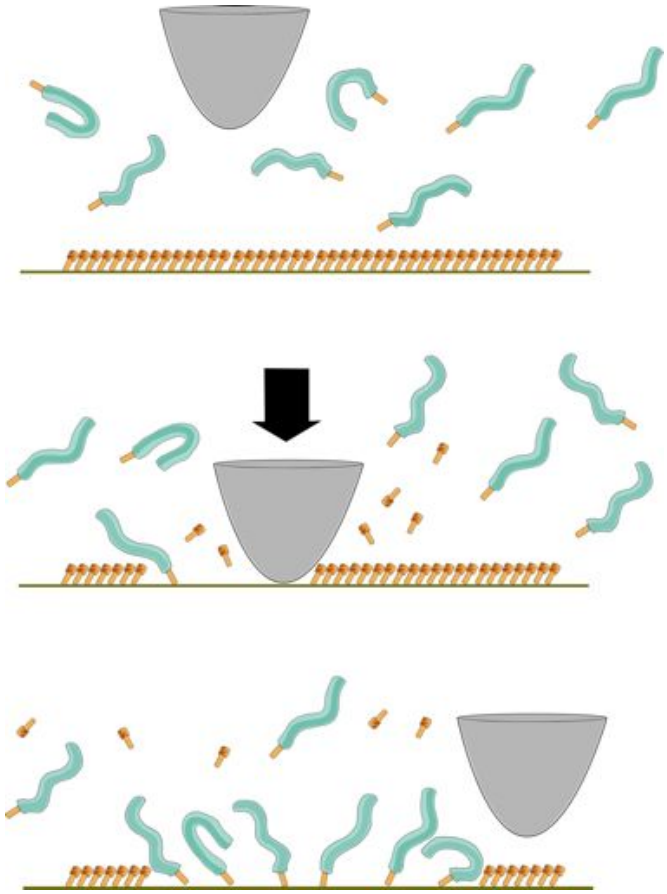

Figure 4.1: Scheme of the process of nanografting

The procedure of nanografting is straightforwardly described. The starting point

is a SAM of alkenethiols that is imaged (using a small force) with an AFM in a liquid environment. The medium contains a thiol-functionalized molecule that has to be grafted to the gold surface (in our case thiolated DNA). By scanning at increased loading force (typically in the order of magnitude of 50-100 nN), the tip "shaves" the alkanethiol monolyer and catalyses the substitution of the existing monolayer. These two steps occurs simultaneously while the tip scans the surface. The self assembly of the new molecules is thus favored in the area spanned by the tip. In this way a Nanografting Assembled Monolayer (NAM) is produced (See figure 4.1). It is thought that the spatial confinement, caused by the passage of the AFM tip, increases the probability of the molecules to adhere to the gold surface with the thiol functional group. In this way a nanografted monolayer is expected to achieve a surface density higher than a SAM. Also, it has been shown that the order and packing of the NAM patches is higher than in SAM patches produced by unconstrained adsorption.

There are two basic parameters that are used to characterize the nanografting process: the nanografting solution concentration and the fabrication parameter S/A. Clearly, increasing the concentration of the solution containing the molecules that have to be grafted facilitates the attachment of the molecules to the surface and hence it increases the surface density. S/A is defined as the amount of overlapping of the tip strokes during nanografting [36]. The more times the tip passes over the same area, the more effective is the substitution of the original molecules with the molecules from the solution (see figure 4.2)

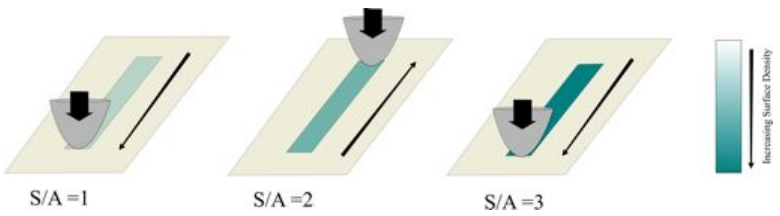

Figure 4.2: Scheme of the effect of fabrication parameter S/A. The more times the tip scans the area, the more effective is the deposition of molecules that are present in the grafting solution (Redrawn from [36])

4.3 DNA NAMs: applications

Once a monolayer of ssDNA is grafted onto a surface, it can bind complementary DNA strands. The unique biomolecular recognition properties of DNA based on Watson Crick base-pairing can be exploited in developing a broad class of biosensors [98]. The idea is to tether proteins or enzymes to the complementary DNA strands in order to have them attaching to the grafted layer. Promising applications of these techniques range from immunological nano-assays [99] to the addressing of multi-enzymatic catalytic reactions [100]. In all these DNA-based devices, it is fundamental to optimize, at each step of the biosensor development, the surface density of the DNA molecules attached to the surface and, to a lesser extent, the physiological conditions (i.e ionic strength of the working solution; screening of surface charges), in order to achieve the highest sensitivity in detecting occurred hybridization.

The group at Senil Lab has pushed forward this technique producing several devices based on the selective and oriented deposition of biomolecules. Moreover, the experimental group of Dr. Loredana Casalis developed the aforementioned strategy giving a qualitative estimation of the surface density of DNA NAMs and hybridization efficiency. By imaging DNA patches with the AFM at different values of load applied to the tip, it is possible to detect hybridization. Such experiments have been recently surveyed by Mirmomtaz et al. [9]. Here DNA patches have been investigated in detail as a function of the key fabrication parameters: the S/A number and the concentration of DNA and counterions in solution.

The general phenomenological aspects found by this investigation are the following. First, a higher S/A leads to higher patches. This can be reasonably explained by considering that a higher S/A increases the number of chains that can be attached to the gold surface. By increasing the surface density, the steric hindrance of the neighboring chains provides a support to stand up.

Second, a higher concentration of the grafting solution increases the surface density. This is detected by measuring an increment of the height patch measured with AFM [9]. It has been shown that at high surface density the response in compression is very different for patches of ssDNA and dsDNA. Moreover, after hybridization with the complementary sequence, the patches show a behavior that is similar to the patches of

dsDNA suggesting that the hybridization can be detected by means of a mechanical probing with an AFM tip.

4.4 Design of the experiments and imaging of NAMs

As pointed out previously, an estimate of surface density can be given making a comparison with the model described in previous chapter.

In the framework of the collaboration with the experimental group of Dr. Loredana Casalis, several experiments on NAM have been produced in order to have some data that can be profitably compared to get an estimate to surface density.

However, to validate the approach, measurement on SAM were produced because their surface density can be well controlled *a priori*. As outlined before, knowing the surface density is an important piece of information, that is essential in developing biosensors but nowadays the surface density has been measured only for SAM.

Successively we chose to produce NAMs at two different surface densities. The surface density was modulated empirically by varying the grafting solution concentration. We decided to use very low concentration (about 1 μM of thiolated DNA) in order to have low surface density according with the choices described in the model. Indeed in the model DNA is described only by means the excluded volume effect and bending rigidity, avoiding the electrostatics. Moreover at very high densities the hybridization with the complementary probes is difficult for steric hindrance, so low density patches are preferred.

Dr. F. Bano, a former colleague of SISSA that worked at Senil Lab nanografted several patches using a grafting solution of 1 and 2 μM of thiolated DNA and imaged with the AFM the NAMs at different applied load. In particular patches of ssDNA, dsDNA have been produced. Succesively it has been measured also the effect of the hybridization *in situ*, namely the direct hybridization of the ssDNA strands after the grafting. Throughout all the experiments a solution with high salt concentration (1 M NaCl) has been used during imaging. It must be stressed that the tips that are used for nanografting deposition, are not used also for the imaging of the patched, for which a new tip is used. In figure Figure 4.3 are reported the AFM topographic images of the NAM patches carried out with a minimal applied load (0.025 nN).

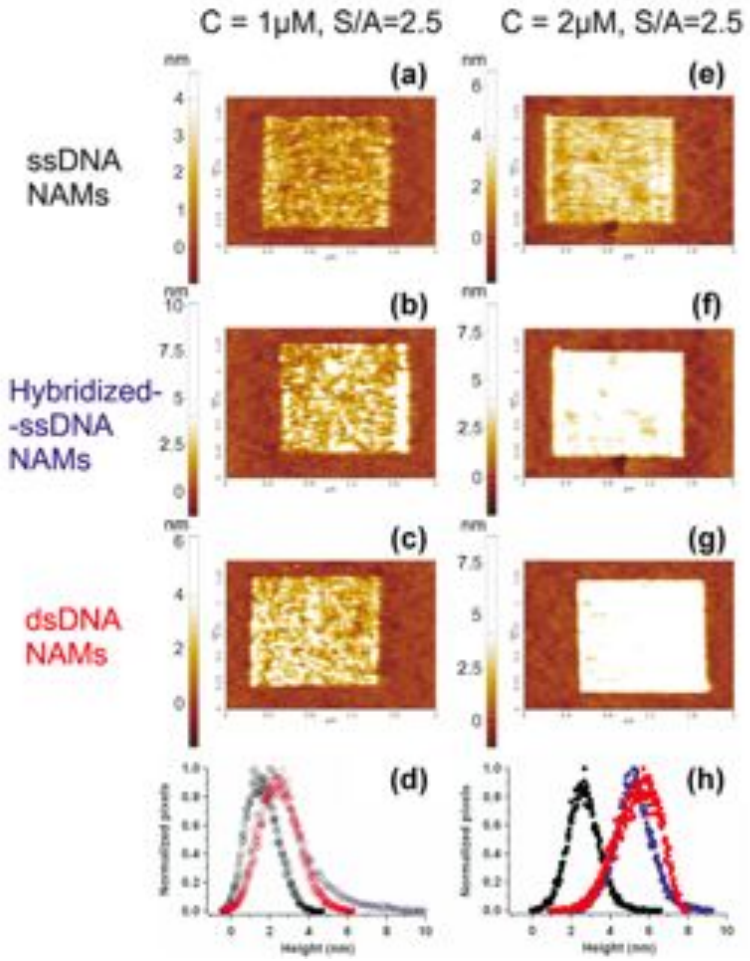

Figure 4.3: AFM topographic images of 24 nucleotides/basepairs long ssDNA (a, e), hybridized ssDNA (b, f) and dsDNA (c, g) NAMs that were grafted within a monolayer of OEG-terminated alkylthiols on gold films. Relative height histograms respect TOEG monolayer correspond to NAMs grafted at 1μM (d) and 2μM (h) DNA grafting solution concentration (black circles correspond to ssDNA, red circles to dsDNA and blue circles to hybridized ssDNA).

In panel (a) of Figure 4.3 it is shown a 1μm x 1μm patch fabricated at DNA concentration of 1μM and S/A = 2.5. The corresponding height histogram (Figure 4.3d, black open circles) revealed a relative height of about 1.8 $\pm$ 0.3 nm with respect to the surrounding carpet of TOEG3 molecules. The absolute height of the DNA from the gold surface can be obtained by adding the height of the TOEG3 carpet (1.8 $\pm$ 0.1 nm see Appendix) to the relative height measured by AFM, resulting in 3.6

± 0.3 nm for the patch shown in Figure 4.3 a. Hereafter it is always reported the absolute heights of DNA from the gold surface. In Figure 4.3 c, a patch of grafted dsDNA is reported showing a patch height is of 4.3 ± 0.3 nm. The associated height histogram is plotted in Figure 4.3 d (red open circles). A ssDNA NAM grafted using the same conditions as the one in Figure 4.3 a, and afterwards hybridized with the fully complementary strand, is shown in Figure 4.3 b. The resulting height histogram (Figure 4.3 d, blue open circles), shows an increase in absolute height from about 3.6 0.3 nm (ssDNA NAM) to about 4.3 ± 0.3 nm, as for the case of dsDNA NAMs. This increment of height respect to ssDNA NAM is an indicator of successful hybridization, because the dsDNA strands are more rigid than ssDNA ones and therefore can stand up. When NAMs are grafted at higher DNA concentration in solution (2 μM), keeping all the other fabrication parameters constant (e.g. S/A=2.5), the height of the patches increases. In fact, the higher is the DNA concentration in solution, the higher is the efficiency of nanografting process and hence an higher surface density of the NAM is expected. This will result in an increase of the height in the dense patch since the steric hindrance of neighboring chains provides an enhanced support to stand up compared to a less dense patch. Figure 4.3 e-g shows NAMs of ssDNA, surface-hybridized ssDNA and solution-hybridized, grafted dsDNA, respectively. The absolute heights calculated from the height histogram (shown in Figure 4.3 h) are 4.7±0.2 nm, 7.3±0.2 nm and 7.0±0.4 nm, respectively.

4.5 AFM imaging of NAMs at different applied load

The height measurements in Figure 4.3 are clearly compatible with the expected higher mechanical rigidity of dsNAMs compared to ssNAMs. The different response in compression of the two types of patches is, however, best characterized by means of AFM height versus applied load measurements. This is carried out by recording AFM topography images (from which differential height profiles are extracted) at different loads applied by the AFM tip. In this way height versus applied load curves are obtained. The absolute heights are plotted in Figure 4.4 as a function of tip load. It must be stressed that the height measurements are averaged over repeated experiments carried out with different DNA patches prepared with the same protocol (see details in Appendix) and AFM tips.

From the qualitative analysis of the data, some general conclusions can be drain. For all patches, the mean height decreases monotonically upon increasing the applied load to the tip. The mechanical response of ssDNA NAMs (black circles) with respect to surface-hybridized ssDNA (blue circles) and dsDNA NAMs (red circles) is different at both grafting concentrations. However there is no significant difference in the behavior of dsDNA and surface-hybridized grafted strands.

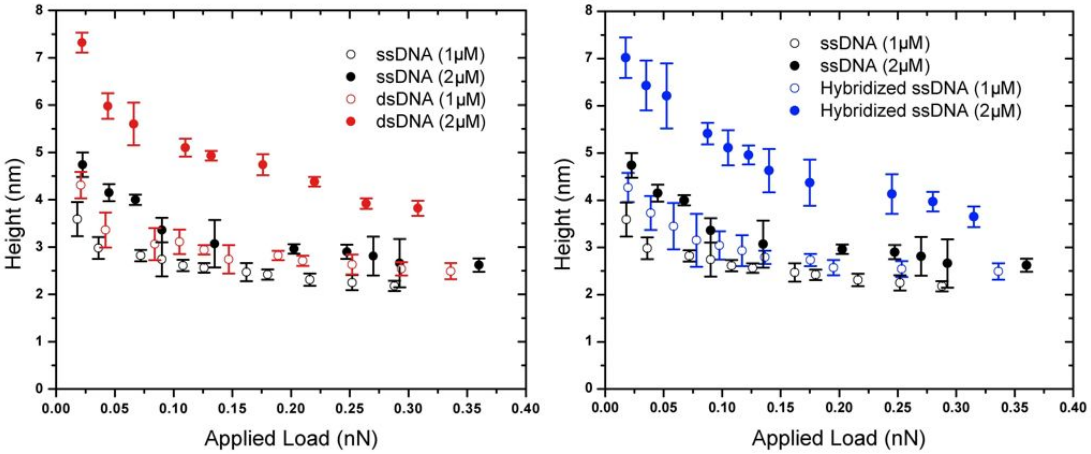

(a) ssDNA and dsDNA **(b)** ssDNA and hybridized ssDNA

Figure 4.4: Absolute heights of DNA NAMs recorded as a function of the applied load by AFM tip. (a) Comparison between ssDNA (in black) and dsDNA (in red) NAMs that were prepared at differen grafting solution concentration (1 and 2 μM respectively open and filled circles) (b) height *vs* applied load curves of hybridized *in situ* ssDNA compared with the same curves of ssDNA NAMs reported in (a)

4.6 Experiments on the tip

In order to employ the analytical formula (Eq. 3.20) for obtaining the surface density of a DNA patch, α, the apical radius of curvature of the tip must be known. An estimate of α could be obtained from the nominal radius of curvature of the manufacturer. However, during AFM experiments, the tip can change its radius of curvature due to wear caused by the patch probing. The reproducibility and the robustness of the experimental measurement of the height of the patch upon compression collected with different tips allows us to assume that, in the course of the experiments, the tip radius of curvature maintains a constant value. Such value can accordingly be measured after a compression experiments.

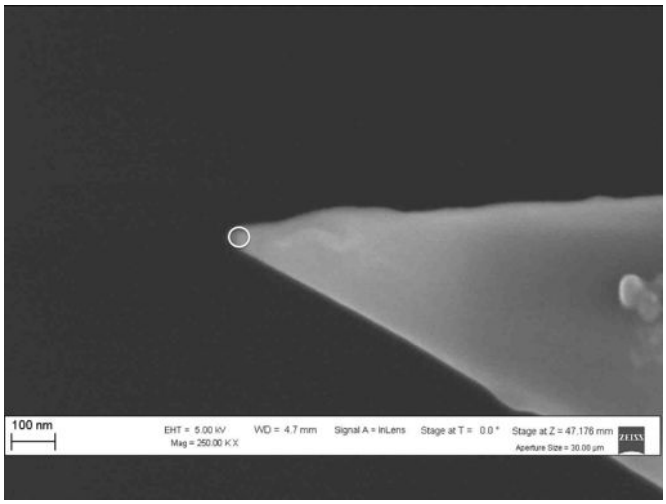

Figure 4.5: Scanning Electron Microscope image of an AFM tip after a compressibility measure of a DNA patch. The tip has a radius of curvature equal to 23 ± 1 nm (white circle)

To address these points, the experimental group of Senil Lab, has characterized with Scanning Electron Microscope a set of 6 AFM tips after being used to compress DNA patches. It was found that the mean radius of curvature at the apical point is equal to α=25 ± 3 nm. The result is striking because the radius of curvature is twice the nominal (10 nm) given by the manufacturer.

Based on the measured value of α, we conclude that accounting for the paraboloid tip geometry is essential in our study because the radius of curvature of the tip is

comparable with the height of the patch and the separation between the chains. Under these conditions, approximating the tip as a flat surface would lead to systematic errors.

4.7 Comparison with experimental data

The experimental data are well fitted by Eq. 3.20 derived from the coarse-grained model after an optimal choice (fit) of the model patch density σ. The fit was carried out using a least squares procedure with the total applied load F_{tip} and h_{tip} taken respectively as the independent and dependent variable. According to this choice, Eq. 3.20 was inverted numerically in the range $a_0 < h_{tip} < h_0$ in order to obtain h_{tip} as function of F_{tip}. The surface density σ is then obtained by numerical minimization of the summed square difference between the experimental and computed heights of the patch at various applied load:

$$\chi^2 = \sum_i \frac{(h_{i,exp} - h_{i,model})^2}{s_i^2} \tag{4.1}$$

where i is running on all the measurement of the patch height, $h_{i,exp}$ and $h_{i,model}$ are respectively the measured experimental height and obtained by the model at given applied load and s_i is the experimental standard deviation on $h_{i,exp}$.

4.8 Comparison with SAM

In order to have a validation to the model, an experiment with a system of known surface density has been performed with a ssDNA SAM. In a ssDNA SAM the surface density can be controlled by monitoring the time of the exposure to the solution of thiolated ssDNA. The longer the contact time, the higher the surface density. In order to measure the topographic profile and to extract the height of the patch, the following strategy has been adopted. By means of nanografting, a patch of TOEG has been grafted within a SAM of ssDNA. In this way, the grafted TOEG provides a reference for measurements of the ssDNA monolayer height. Figure 4.6 illustrate schematically the system and the height histogram from which the mean height is measured. The AFM topographic image of the SAM collected at "zero force" shows a hole in correspondence with the TOEG nanografted area. Different applied loads have been applied to the

SAM and the curves of absolute height *vs* applied load have been obtained as reported in figure 4.7.

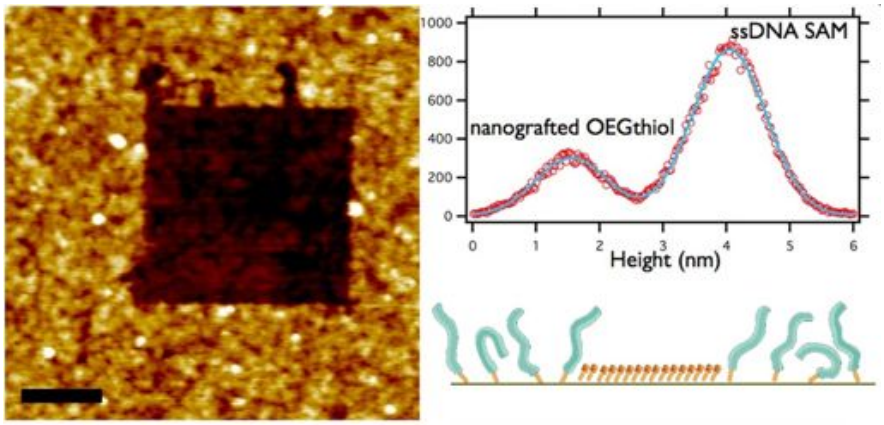

Figure 4.6: AFM micrograph of a TOEG3 patch nanografted into a high density ssDNA SAM with corresponding height histogram and schematics (scale bar=200nm).

Then the comparison between the data and the model has been carried out as described in previous section (see figure 4.7). The surface density returned by the fit procedure was equal to $13 \pm 2.5\text{x}10^{12}$ molecules cm^{-2}, which is in very good agreement with the nominal values measured in such system [39] and hence provides a successful validation of the computational approach.

4.9 Comparison with NAM

From the data presented in Figure 4.4 it has been produced a comparison using the strategy outlined in previous sections. In Figure 4.8 and 4.9, the comparison between experiments and fit are shown and the results are summarized in Table 4.1. The experimental data are well described by the fit in the whole force range in both ssDNA and dsDNA at the two considered concentrations. Also, the value of the reduced χ^2 is in the order of unity, indicating a good fit of the data. It is interesting to notice that the fitted values for the surface densities of the NAM patches are higher compared to those found in the SAM counterparts [39, 46, 101]. Therefore it is plausible that, with NAMs, one could span a wider range of surface densities even beyond the limiting values reported for SAMs, both for ssDNA and dsDNA.

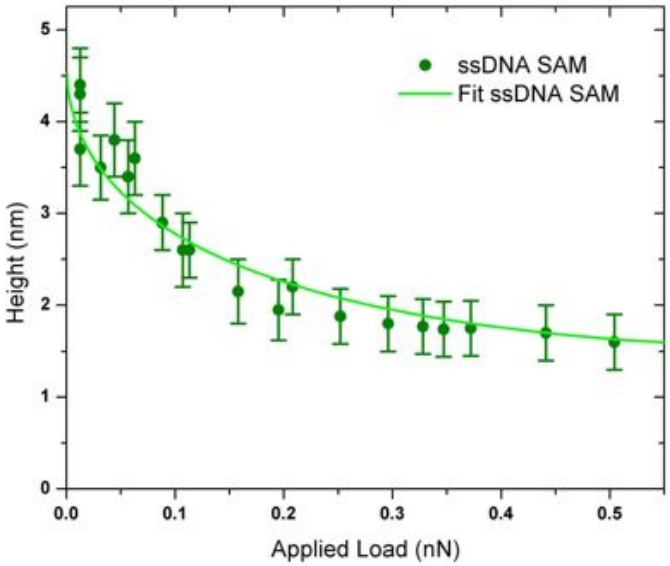

Figure 4.7: Comparison between experimental (symbol) and fitted data (lines) for height vs applied load for a high density ssDNA SAM

Table 4.1: Estimated surface density values for the ssDNA and dsDNA grafted at 1 and 2 μM concentration

NAM	[DNA]=1μM	[DNA]=2μM
ssDNA	13.1± 1.1x10^{12} molecules cm^{-2}	17.7± 1.7x10^{12} molecules cm^{-2}
dsDNA	3.8 ± 0.3x10^{12} molecules cm^{-2}	6.2± 0.3x10^{12} molecules cm^{-2}

4.10 Comparison with Hybridized NAM

Here we show how the modeled mechanical response of ssDNA and dsDNA patches can be used to estimate the hybridization efficiency of ssDNA NAMs. A proper understanding of the hybridization mechanism in such dense systems is obviously crucial for the use of nanografting-based nano-arrays for quantitative assays [102, 103, 104]. It can be argued that, in a partially hybridized patch, the molecules that bear the compression exerted by a mild AFM load are essentially only the hybridized ones. The double stranded nature of these molecules, in fact, causes them to stand out of the background height of the non-hybridized DNA strands. Neglecting the presence of

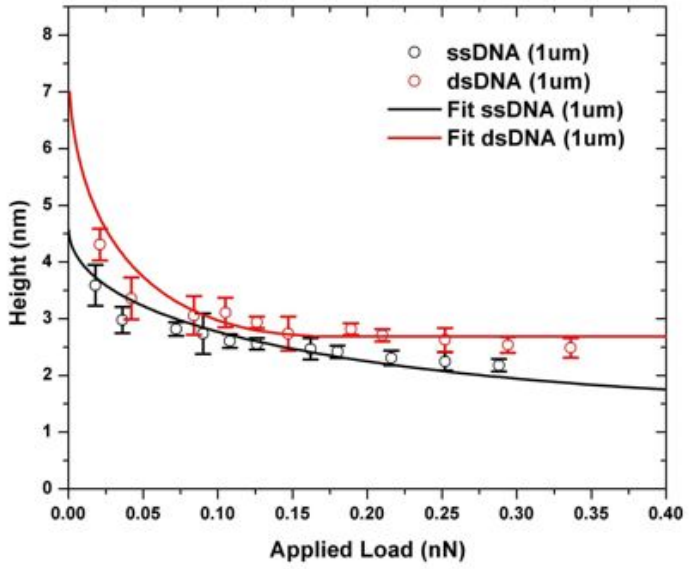

Figure 4.8: Comparison between experimental data (symbols) and the theoretical fits (lines) of patch height vs applied load. Black stands for ssDNA data, while red stands for dsDNA. The heights of the patches nanografted at 1 μM concentrations of ssDNA and dsDNA in solution are represented here.

single-stranded molecules, the density of the hybridized patch can be obtained by fitting the experimental compressibility curve with the one of a pure dsDNA patch (see Figure 4.10). This value clearly overestimates the true density of the double-stranded hybridized molecules because it effectively ascribes to the latter also the contribution to the mechanical resistance due to the ssDNA background. Consequently, the ratio between the effective dsDNA density of the hybridized patch and the non-hybridized one provides an upper bound on the hybridization efficiency.

From the fit of experimental data with the model for the dsDNA one obtains a surface density equal to $3.6 \pm 0.4\text{x}10^{12}$ molecules cm^{-2} in the 1 μM case and equal to $6.1 \pm 0.6\text{x}10^{12}$ molecules cm^{-2} in the 2 μM case. These values lead to an upperbound of about 30% for the hybridization efficiency. This value is lower compared to data present in literature and estimated with other strategy [102, 103, 104] that gives an efficiency of about a 50% . However this bound is well above the 10% value found from data obtained with spectroscopic techniques for saturated DNA SAMs [39]. While it

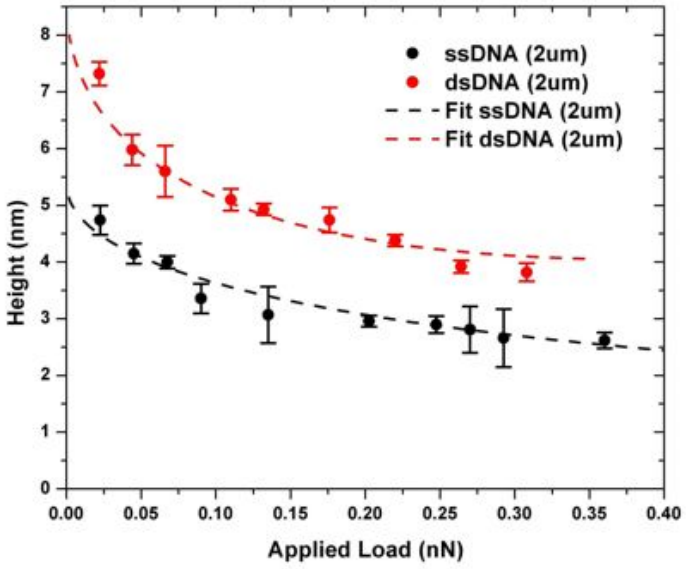

Figure 4.9: Comparison between experimental data (symbols) and the theoretical fits (lines) of patch height vs applied load. Black stands for ssDNA data, while red stands for dsDNA. The heights of the patches nanografted at 2 μM concentrations of ssDNA and dsDNA in solution are represented here.

must be stressed that the value refers to an upper bound and hence all lower values could be compatible with the result, the significant difference of the NAM value with the SAM one is consistent with the expected higher order of NAM monolayers.

4.11 Summary and conclusions

In this chapter we have reported on the use of an integrated experimental/theoretical approach to provide a phenomenological, quantitative description and prediction of the response to mechanical compression of ssDNA and dsDNA patches with varying levels of surface density. The comparison with the analytical formula obtained from the theoretical/computational model has provided an estimate of the surface densities for both SAM and NAM of DNA from their AFM topographic images at different applied load. Therefore, an upper bound to hybridization efficiency has been obtained by simple reasoning.

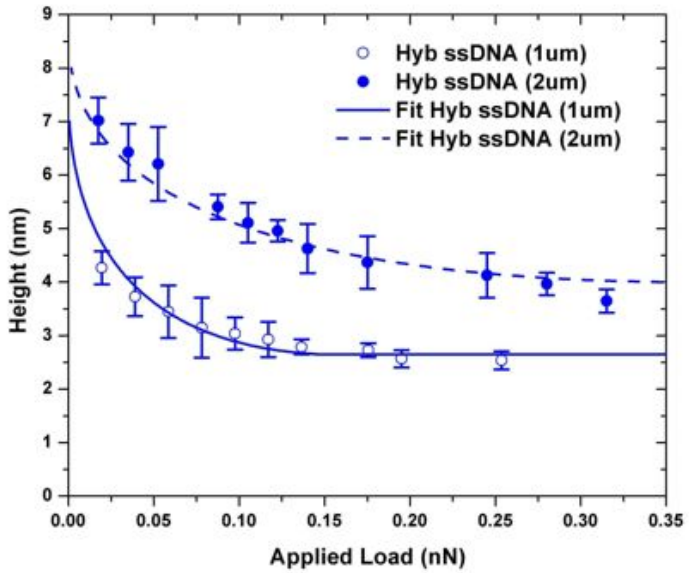

Figure 4.10: Comparison between experimental (symbol) and computational data (lines) for height vs applied load for ssDNA NAM after hybridization.

5

Conclusions

In this thesis we focused on the elastic response of one or few DNA molecules at the nanoscale. In particular, two problems have been addressed using both advanced experimental techniques and computational/theoretical models: the stretching of ssDNA and the compression of DNA patches.

For what concerns stretching of ssDNA, presented in Chapter 2, we used an unprecedented experimental technique to extract elongation curves of long molecules of ssDNA at different salt conditions. Within a collaboration with the Small Biosystem Laboratory led by Prof. Felix Ritort we performed these experiments with OT. From the analysis of the data, the formation of secondary structure at different salt condition has been studied. Moreover, simple theoretical models have been used in order to characterize the elastic response of ssDNA.

We found that the formation of secondary structure is very sensitive to the variation of monovalent and divalent salt and it increases when the concentration of the ions in solution increases. We shown that the force extension curves of ssDNA at a certain divalent salt concentration are almost identical to the one found at a two orders of magnitude smaller concentration of monovalent salt.

The persistence length, extracted from the force-extension curves using the WLC model, shows a dependence on the concentration. The higher the salt concentration, the smaller the persistence length. Furthermore, using the TC model we inferred the effective thickness of the filament of ssDNA in the data at low salt concentration.

In the near future, the work with this new experimental technique can be extended to the study of the elastic response and the secondary structure formation in presence

of other monovalent and divalent cations such as potassium and calcium. Additionally the effect of the concentration of the blocking oligonucleotide solution must be explored in detail. New experiments are planned to systematically check whether the force extension curves are affected by a different concentration of oligo solution and how much specific is the binding of the oligo to the ssDNA. Another interesting perspective could arise from the study the effect of the macromolecular crowding on the elastic response of the ssDNA and hence in the formation of secondary structures. Moreover, this technique could be profitably used in future for the study of the interactions of ssDNA with proteins or chemical for the development of new drugs opening many avenues of investigation.

For what concerns the compression of DNA patches (Chapters 3 and 4), we focused on the development of a computational model for the simulations of DNA patches. This model has been profitably used for the description of the behavior of a DNA patch sensed and compressed by an AFM tip.

With the model it is possible to obtain the height of the DNA patch of both ssDNA and dsDNA at a given surface density and applied force. This relationship can be fruitfully exploited to estimate the surface density from AFM topographic images of DNA patches at different applied loads. Surface density is quantity that is fundamental for the fabrication and characterization of a nanodevice but it is difficult to measure with typical experimental set-ups,.

Within the collaboration with the Senil Lab headed by Dr. Loredana Casalis, our model for the DNA patches has been compared with experimental data. This group produced the DNA patches using nanografting, an innovative technique for the AFM tip-aided deposition of DNA, and measured the height from AFM topographic images of the patches at different applied load. First, the model was validated on a self-assembled monolayer of DNA whose surface density was known. Second, this model provided the values of surface densities of the nanografted DNA patches.

We found that the surface densities obtained with the nanografting technique are higher than the one found with different technique for the attachment of DNA on surface. The model can also provide an estimate of the efficiency of hybridization in ssDNA patches. We also found a higher value of hybridization efficiency (30%) for NAM than the one reported in literature for monolayers of DNA.

We expect that these possibilities offered by nanografting of tuning and increasing the surface density of DNA patches could be successfully exploited for building nanodevices for biosensing application.

The model presented in this thesis provides a valuable aid to design special-purpose nano-patches. In fact, the proposed phenomenological model can be used to choose the appropriate patch surface density to ensure that the change in height upon (possibly partial) ssDNA hybridization is easily and unambiguously ascertained by AFM probing. As future work, we could set up simulations of patches consisting of both ssDNA and dsDNA filament in order to get a more precise estimate of the hybridization efficiency via this computational/theoretical approach. The present investigation can be also extended to specific diagnostic directions. In particular, it would be worth covering with this analysis a wider range of lengths of the grafted DNA sequences (18 to 60 nucleotides) that are relevant from the biomedical and nano-technological points of view.

Appendix: Experimental details

A.1 Stretching ssDNA

A.1.1 Synthesis of the hairpins

The hairpins used for the experiment of ssDNA stretching have been synthetized at the Small Biosystem Lab in Barcelona. The hairpin consists of a stem of 6838 bp with a tetraloop at one end and two 29 bp dsDNA handles at the other. The synthesis has been reported previously in literature [61] and the steps are summarized in Figure A.1. N6-methyladenine free λ-DNA (New England Biolabs) is digested with BamHI (New England Biolabs) and phosphorylated at its 5-ends (T4 polynucleotide kinase, New England Bio- labs). The fragment of the dsDNA between positions 41733 and 48502 (the cosR end) is used as the stem of the DNA hairpin.

Several oligonucleotides whose sequence are reported in Table A.1 are used as building blocks for the formation of the hairpin. The tetraloop that close the hairpin is created using BamHI-loopII purchased from Eurons MWG Operon. This oligonucleotide forms a small hairpin structure whose stem has an overhang complementary to the BamHI restriction site (see Figure A.1).

The dsDNA handles are formed from two oligonucletides (cosRlong and cosRshort from Sigma-Aldrich). The partial complementarity of the two oligos allows for the formation a protruding end complementary to the cosR .

The cosRshort is functionalized at the 5-end with a biotin and the cosRlong is tailed with multiple digoxigenins at its 3-end (DIG Oligonucleotide tailing Kit 2nd Generation,Roche). After this procedure, cosRlong is puried with the QIAquick Nucleotide Removal Kit (QIAGEN).

The dsDNA handles are formed by the hybridization of the unpaired regions of cosRlong and cosRshort with a complementary oligonucleotide (splint)

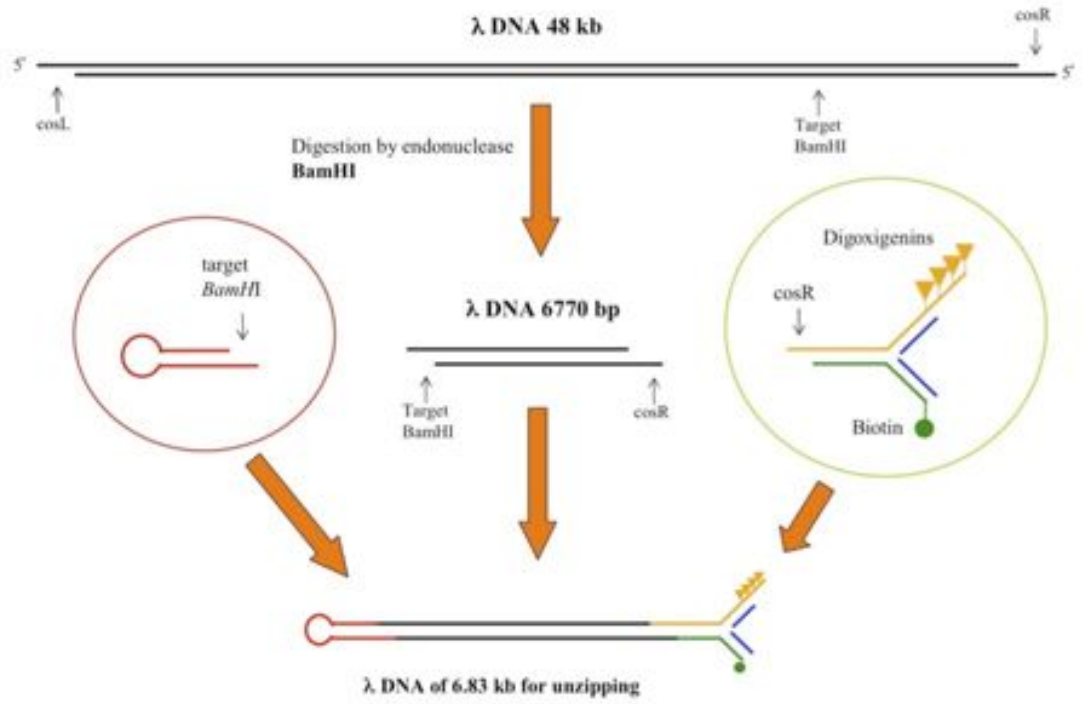

Figure A.1: Scheme illustrating the synthesis of the hairpin. The λ-DNA and the 6770 bp fragment are represented in black, BamHI-loopII in red, cosRlong and cosRshort respectively in yellow and green and split in blue. Reproduced from Supporting Informations of [61].

The self assembly of the hairpin is carried out with a thermal treatment. All the oligonucleotides and the 6770 bp stem are annealed by incubation for 10 minutes at 70° C, followed by incubation for 10 minutes at 55° C and cooling down to room temperature.

The formation of phosphodiester bonds between the oligonucleotides (ligation) is performed as an overnight reaction at 16° C (T4 DNA ligase, New England Biolabs).

The molecules obtained are stored in a solution containing Tris.HCl 10 mM, EDTA 1 mM, and NaCl 10 mM with pH=7.5.

A.1.2 Buffer solutions

The TE buffer solutions with monovalent salt used in the experiments contain Tris.HCl 10 mM and EDTA 1 mM. The NaCl concentrations used used are 10, 25, 50, 100, 250,

Table A.1: Oligonucleotides used for the hairpin synthesis

Oligonucleotide	Sequence
BamHI-loopII	5'-GATCGCCAGTTCGCGTTCGCCAGCATCCG ACTACGGATGCTGGCGAACGCGAACTGGC-3'
cosRlong	5'-Pho-GGGCGGCGACCTAAGATCTATTATATATGTG TCTCTATTAGTTAGTGGTGGAAACACAGTGCCAGCGC-3'
cosRshort	5'-Bio-AGTTAGTGGTGGAAACACAGTGCCAGCG CAATAGAGACACATATATAATAGATCTT-3'
splint	5'-GCGCTGGCACTGTGTTTCCACCACTAACT-3'

500 and 1000 mM. The buffer solutions with divalent salt contain Tris.HCl 10 mM and a concentration of $MgCl_2$ equal to 0.5, 1, 2, 4 and 10 mM. For all the solutions, the pH has been adjusted at 7.5.

A.1.3 The beads

Streptavidin (SA) beads are purchased from G.Kisker-Products for Biotechnology and have a diameter of about 3 μm.

AntiDigoxigenin beads (AD) are synthesized with the protocol of Maumita Mandal. The diameter of the polystyrene beads used (Spherotech) is about 3 μm.

A.1.4 Preparation of the block loop solutions

The sequence of the block-loop oligonucleotides is 5'-TAGTC GGATG CTGGC GAACG CGAAC TGGCG-3'. The block-loop solutions have been prepared using the same buffer solution used for the experiment adding the oligonucleotide up to a concentration of 250 nM. Before doing the experiment this solutions have been annealed at 45° C for 15 minutes in order to avoid the formation of secondary structures.

A.1.5 Optical Tweezers

The Optical Tweezers used consists of two counter-propagating laser that form a single optical trap where particles can be trapped by gradient forces. The setup (Figure A.2) is similar to the one described by Smith et al. [21] and it is described in detail in the literature [22, 61, 105, 106]

The two laser beams have orthogonal polarization so the optical paths are separable using polarized beamsplitters. From now, only one path will be described. The laser beam is focused in the microfluidic chamber by the first objective and is collected by the second one. The position of the trap is controlled by the wiggler that bends the optical fiber. The 5% of the light is deviated by a pellicle to a light lever position sensitive detector that measures the position of the center of the trap.

The laser light is split by a non-polarizing beamsplitter to a position sensitive detector and a photodiode that measure the intensity and the position of the beam. This two detectors can measure the force applied to the bead in the trap by measuring the variation of the light intensity. In figure A.3 there is a schematic representation of the working principle. The photodiode measure the force in the direction in which the lights propagate while the position sensitive detector measure the force components in the plane normal to the beam. At zero force the laser beam collimated by the objective, is projected onto detector surfaces. If an external force push downwards (or upwards) the bead in the trap, the light moves down (or up) on the force PSD while if an axial force push (or pull) the bead in the direction of the laser beam the light spot contracts (or expands) on PD.

The force and the distance are obtained processing and converting the currents measured by the detectors. The calibration procedure is reported in Supporting Information of [61]. With this setup we get an acquisition frequency of 1 kHz. The resolution in force is 0.1 pN and 0.5 nm in distance. The whole instrument is kept in a constant temperature of 25° C and hence all the experiments are carried out at the same temperature.

A.2 Mechanical sensing of DNA patches

A.2.1 Materials and Instrumentation

Chemicals: The thiol-modified DNA (P24; SH$-(CH_2)_6$-5'- TAATC GGCTC ATACT CTGAC TGTA-3') oligomers and non-thiolated complementary strands (T24; 5'-TACAG TCAGA GTATG AGCCG ATTA-3') were purchased from Biomers GmbH (Ulm, Germany) as HPLC purified grade and used without further purification. Sodium chloride (NaCl), Tris(hydroxy-methyl)aminomethane (Tris) and ethylenediaminetetraacetic

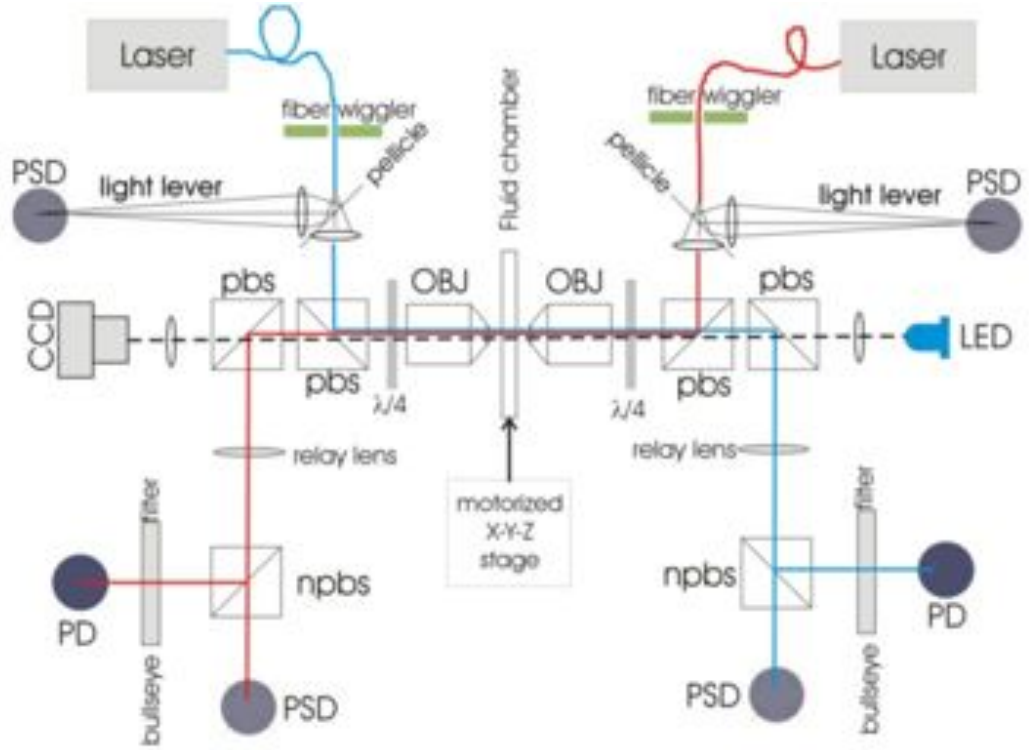

Figure A.2: Scheme illustrating the Optical Tweezers setup. Optics components: Laser = Fiber-coupled diode laser, pbs=polarizing beam-splitter, npbs=non-polarizing hybrid beam-splitter, OBJ = Objectives, PSD = position-sensitive photo detector, PD = photodiode , $\lambda/4$ = quarter-wave plate, CCD = TV camera, LED = Light Emitting Diode. Reproduced from [22].

acid (EDTA) were purchased from Sigma. Top oligo ethylene-glycol3 terminated alkylthiols ($SH(CH_2)_{11}(OCH_2CH_2)_3OH$, TOEG3) was obtained from Prochimia and fresh solution prepared in pure ethanol (Fluka, purity $\leq$ 99.8 %) before the experiments. TE buffer (1M NaCl, 10mM Tris, 1mM EDTA, pH 6.9) was prepared using MilliQ water (resistance $>$ 18MΩcm) and filtered through a Millipore filter (GP Express PLUS Membrane, 0.22 μm pore size) before use.

AFM: All the Atomic Force Microscope (AFM) experiments were performed by contact-mode XE-100 PARK AFM system (Korea) with a custom liquid cell at room temperature. Standard silicon rectangular cantilevers, (NSC19, MikroMasch, 0.63 Nm^{-1}, nominal tip radius $<$ 10nm) and (CSC38/B, MikroMash, 0.03 nm^{-1}, tip radius 10nm) were utilized for nanografting and imaging, respectively, using the contact-mode

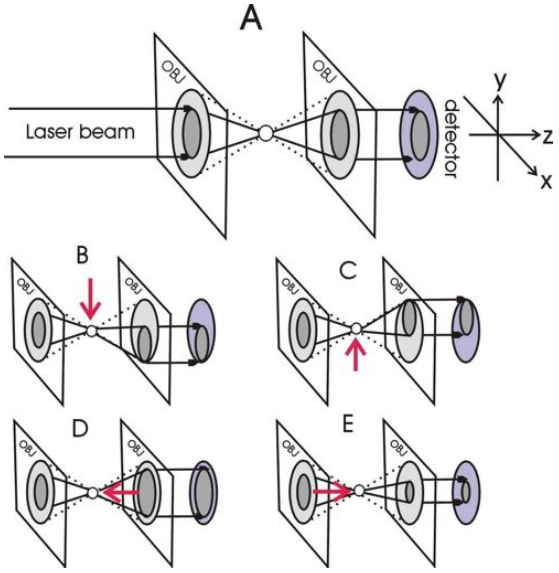

Figure A.3: Schematic representation of the measurement of the force at the PSD and PD (A) Zero force (B-C) Light path to the PSD when an external force is applied in the direction normal to the laser beam. expands on detector. (E) Light path to the PD when an external force is applied in the direction of the laser beam. Reproduced from [22]

AFM.

A.2.2 Production of DNA patches

Monolayer preparation: For preparing a bio-molecule resistant monolayer on ultra flat gold substrate, a 100 nm thick gold film was deposited on freshly cleaved mica sheets (Mica New York Corp., clear ruby muscovite) at a pressure of about 10-5 mbar in an electron-beam evaporator at a rate of 0.1 nm/sec. In this work, Epoxy SU8-100 (negative tone photoresist, MicroChem) was utilized as a solid support. A small drop of SU8-100 was placed over gold slides (few millimeters in size) and then cured to form SU8-100/gold/mica sandwich. The gold-mica interface was disclosed mechanically, and immediately immersed into a freshly prepared 100μM solution of TOEG3 in ethanol for 15 hours at room temperature. The resulting SAM was then rinsed with ethanol and dried under a soft stream of nitrogen.

Preparation of dsDNA: Double-stranded DNA (dsDNA) molecules for nano-grafting duplexes were prepared by incubation of a 1:3/2 solution of ssDNA and its complementary strands in TE buffer at melting temperature for 10 min. After the incubation, the

temperature was allowed to cool down to room temperature and duplexes with final concentrations of 1 μM and 2 μM were obtained.

Nanografting of DNA NAMs and hybridization conditions: The protocol of nanografting has been reported earlier [9, 36]. Briefly, AFM tip scanned the selected area at relatively large forces (usually in the range of 80-100nN) with a scan rate of 500 nm/sec in the presence of thiolated (ss- or ds-) DNA (1 μM (or 2 μM) dissolved in a 1:1 mixture of TE buffer and ethanol) solution. This caused TOEG3 molecules from the surface to be replaced locally with thiolated DNA molecules present in the solution. The fabricating parameter S/A, the ratio between the total area (S) that is coated by the tip during nanografting and the area of the patch (A) is used to control nanografting. All the hybridization reactions were carried out at room temperature within an AFM liquid cell for 1 hour. The substrate was washed thoroughly with TE buffer to expunge loosely bound DNA molecules before and after the hybridization reaction.

A.2.3 AFM height and compressibility measurements

Topographic images of resulted Nanografted Assembled Monolayers (NAMs) of DNA were recorded at a minimum force ($\sim$ 0.2nN) in TE buffer. In compressibility measurements, the relative heights of (ss- or ds-) DNA NAMs, as a function of the applied load, were collected by gradually increasing the imaging forces from pull-off (low) force ($\sim$ 0nN) to high force ($\sim$ 2nN).

A.2.4 Preparation of ssDNA SAM and nanografting of TOEG3

Freshly cleaved gold substrates were immersed in a 1M NaCl TE buffer solution with 1 μM thiolated ssDNA for 12-14 hours and subsequently treated in a 1mM mercaptohexanol solution [39]. TOEG3 has been nanografted into the freshly prepared ssDNA SAMs using a 1:1 mixture of TE buffer and ethanol with 6μM of TOEG3 molecules.

A. APPENDIX: EXPERIMENTAL DETAILS

References

[1] Watson J. D. and Crick F. H. C. A Structure for Deoxyribose Nucleic Acid. *Nature*, **171**:737–738, 1953.

[2] Watson J. D. and Crick F. H. C. Genetical Implications of the structure of Deoxyribonucleic Acid. *Nature*, **171**:964–967, 1953.

[3] V. A. Bloomfield, D. M. Crothers, and I. Jr. Tinoco. *Nucleic Acids*. University Science Books, 1999.

[4] S. Mueller, editor. *Nucleic Acids from A to Z*. Wiley-VCH Verlag GmbH and Co. KGaA, Weinheim, 2008.

[5] F. Ritort. Single-molecule experiments in biological physics: methods and applications. *J. Phys.: Condens. Matter*, **18**(32):R531, 2006.

[6] J. L. R. Arrondo and A. Alonso, editors. *Advanced Techniques in Biophysics*, **10** of *Springer Series in Biophysics*. Springer-Verlag GmbH, 2006.

[7] S. Kumar and M. S. Li. Biomolecules under mechanical force. *Physics Reports*, **486**:1–74, 2010.

[8] K. R. Chaurasiya, T. Paramanathan, M. J. McCauley, and M. C. Williams. Biophysical characterization of DNA binding from single molecule force measurements. *Physics of Life Reviews*, **7**:299–341, 2010.

[9] E. Mirmomtaz, M. Castronovo, C. Grunwald, F. Bano, D. Scaini, A. A. Ensafi, G. Scoles, and L. Casalis. Quantitative Study of the Effect of Coverage on the Hybridization Efficiency of Surface-Bound DNA Nanostructures. *Nano Letters*, **8**(12):4134–4139, 2008.

[10] M. D. Frank-Kamenetskii. Biophysics of the DNA molecule. *Physics Reports*, **288**:13–60, 1997.

[11] Franklin R. and Gosling R. G. Molecular Configuration in Sodium Thymonucleate. *Nature*, **171**:740–741, 1953.

[12] Franklin R. and Gosling R. G. Evidence for 2-Chain Helix in Crystalline Structure of Sodium Deoxyribonucleate. *Nature*, **172**:156–157, 1953.

[13] M. H. F. Wilkins, A. R. Stokes, and H. R. Wilson. Molecular Structure of Deoxypentose Nucleic Acids. *Nature*, **171**(738-740), 1953.

[14] V. K. McElheny. *Watson and DNA: Making a Scientific Revolution*. Perseus Publishing, 2002.

[15] W. Saenger. *Principles of nucleic acid structure*. New York Springer-Verlag, 1984.

[16] C. Bustamante, Z. Bryant, and S. B. Smith. Ten years of tension: single-molecule DNA mechanics. *Nature*, **421**:423–427, January 2003.

[17] P. C. Braga and D. Ricci, editors. *Atomic Force Microscopy : Biomedical Methods and Applications*. Humana Press Inc., 2004.

[18] M. Rief and H. Gruebmuller. Force Spectroscopy of Single Biomolecules. *Chem. Phys. Chem.*, **3**:255–261, 2002.

[19] A. Ashkin. Acceleration and Trapping of Particles by Radiation Pressure. *Phys. Rev. Lett.*, **24**:156–159, 1970.

[20] A. Ashkin, J. M. Dziedzic, J. E. Bjorkholm, and Steven Chu. Observation of a single-beam gradient force optical trap for dielectric particles. *Optics letters*, **11**(5):288–290, 1986.

[21] S. B. Smith, Y. Cui, and C. Bustamante. Optical-trap force transducer that operates by direct measurement of light momentum. *Methods. Enzymol.*, **361**:134–160, 2003.

[22] http://tweezerslab.unipr.it.

[23] M. Rubinstein and R. Colby. *Polymer Physics*. Oxford University Press, Oxford, UK, 2003.

[24] J. F. Marko and E. D. Siggia. Stretching DNA. *Macromolecules*, **28**(8759), 1995.

[25] T. Vo-Dinh and B. Cullum. Biosensors and Biochips: advances in biological and medical diagnostics. *Fresenius J. Anal. Chem.*, **366**:540–551, 2000.

[26] F. R. R. Teles and L. P. Fonseca. Trends in DNA Biosensors. *Talanta*, **77**:606–623, 2008.

[27] C. M. Niemeyer. Self-assembled nanostrutures based on DNA: towards the development of nanobiotechnology. *Current Opinion in Chemical Biology*, **4**:609–618, 2000.

[28] C. M. Niemeyer. DNA as a material for nanotechnology. *Angew. Chem. Int. Ed.*, **36**(6):585–587, 1997.

[29] N. C. Seeman. DNA engineering and its application to nanotechnology. *Trends in Biotechnology*, **17**(11):437 – 443, 1999.

[30] N. C. Seeman. An Overview of Structural DNA Nanotechnology. *Molecular Biotechnology*, **37**:246–257, 2007.

[31] M. Dufva. *DNA Microarray for Biomedical Research: Methods and Protocols*, **529**. Humana Press Inc., 2009.

[32] http://bitesizebio.com/, July 2011.

[33] W. Vercoutere and M. Akeson. Biosensors for DNA sequence detection. *Current Opinion in Chemical Biology*, **6**:816–822, 2002.

[34] E. Mariotti, M. Minunni, and M. Mascini. Surface plasmon resonance biosensor for genetically modified organisms detection. *Analytica Chimica Acta*, **453**(2):165 – 172, 2002.

[35] M. Thompson, B. A. Cavic, L. M. Furtado, Z. Morel, and N. Tassew. Acoustic wave biosensor study of interfacially-bound proteins, nucleic acids and blood platelets, 2000.

[36] M. Castronovo, S. Radovic, C. Grunwald, L. Casalis, M. Morgante, and G. Scoles. Control of Steric Hindrance on Restriction Enzyme Reactions with Surface-Bound DNA Nanostructures. *Nano Letters*, **8**(12):4140–4145, 2008.

[37] C. M. Niemeyer. Semisynthetic DNA-Protein Conjugates for Biosensing and Nanofabrication. *Angew. Chem. Int. Ed.*, **49**:1200–1216, 2010.

[38] F. Bano, L. Fruk, B. Sanavio, M. Glettenberg, L. Casalis, C. M. Niemeyer, and G. Scoles. Toward multiprotein nanoarrays using nanografting and DNA directed immobilization of proteins. *Nano Letters*, **9**(7):2614–2618, July 2009.

[39] A. W. Peterson, R. J. Heaton, and R. M. Georgiadis. The effect of surface probe density on DNA hybridization. *Nucl. Ac. Res.*, **29**(24):5163–5168, 2001.

[40] Z. Zhang, J. Zhou, A. Tang, Z. Wu, G. Shen, and R. Yu. Scanning electrochemical microscopy assay of DNA based on hairpin probe and enzymatic amplification biosensor. *Biosensors and Bioelectronics*, **25**(8):1953–1957, 2010.

[41] X. Liang, H. Kuhn, and M. D. Frank-Kamenetskii. Monitoring Single-Stranded DNA Secondary Structure Formation by Determining the Topological State of DNA Catenanes. *Biophys. J.*, **90**(8):2877–2889, 2006.

[42] S. Kumar and G. Mishra. Stretching single stranded DNA. *Soft Matter*, **7**:4595–4605, 2011.

[43] Y. Zhang, H. Zhou, and Z.-C. Ou-Yang. Stretching single stranded DNA: Interplay of Electrostatic, Base-Pairing and Base-Pair Stacking Interactions. *Biophys. J.*, **81**:1133–1143, 2001.

[44] M. J. Lacy and E. W. Voss Jr. Direct adsorption of ssDNA to polystyrene for characterization of the DNA/anti-DNA interaction, and immunoassay for anti-DNA autoantibody in New Zealand White mice. *Journal of Immunological Methods*, **116**(1):87 – 98, 1989.

[45] S. Manohar, A. R. Mantz, K. E. Bancroft, C.-Y. Hui, A. Jagota, and D. V. Vezenov. Peeling Single-Stranded DNA from Graphite Surface to Determine Oligonucleotide Binding Energy by Force Spectroscopy. *Nano Letters*, **8**(12):4365–4372, 2008.

[46] D. Y. Petrovykh, H. Kimura-Suda, L. J. Whitman, and M. J. Tarlov. Quantitative Analysis and Characterization of DNA Immobilized on Gold. *J. Am. Chem. Soc.*, **125**:5219–5226, 2003.

[47] D. Y. Petrovykh, V. Pérez-Dieste, A. Opdahl, H. Kimura-Suda, J. M. Sullivan, M. J. Tarlov, F. J. Himpsel, and L. J. Whitman. Nucleobase Orientation and Ordering in Films of Single-Stranded DNA on Gold. *J. Am. Chem. Soc.*, **128**:2–3, 2006.

[48] C. Ehresmann, F. Bauldin, M. Mougel, P. Romby, J. P. Ebel, and B. Ehresmann. Probing the structure of RNA. *Nucl. Ac. Res.*, **15**:9109–9128, 1987.

[49] F. Dong, H. T. Allawi, T. Anderson, B. P. Neri, V. A. Parsegian, and I. Lyamichev. Secondary structure predictio and structure specific sequence analysis od single stranded DNA. *Nucl. Ac. Res.*, **29**(15):3248–3257, 2001.

[50] S. B. Smith, Y. Cui, and C. Bustamante. Overstretching B-DNA: The Elastic Response of Individual Double-Stranded and Single-Stranded DNA Molecules. *Science*, **271**(5250):795–799, 1996.

[51] C. Bustamante, S. B. Smith, J. Liphardt, and D. Smith. Single-molecule studies of DNA mechanics. *Current Opinion in Structural Biology*, **10**:279–285, 2000.

[52] M.-N. Dessinges, B. Maier, Y. Zhang, M. Peliti, D. Bensimon, and V. Croquette. Stretching single stranded DNA, a model polyelectrolyte. *Phys. Rev. Lett.*, **89**(24):248102, 2002.

[53] C. Danilowicz, C. H. Lee, V. W. Coljee, and M. Prentiss. Effects of temperature on the mechanical properties of single stranded DNA. *Phys. Rev. E*, **75**:030902, 2007.

[54] O. A. Saleh, D. B. McIntosh, P. Pincus, and N. Ribeck. Nonlinear Low-Force Elasticity of Single-Stranded DNA Molecules. *Phys. Rev. Lett.*, **102**(6):068301, Feb 2009.

[55] D. B. McIntosh, N. Ribeck, and O. A. Saleh. Detailed scaling analysis of low-force polyelectrolyte elasticity. *Phys. Rev. E*, **80**(4):041803, 2009.

[56] D. B. McIntosh and O. A. Saleh. Salt Species-Dependent Electrostatic Effects on ssDNA Elasticity. *Macromolecules*, **44**(7):2328–2333, 2011.

[57] A. Montanari and M. Mézard. Hairpin Formation and Elongation of Biomolecules. *Phys. Rev. Lett.*, **86**(10):2178–2181, 2001.

[58] N. M. Toan, D. Marenduzzo, and C. Micheletti. Inferring the Diameter of a Biopolymer from Its Stretching Response. *Biophys. J.*, **89**:80–86, 2005.

[59] N. M. Toan and C. Micheletti. Inferring the effective thickness of polyelectrolytes from stretching measurements at various ionic strengths: applications to DNA and RNA. *J. Phys.: Condens. Matter*, **18**:S269–S281, 2006.

[60] Y. Seol, G. Skinner, and K. Visscher. Elastic Properties of a Single-Stranded Charged Homopolymeric Ribonucleotide. *Phys. Rev. Lett.*, **93**:118102, 2004.

[61] J. M. Huguet, C. V. Bizarro, N. Forns, S. B. Smith, C. Bustamante, and F. Ritort. Single-molecule derivation of salt dependent base-pair free energies in DNA. *Proc. Natl. Acad. Sci. USA*, **107**(35):15431–15436, 2010.

[62] U. Gerland, R. Bundschuh, and Terence H. Mechanical probing the folding pathway of single RNA molecules. *Biophys. J.*, **84**:2831–2840, 2003.

[63] U. Gerland, R. Bundschuh, and Terence H. Force-Induced Denaturation of RNA. *Biophys. J.*, **81**:1324–1332, 2001.

[64] A. R. Wolfe and T. Meehan. The effect of sodium ion concentration on intrastrand base-pairing in single-stranded DNA. *Nucl. Ac. Res.*, **22**(15):3147–3150, 1994.

[65] N. M. Toan and D. Thirumalai. Theory of Biopolymer Stretching at High Forces. *Macromolecules*, **43**:4394–4400, 2010.

[66] B. Essevaz-Roulet, U. Bockelmann, and F. Heslot. Mechanical separation of the complementary strands ofDNA. *Proc. Natl. Acad. Sci. USA*, **94**(22):11935–11940, 1997.

[67] G. Caliskan, C. Hyeon, U. Perez-Salas, R. M. Briber, S. A. Woodson, and D. Thirumalai. Persistence Length Changes Dramatically as RNA Folds. *Phys. Rev. Lett.*, **95**:268303, 2005.

[68] B. I. Shklovskii. Screening of a macroion by multivalent ions: Correlation-induced inversion of charge. *Phys. Rev. E*, **60**:5802–5811, 1999.

[69] S. L. Heilman-Miller, D. Thirumalai, and S. A. Woodson. Role of Counterion Condensation in Folding of the Tetrahymena Ribozyme. I. Equilibrium Stabilization by Cations. *J. Mol. Biol.*, **306**:1157–1166, 2001.

[70] C. V. Bizarro, A. Alemany, and F. Ritort. Non specific binding of Mg2+ to RNA determined by force spectroscopy methods. *to be published*.

[71] M. Schena, D. Shalon, R. W. Davis, and P. O. Brown. Quantitative monitoring of gene expression patterns with a complementary DNA microarray. *Science*, **270**:467–470, 1995.

[72] M. J. Heller. DNA Microarray Technology: Devices, Systems, and Applications. *Annu. Rev. Biomed. Eng.*, **4**:129–53, 2002.

[73] R. B. Stoughton. Applications Of DNA Microarrays In Biology. *Annu. Rev. Biochem.*, **74**:53–82, 2005.

[74] C. Wingren and C. A. K. Borrenbaeck. Progress in miniaturization of protein arrays–a step closer to high-density nanoarrays. *Drug Discovery Today*, **12**(19-20):813–819, 2007.

[75] C. Wingren and C. A. K. Borrebaeck. Antibody microarray analysis of directly labelled complex proteomes. *Current Opinion in Biotechnology*, **19**(1):55–61, 2 2008.

[76] C. J. Johnson, N. Zhukovsky, A. E. G. Cass, and J. M. Nagy. Proteomics, nanotechnology and molecular diagnostics. *Proteomics*, **8**(4):715–730, 2008.

[77] S. Husale, H. H. J. Persson, and O. Sahin. DNA nanomechanics allows direct digital detection of complementary DNA and microRNA targets. *Nature*, **462**(24):1075–1078, 2009.

[78] V. V. Rybenkov, N. R. Cozzarelli, and A. V. Vologodskii. Probability of DNA knotting and the effective diameter of the DNA double helix. *Proc. Natl. Acad. Sci. USA*, **90**(11):5307–5311, 1993.

[79] O. Gonzalez and J. H. Maddocks. Global curvature, thickness, and the ideal shapes of knots. *Proc. Natl. Acad. Sci. USA*, **96**:4769–4773, 1999.

[80] D. Marenduzzo and C. Micheletti. Thermodynamics of DNA packaging inside a viral capsid: the role of DNA intrinsic thickness. *J. Mol. Biol.*, **330**:485–492, 2003.

[81] C. Micheletti, D. Marenduzzo, E. Orlandini, and D. W. Summers. Knotting of random ring polymers in confined spaces. *J. Chem. Phys.*, **124**(6):064903, 2006.

[82] H. Yamakawa. Stiff-Chain Macromolecules. *Annu. Rev. Phys Chem.*, **35**:23–47, 1984.

[83] R. Ramachandran, G. Beaucage, A. S. Kulkarni, D. McFaddin, J. Merrick-Mack, and V. Galiatsatos. Persistence Length of Short-Chain Branched Polyethylene. *Macromolecules*, **41**:9802–9806, 2008.

[84] A. Opdahl, D. Y. Petrovykh, H. Kimura-Suda, M. J. Tarlov, and L. J. Whitman. Independent control of grafting density and conformation of single-stranded DNA brushes. *Proc. Natl. Acad. Sci. USA*, **104**(1):9–14, 2007.

[85] M. Cárdenas, J. Barauskas, K. Schillén, J. L. Brennan, M. Brust, and T. Nylander. Thiol-Specific and Nonspecific Interactions between DNA and Gold Nanoparticles. *Langmuir*, **22**:3294–3299, 2006.

[86] J. N. Israelachvili. *Intermolecular and Surface Forces*. Academic Press London, 1991.

[87] W. Kaiser and U. Rant. Conformations of End-Tethered DNA Molecules on Gold Surfaces: Influences of Applied Electric Potential, Electrolyte Screening, and Temperature. *J. Am. Chem. Soc.*, **132**(23):7935–7945, 2010.

[88] K. Binder, editor. *Monte Carlo and Molecular Dynamics Simulation in Polymer Physics*. Oxford University Press, 1995.

[89] N. Metropolis, A. W. Rosenbluth, M. N. Rosenbluth, A. H. Teller, and E. Teller. Equation of State Calculations by Fast Computing Machines. *J. Chem. Phys.*, **21**(6):1087–1092, 1953.

[90] H. Meyer J. Baschnagel, J.P. Wittmer. Monte Carlo SImulation of Polymers: Coarse-Grained Models. *NIC Series*, **23**:83–140, 2004.

[91] J. N. Sneddon. The relation between load and penetration in the axisymmetric Boussinesq problem for a punch of arbitrary profile. *Int. J. Eng. Sci.*, **3**:47–57, 1965.

[92] M. Heuberger, G. Dietler, and L. Schlapbach. Elastic deformations of tip and sample during atomic force microscope measurements. *J. Vac. Sci. Tec. B*, **14**:1250–1254, 1996.

[93] B. Cappella and G. Dietler. Force-Distance curves by atomic force microscopy. *Surface Science Reports*, **34**:1–104, 1999.

[94] S. Steltenkamp, M. M. Muller, M. Deserno, C. Hennesthal, C. Steinem, and A. Janshoff. Mechanical Properties of Pore-Spanning Lipid Bilayers Probed by Atomic Force Microscopy. *Biophys. J.*, **91**:217–226, 2006.

[95] M. Liu, N. A. Amro, C. S. Chow, and G. y. Liu. Production of Nanostructures of DNA on Surfaces. *Nano Letters*, **2**(8):863–867, 2002.

[96] M. Liu, N. A. Amro, and G. y. Liu. Nanografting for Surface Physical Chemistry. *Annu. Rev. Phys Chem.*, **59**:367–386, 2008.

[97] L. G. Rosa and J. Liang. Atomic Force Microscope Nanolithography: Dip-Pen, Nanoshaving, Tapping Mode, Electrochemical and Thermal Nanolithography. *J. Phys.: Condens. Matter*, **21**:483001, 2009.

[98] C. M. Niemeyer, L. Boldt, B. Ceyhan, and D. Blohm. DNA-directed immobilization: efficient, reversible, and site-selective surface binding of proteins by means of covalent DNA-Streptavidin conjugates. *Analytical Biochemistry*, **268**(1):54 – 63, 1999.

[99] H. Schroeder, M. Adler, K. Gerigk, B. Müller-Chorus, F. Götz, and C. M. Niemeyer. A User Configurable Microfluidic Device for Multiplexed Immunoassays Based on DNA-Directed Assembly. *Anal. Chem.*, **81**:1275–1279, 2009.

[100] J. Müller and C. M. Niemeyer. DNA-directed assembly of artifical multienzyme complexes. *Biochem. Biophys. Res. Commun.*, **377**:62–67, 2008.

[101] L. K. Wolf, Y. Gao, and R. M. Georgiadis. Sequence-Dependent DNA Immobilization: Specific versus Nonspecific Contributions. *Langmuir*, **20**:3357–3361, 2004.

[102] I. Y. Wong and N. A. Melosh. An Electrostatic Model for DNA Surface Hybridization. *Biophys. J.*, **98**(12):2954 – 2963, 2010.

[103] D. Irving, P. Gong, and R. Levicky. DNA Surface Hybridization: Comparison of Theory and Experiment. *J. Phys. Chem. B*, **114**(22):7631–7640, 2010.

[104] P. Gong and R. Levicky. DNA surface hybridization regimes. *Proc. Natl. Acad. Sci. USA*, **105**(14):5301–5306, 2008.

[105] C. Bustamante and S. B. Smith. Light-Forces sensor and method for measuring axial optical-trap forces from changes in light momentum along an optical axis. Technical report, U.S. Patent 7,133,132,B2, 2006.

[106] C. Bustamante and S. B. Smith. Optical beam translation device and method using a pivoting optical fiber. Technical report, U.S. Patent 7,274,415,B2, 2006.

List of Figures

LIST OF FIGURES

List of Tables

Acknowledgements

First of all I would like to express my deepest gratitude to my supervisors, Prof. Cristian Micheletti and Prof. Antonio DeSimone for their patient support and precious guidance throughout my entire PhD and in particular in these last months. Without their careful reading, all the suggestions and the corrections, this thesis would not be written.

I want to thank also Prof. Felix Ritort for having hosted me for seven months at the Small Biosystem lab in Barcelona, for his helpful advices and for all the valuable comments about the work carried out there.

I am also very thankful to Dr. Loredana Casalis for having contributed to the work on the DNA patches (in particular in the experimental parts) with her durable support and the useful discussions during these years of collaboration. I would like to thank also Prof. Giacinto Scoles for the illuminating and stimulating discussions.

I am deeply grateful to all the people of the laboratories with whom I have collaborated. In particular I would like to thank Joan Camunas, Sara de Lorenzo and Dr. Marco Ribezzi from the Small Biosystem Lab that helped with the OT and the various synthesis. I am very thankful to Dr. Josep Maria Huguet for the data of 3kb ssDNA and their analysis. I owe my thanks also to Dr. Fouzia Bano and Dr. Pietro Parisse from Senil Lab that carefully and patiently carried out the AFM experiments and contributed with their ideas to the project of DNA patch compression.

I would like to thank all the friends, the present and the former colleagues from SISSA that supported me in these 4 years.

At the end, I would like to express my deepest thanks to my extended family in Povoletto and here in Trieste who helped me to face all my difficult

moments. Knowing that you are with me in each and every decision is the best gift that a man can have.

Declaration

I herewith declare that I have produced this thesis without the prohibited assistance of third parties and without making use of aids other than those specified; notions taken over directly or indirectly from other sources have been identified as such. This paper has not previously been presented in identical or similar form to any other Italian or foreign examination board.

The thesis work was conducted from Novembre 2007 to November 2011 under the supervision of Prof. Antonio DeSimone and Prof. Cristian Micheletti at SISSA .